Electric and Magnetic Field Control for Electric Dipole Moment Searches

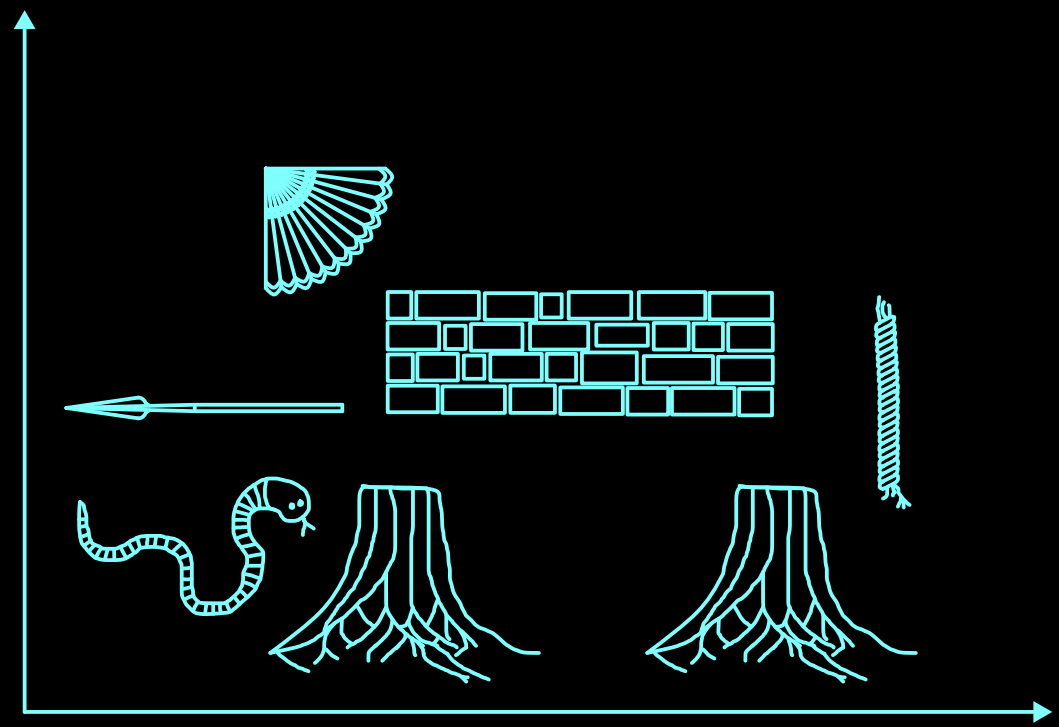

Thomas Benjamin Meijknecht

Electric and Magnetic Field Control for Electric Dipole Moment Searches

Cover: The mysterious gift

Once, a merchant had a tent set up before the palace. He said to the king: "If you can say what is in the tent within 24 hours, it will be yours". So the king asked his 7 best scientists to investigate the contents of the tent. Of the 7, 6 entered the tent, one remained outside. It was dark in the tent. The 6 could only use the sense of touch. The one outside the tent asked the 6 what they had observed, and where that was. Pen and paper in hand, he mapped the observations of the others: "a snake", "a wall", "a spear", "a fan", "a rope", and "a trunk" (see front cover). The 7 scientists debated their observations and the map until deep into the night. Tired, one of them dozed off. He felt the ground trembling. He heard trumpets. He saw large dark shapes moving closer. He was going to get trampled... "Elephants," he exclaimed, cold sweat sticking to his clothes. It was just a dream. "But that is the answer," another said, "it is an elephant" (see back cover). The 7 scientists reported their findings to the king. He attained the mysterious gift.

Adapted from the Eastern fable *Blind men and an elephant*.

university of groningen

NWO

Nikhef

The work in this thesis has been carried out at the Van Swinderen Institute for Particle Physics and Gravity of the University of Groningen. This work is done as part of the NL-*e*EDM consortium which receives funding (EEDM-166) from the Dutch Research Council (NWO). This work originates as part of the research programme of the Foundation for Fundamental Research on Matter (FOM), and falls as of 1 April 2017, under the responsibility of Netherlands Foundation of Scientific Research Institutes (NWO-I), which is part of the Dutch Research Council (NWO).

Cover: Thomas B. Meijknecht
Printed by: Gildeprint

university of groningen

Electric and Magnetic Field Control for Electric Dipole Moment Searches

PhD thesis

to obtain the degree of PhD at the
University of Groningen
on the authority of the
Rector Magnificus Prof. J.M.A. Scherpen
and in accordance with
the decision by the College of Deans.

This thesis will be defended in public on

Tuesday 28 November 2023 at 11.00 hours

by

Thomas Benjamin Meijknecht

born on 11 June 1990
in Leeuwarden

Supervisor
Prof. K.H.K.J. Jungmann

Co-supervisor
Dr. L. Willmann

Assessment Committee
Prof. P. Crivelli
Prof. J. Even
Prof. C.J.G. Onderwater

Contents

Abstract iv
Abstract (Nederlands) iv

1 Introduction **1**
1.1 The Standard Model and beyond 1
1.2 Permanent Electric Dipole Moments 2
1.3 Thesis outline 4

2 From P,T-Violation to eEDM Searches with BaF **5**
2.1 P,T-Violation through eEDMs 5
2.2 eEDM searches in atoms and molecules 6
2.3 eEDM sensitive search with BaF 8
2.3.1 BaF experiment setup 10
2.3.2 eEDM statistical sensitivity 12
2.4 Requirements for an interaction zone 13

3 eEDM Experiment Setup **15**
3.1 Full setup 16
3.2 Magnetic field control 17
3.3 Active compensation with external coils 18
3.4 Passive stabilization using a multi-layer μ-metal magnetic shield 20
3.4.1 Design and calculations 20
3.4.2 Implementation 27
3.5 Magnetic holding field generation 28
3.5.1 Double cosine coil to generate magnetic holding field 28
3.5.2 Coil for transverse field effect investigation 33
3.5.3 Active compensation with internal coils 33
3.6 Non-magnetic materials 35
3.7 Electric field generation 36
3.8 Vacuum system 36
3.9 Interaction zone internals 36
3.10 Lasers 36
3.11 Data Acquisition 41
3.12 Conclusion 42

4 Generate Homogeneous nT Magnetic Fields in a 70 μT Environment **43**
4.1 Magnetic field probing using flux gates . . . 43
4.2 Environmental impact on magnetic field . . . 44
4.3 Field map inside the magnetic shield . . . 45
4.4 Holding field generation inside the magnetic shield . . . 49
4.5 Conclusion . . . 50

5 Electric and Magnetic Field Maps with a BaF Beam - One pulse laser spectroscopy **51**
5.1 Experimental method . . . 51
5.2 Electric field measurements . . . 53
5.3 Magnetic field measurements . . . 53
5.4 Conclusion . . . 58

6 Capabilities of the Experiment for EDM Searches - Two pulse laser spectroscopy **59**
6.1 Spin precession signal from photon counting . . . 59
6.2 Magnetic field . . . 63
6.2.1 Tuning the magnetic holding field with the double cosine coil . . 64
6.2.2 Differential shielding factor of magnetic shield . . . 67
6.2.3 Length of homogeneous magnetic fields . . . 68
6.3 Electric field . . . 69
6.4 Motional and transverse magnetic fields . . . 70
6.5 Systematic effects . . . 75
6.6 Conclusion . . . 78

7 Summary **81**

8 Nederlandse samenvatting **83**

Acknowledgments **85**

A Conventions **87**

B Vacuum system for an eEDM experiment **89**
B.1 Purpose of and requirements on the vacuum system . . . 89
B.2 Vacuum materials . . . 89
B.3 Vacuum properties . . . 90

C Magnetic shield specification from Sekels **93**

D ITO-coated glass plates for electric field generation **105**

E Electric field reversal box **111**

F A note on airpads **113**

G Flux Gates **115**

H Magnetic field maps of the interaction zone employing flux gates 117

Bibliography 123

Abstract

Permanent Electric Dipole Moments (EDMs) would violate the symmetries of parity and time-reversal, and with validity of CPT symmetry they would also violate the combined CP symmetry. EDMs have been suggested in many speculative extensions to the Standard Model of particle physics. The purpose of the NL-eEDM experiment is to search for a permanent electron Electric Dipole Moment (eEDM). The experiment entails a BaF molecular beam moving through an interaction zone with a homogeneous electric and a homogeneous magnetic field. A non-zero eEDM would reveal itself in a different spin precession behavior for parallel and anti-parallel electric and magnetic fields.

The emphasis of this work lies on the design, implementation, evaluation and use of the interaction zone for this new experiment. The design is informed by calculations with COMSOL software. The implementation consists of Indium Tin Oxide (ITO) coated glass plates for homogeneous electric field generation at several $\mathrm{kV/cm}$ scale. A homogeneous magnetic field of $\mathcal{O}(\mathrm{nT})$ is realized by a novel designed double cosine coil, which resides in a 5 layer μ-metal shield with $\mathcal{O}(10^6)$ shielding surrounded by rectangular compensation coils.

This work in combination with work on a BaF source, laser systems, a quantum mechanical description of the measurement process, data acquisition and analysis provides the first complete eEDM setup at the VSI in Groningen. Measurements have been performed with spin precession on BaF molecules in order to quantify the capabilities of the setup. These show that the setup of the interaction zone suffices for a competitive eEDM search.

Abstract (Nederlands)

Permanente Elektrische Dipool Momenten (EDM's) zouden pariteits- en tijdsomkeringsymmetrie breken, en samen met de validiteit van CPT-symmetrie zouden zij ook de gecombineerde CP-symmetrie breken. EDM's zijn gesuggereerd in veel speculatieve extensies van het Standaard Model der deeltjefysica. Het doel van het NL-eEDM experiment is om te zoeken naar een permanenent electron Elektrisch Dipool Moment (eEDM). Het experiment bevat een moleculaire BaF bundel die beweegd door een interactiegebied met een homogeen elektrisch en een homogeen magnetisch veld. Een eEDM ongelijk aan nul toont zich in een verschillend spinprecessiegedrag voor parallelle en anti-parallelle elektrische en magnetische velden.

Dit werk legt de nadruk op het ontwerp, de implementatie, de evaluatie en het gebruik van het interactiegebied voor dit nieuwe experiment. Het ontwerp is met behulp van berekeningen in COMSOL software gemaakt. De implementatie omvat met Indium Tin Oxide (ITO) gecoate glasplaten voor opwekking van een homogeen elektrisch veld op een schaal van enkele $\mathrm{kV/cm}$. Een homogeen $\mathcal{O}(\mathrm{nT})$ magnetische veld wordt gerealiseerd door een nieuw ontworpen dubbele cosinusspoel, die is behuist in een 5-laags μ-metaal schild met $\mathcal{O}(10^6)$ afscherming omgeven door rechthoekige compensatiespoelen.

Dit werk samen met werk aan een BaF bron, laser systemen, een kwantummechanische beschrijving van het meetproces, data-acquisitie en analyse bieden de eerste volledige eEDM-opstelling in het VSI te Groningen. Metingen zijn uitgevoerd met spinprecessie op BaF moleculen om de capaciteiten van het experiment te quantificeren. Deze laten zien dat de opstelling van het interactiegebied afdoende is voor een competetieve eEDM zoektocht.

1 Introduction

1.1 The Standard Model and beyond

The Standard Model (SM) of elementary particles and their interactions is a phenomenal achievement in physics. It rests on the fundamental symmetries of the strong and electroweak interaction: $SU(3) \times SU(2) \times U(1)$. $SU(3)$ is the symmetry of the strong interaction. $SU(2) \times U(1)$ is the symmetry of the electroweak interaction. The theory of electroweak interactions [1–6] is itself a unification of the electromagnetic and the weak interactions. Particles predicted in the SM that mediate these interactions, such as the Z, W and Higgs bosons [7, 8], have been observed in high energy physics experiments at laboratories such as DESY, KEK, Fermilab, SLAC and CERN [9–11].

The discrete symmetries of charge-conjugation C, parity P, time-reversal T and combinations of them are either conserved or broken by SM interactions. Symmetry breaking has only been observed for weak interactions. A neutron Electric Dipole Moment (nEDM) search was suggested in 1950 to test parity conservation in the weak interaction [12]. A first limit was put on the nEDM in 1957 [13]. Another test of parity conservation in the weak interaction through β-decay, was suggested in 1957 [14]. Parity violation was subsequently observed using Co^{60} nuclear β-decay [15], opening the door for more searches for violations of C, or P, or T, or any combination of these. In 1964 CP symmetry violation was found in neutral kaon decay [16]. The combined CPT symmetry appears to date unbroken. Its conservation has been motivated by the CPT theorem [17–19]. CPT symmetry is conserved in the SM and is intrinsically connected to the Lorentz invariance symmetry [20, 21].

The SM of particle physics can not explain the baryon asymmetry observed in astrophysical observations. One possible explanation assumes besides a number of further assumptions, additional sources of CP violation beyond what has been observed up to now [22]. This motivates searches for physics beyond the Standard Model through experiments at all accessible energy scales. Tests can be performed in high energy physics, such as at the LHC, through the direct creation of new particles predicted by new physics. High precision measurements form a different but complementary approach where new physics becomes observable at low energy through small observable modifications of predicted SM effects. One category of such high precision measurements is the search for permanent electric dipole moments.

Beyond the initial work on the nEDM [12, 13] there have been more EDM searches in various systems. An overview of the field of EDMs can be found, e.g. in several reviews and books [23–29]. In the 1960's the enhancement of the electron Electric Dipole Moment (eEDM) in atoms was pointed out [30–32]. Furthermore various

types of matter have been employed, e.g. heavy leptons such as the muon and tau [27, 33–38], neutrons [12, 13, 39], protons [40–43], deuterons [44], condensed matter [45, 46], atoms and nuclei [47–51] (e.g. Xe, Hg), bound electrons [52–56] (bound in e.g. atoms, molecules, solid state systems). Our experiment is in a competitive field to search for eEDMs employing polar diatomic molecules. Polar molecules such as BaF and YbF have a substantially larger enhancement of the eEDM compared to atoms, due to a large number of close-lying molecular states of opposite parity which are mixed in an external electric field. These have been calculated by a number of theoretical groups for various systems [57–62].

1.2 Permanent Electric Dipole Moments

Besides them being interesting in themselves, one motivation for permanent Electric Dipole Moment (EDM) [i] searches is the investigation of discrete symmetries. EDMs require both P-violation and T-violation. An additional set of motivations for EDM searches, through P,T-violation, is them forming tests of Standard Model extensions and cosmology. Assuming CPT invariance, a T violating EDM is equivalent to CP symmetry breaking. Many theories beyond the Standard Model that have additional CP or CPT symmetry breaking also predict an EDM on particles such as the electron (see Fig. 1.1). A Hamiltonian of a particle with magnetic dipole moment $\vec{\mu}$ and EDM $\vec{d}$ in magnetic field $\vec{B}$ and electric field $\vec{E}$ [24] contains

$$H = -(\vec{\mu} \cdot \vec{B} + \vec{d} \cdot \vec{E}), \tag{1.1}$$

where $\vec{\mu} = \mu\vec{S}$, $\vec{d} = d\vec{S}$, and $\vec{S}$ is the particle spin.

An EDM breaks P and T symmetry. This is illustrated in Fig. 1.2 by the relative orientation of arrows. In the center all dipole moments and fields are aligned parallel with the spin $\vec{S}$. Under P or T transformations, the electric dipole moment $\vec{d}$ changes sign compared to spin $\vec{S}$. The electric field $\vec{E}$ changes sign in a P transformation. Under P or T transformations, the magnetic dipole moment $\vec{\mu}$ stays aligned with the spin $\vec{S}$, which itself transforms like magnetic field $\vec{B}$ [28]. The electric dipole moment breaks but the magnetic dipole moment conserves P and T symmetries.

The principle of EDM measurements is shown in Fig. 1.3. Searches for an electron Electric Dipole Moment (eEDM) require the measurement precision of the energy eigenvalues of H to be smaller than the size of the eEDM contribution. This measurement precision primarily depends on the uncertainty in the environmental magnetic field. A particular feature of searches in molecules is the sensitivity to the alignment of electric and magnetic fields. The primary problem that this thesis addresses is: *how to realize an experimental setup with sufficient control over its environment, with electric and magnetic field control in particular?*

[i] Within this thesis any mention of an EDM implies a permanent EDM. A permanent EDM is aligned with particle spin, and remains non zero for the electric field approaching zero, unlike induced electric dipole moments [32].

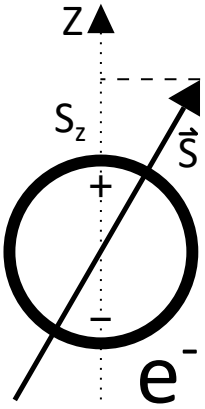

Figure 1.1: Elementary particles such as the electron have in several speculative models a permanent electric dipole moment [63–65]. For an extended object an EDM would be represented by a distance separating opposite electric charges. For a quantum system such as the electron, the spin $\vec{S}$ is the only vector quantity that can be defined independently. Any other vectorial quantities are proportional to $\vec{S}$, i.e. $\vec{\mu} = \mu\vec{S}$ and $\vec{d} = d\vec{S}$.

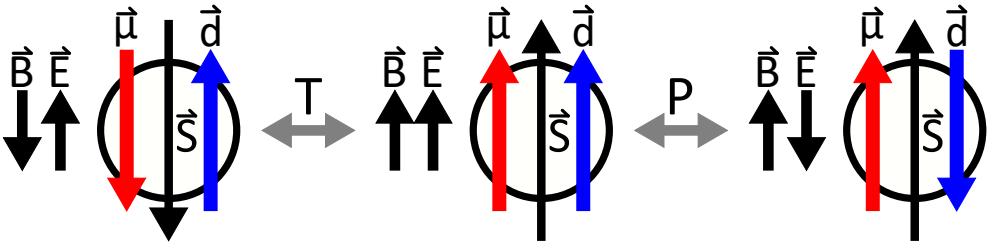

Figure 1.2: Visual representation of a particle with magnetic dipole moment $\vec{\mu}$ and electric dipole momement (EDM) $\vec{d}$, both of which are proportional to particle spin $\vec{S}$, in magnetic field $\vec{B}$ and electric field $\vec{E}$ under P and T symmetry [28].

Figure 1.3: In most searches for EDMs three conceptual steps can be distinguished.

1.3 Thesis outline

We investigated multiple factors in order to arrive at an experimental setup for an electron Electric Dipole Moment (eEDM) searches, with a particular focus on an interaction zone that has the required electric and magnetic field control.

In Chapter 2 we discuss the context of eEDM searches, from theory to experiment, in order to arrive at a more accurate problem formulation. We discuss the connection between the eEDM and the induced dipole moment in BaF molecules. We conclude the chapter with quantitative requirements on an interaction zone required for such searches, focusing on electric and magnetic fields.

Based on the required specifications of the interaction zone we design an experimental setup with the help of calculations using the commercial software package COMSOL [66] in Chapter 3.

In Chapter 4 we characterize the interaction zone properties with flux gates, in particular its magnetic field due to the high potential for causing unintended measurement results. We verify that the magnetic field fulfills the requirements for a sensitive EDM search. The flux gates are also positioned around the magnetic shield for continuous magnetic field monitoring.

The interaction zone is embedded within a newly built setup. The electric and magnetic fields have to be determined for an EDM experiment at runtime. In Chapter 5 we exploit electric and magnetic field sensitivity of transitions in BaF molecules to map these fields, employing one pulse two-photon spectroscopy.

In Chapter 6 we demonstrate the capabilities of the experiment for EDM searches, employing two pulse two-photon spectroscopy. We show how the results of spin precession measurements with a molecular BaF beam are derived from the detected photon signal. The magnetic and electric fields inside the interaction zone are measured by a spin precession method. An initial set of systematic effects is estimated, e.g. arising from motional magnetic fields, as their quantitative knowledge is of crucial importance for an EDM sensitive experiment.

Chapter 7 is a summary of the presented work. Chapter 8 is a summary of the presented work in Dutch, i.e. een Nederlandse samenvatting.

2 From P,T-Violation to eEDM Searches with BaF

How does an electron Electric Dipole Moment (eEDM) search impact fundamental Standard Model (SM) physics? What motivates such an experiment with BaF? How can such an experiment be performed with sufficiently high sensitivity? What are the requirements on an environment, an interaction zone, within which the BaF molecules are studied in a maximally eEDM sensitive state? These questions guide towards a formulation of requirements for an experimental setup.

2.1 P,T-Violation through eEDMs

The Standard Model (SM) predicts EDMs in many of its building blocks and systems composed of them. Through known CP violation we have EDMs induced by many loop processes, e.g. at minimum 3 loops for neutrons [67, 68] and 4 loops for leptons [69–72].

eEDM searches are a background-free probe for multiple alternative theories. Current eEDM searches aim for sensitivities that bring them within reach of SM extension predictions. Many SM extensions predict much larger eEDMs than the SM. Known CP-violation in the SM leads to an eEDM of $\mathcal{O}\left(10^{-38}\ \mathrm{e\,cm}\right)$ or less [63], well below the sensitivity of present apparatuses. Very recent calculations of so far neglected terms show that in paramagnetic atomic or molecular systems, if only one such system is used for an EDM measurement, an eEDM measurement to $d_e^{equiv} \approx 10^{-35}\ \mathrm{e\,cm}$ (see blue line in Fig. 2.1) or larger is possible [64, 73]. In that case searches through paramagnetic EDMs leave a search space up to approximately 5×10^7 GeV or smaller energy scale. Reaching beyond this scale requires probing different systems. Neutron EDM (nEDM) and proton EDM (pEDM) searches are closer to SM predictions [65] (see Fig. 2.1). The SM includes for the strong interaction a CP-violating term parametrized by $\bar{\theta}_{QCD}$. In fact, an EDM in ^{199}Hg of $|d_{Hg}| < 7.4 \times 10^{-30}\ \mathrm{e\,cm}$ (95% confidence level) yields the best upper limit $\bar{\theta}_{QCD} = 1.5 \times 10^{-10}$ [74–76]. The SM values for EDMs on neutrons and protons are respectively [74, 75, 77, 78]

$$1 \times 10^{-32}\ \mathrm{e\,cm} < |d_n|, |d_p| < 6 \times 10^{-32}\ \mathrm{e\,cm}. \tag{2.1}$$

Upon finding a nucleon EDM at or below this limit, an independent measurement is required to disentangle the contributions of the EDM and the $\bar{\theta}_{QCD}$ term. Hence with eEDM searches there is more room compared to nEDM and pEDM searches for falsifying alternative theories. In addition, eEDM searches can probe physics at energy

scales inaccessible to high energy physics experiments today and in the foreseeable future (see Fig. 2.2).

Searches for an eEDM, through parity and time-reversal violation, are connected to the cosmological phenomenon of matter-antimatter asymmetry. For every massive particle in the universe, there are 10^9 photons [83]. Ordinary matter mostly consists of baryons and electrons. Radiation is mostly CMB photons. One possible mechanism that creates an imbalance between matter and antimatter was formulated by Sakharov [22]. Most matter and antimatter annihilated when the universe froze out. The result is a small remnant of matter, and a relatively large amount of photons. The Sakharov conditions [22] are a set of conditions that can lead to such an asymmetry:

1. baryon (and lepton) number violation,
2. C violation,
3. CP violation,
4. and a non adiabatic out of equilibrium epoch of the universe.

This is one reason to search for CP violation, as well as T violation, by means of an EDM. In our case in particular that is an electron EDM (eEDM). An example at high energy scale of searches for new and different CP-violating observables is through $B^0_{(s)} \to l^+l^-$ decays, investigated to high precision by the LHCb collaboration [84]. The SM extension models do not require condition 4 [85, 86]. They assume violation of the combined CPT symmetry to obtain the apparent dominance of matter over antimatter.

2.2 eEDM searches in atoms and molecules

The first eEDM searches were performed with atomic ceasium beams [87–89], and later with a thallium atomic beam [54]. Increased precision was achieved employing diatomic molecules. The first experiment to set an upper limit on the eEDM with diatomic molecules used a YbF beam [55] (see Table 2.1). A ThO beam was used to set a significantly improved upper limit on the eEDM [79]. A HfF^+ ion trap was employed to set the current best upper limit on the eEDM [38, 80, 81]. The YbF and BaF experiments differ from the ThO and HfF^+ experiments, in that the former use a ground state (Σ) of the molecules, whereas the latter use an excited (Δ) state, which in part results in complementary systematics. Some molecules have a large difference in the relative sensitivity to the eEDM and the SM-CKM terms, e.g. BaF and ThO [57], which is needed to go beyond an eEDM sensitivity indicated by the blue line in Fig. 2.1. The NL-eEDM experiment exploits BaF molecules and has been set up to improve the limits on the eEDM, because of experimental advantages [82].

Table 2.1: Upper limits set on eEDM d_e at 90% confidence level by experiments employing diatomic molecules.

Molecule	$\lvert d_e \rvert$ [e cm]
YbF	$< 1.05 \times 10^{-27}$ [55]
ThO	$< 1.1 \times 10^{-29}$ [79]
HfF^+	$< 4.1 \times 10^{-30}$ [38, 80, 81]

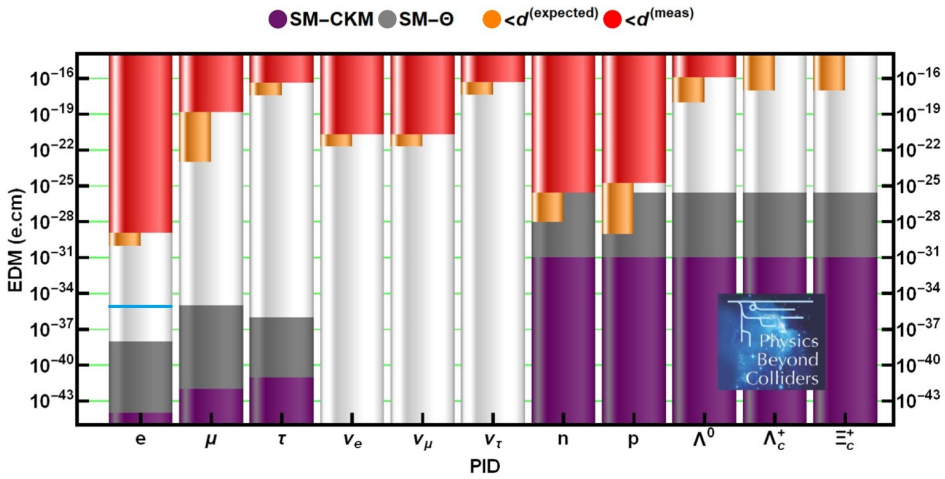

Figure 2.1: Review of EDM experiments [65]. Currently, the electron EDM (eEDM) has a larger gap between Standard Model values (SM-CKM) and the measured and excluded values compared to the neutron EDM (nEDM) and the proton EDM (pEDM). Upon finding a nucleon EDM, an independent measurement is required to distinguish the EDM and the $\bar{\theta}_{QCD}$ (SM-Θ) term. The blue line indicates the scale of SM-CKM terms present in paramagnetic systems employed for eEDM searches [64, 73]. These terms are indistinguishable from an eEDM if one such system is probed. Reaching beyond this scale requires probing different systems.

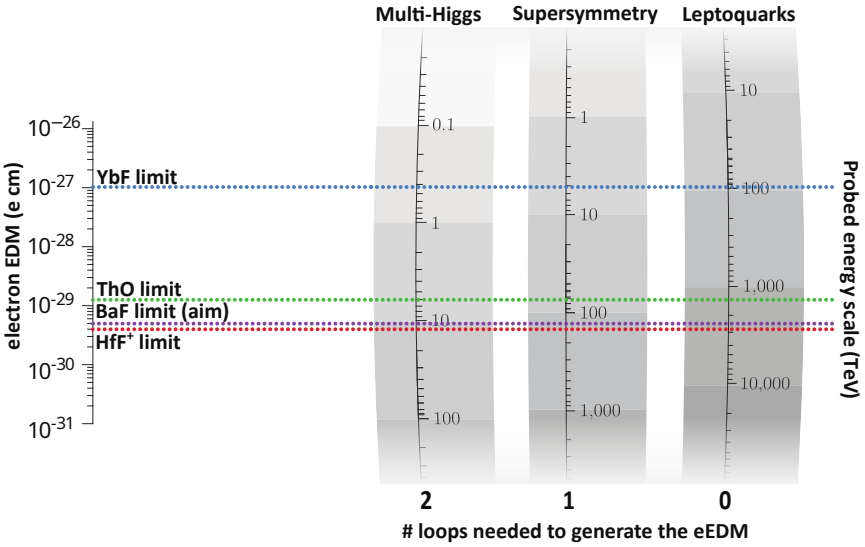

Figure 2.2: Theorized predictions on the eEDM depend on the number of loops required in a theory to generate an eEDM, and the energy scale. The interaction strength is assumed to be unity. Shown is a selection of recent eEDM searches performed with diatomic molecules, indicating an upper limit with 90% confidence: YbF (blue) [55], ThO (green) [79], HfF^+ (red) [38, 80, 81]. The estimated sensitivity of eEDM searches aimed for using BaF (purple) is shown for comparison [82].

2.3 eEDM sensitive search with BaF

The experiment uses a beam of BaF in external electromagnetic fields, where a BaF molecular quantum system moves at a velocity through the electromagnetic field in an eEDM sensitive (superposition) state. The state manipulation of the BaF molecule is executed using interactions with laser fields. The BaF molecule has been studied well and is described in [90–92]. Within the rather complex level scheme the eEDM experiment is concerned only with a few BaF molecular states. We will restrict our description here to the fully sufficient researched level scheme of the BaF ground state (see Fig. 2.3). A quantum mechanical description is arrived at through matrix diagonalization combined with Optical Bloch Equations (OBE) [91, 92].

Table 2.2: Scale of typical experimental frequencies.
* This frequency is estimated for $d_e \approx 10^{-28}$ e cm [91] and $|E| \approx \mathcal{O}(\mathrm{kV/cm})$.

Parameter	Frequency
$\omega^0_{HFS}/2\pi$	65.86 MHz
$\omega_{tensor}(\lvert E\rvert)/2\pi$	$\mathcal{O}(10\ \mathrm{kHz})$
$2\mu_B\lvert B\rvert/h$	$\mathcal{O}(100\ \mathrm{Hz})$
$2d_e\lvert E\rvert/h$	$\mathcal{O}(0.1\ \mathrm{mHz})$ *

The eEDM sensitive states are $|F=1, m_F=1\rangle$ and $|F=1, m_F=-1\rangle$ [i]. Their energy splitting is measured with spin precession. In the sequence of spin precession (Fig. 2.4) $|\psi_0\rangle = |0,0\rangle$ is a well defined starting state. A laser pulse of $\Omega_{PS}t = \pi$ (see Fig. 5.1), where t is the pulse duration, prepares the superposition state of $|1,+1\rangle$ and $|1,-1\rangle$. The superposition state is

$$|\psi\rangle = \frac{1}{\sqrt{2}}\left(|1,-1\rangle\, e^{-i\phi/2} + |1,+1\rangle\, e^{+i\phi/2}\right). \tag{2.2}$$

This state is time dependent because $\phi = \omega\tau$, where ω is the angular spin precession frequency associated with energy difference $\hbar\omega$. Phase ϕ evolves in electric and magnetic fields for a coherent interaction time τ. Depending on the phase accumulated in the superposition state, a second laser pulse $\Omega_{PS}t = \pi$ of the very same duration t, analyses the superposition state into either the $|F=0\rangle$ or the $|F=1\rangle$ state. The sequence ends when resonant laser light probes the population in these states.

In the superposition state of the $|1,+1\rangle$ and $|1,-1\rangle$ states (see Eq. 2.2), an accumulated phase ϕ arises from integrating over an energy difference $\Delta W(\tau)$ as in

$$\phi = \int_0^T \frac{\Delta W(\tau)}{\hbar} d\tau, \tag{2.3}$$

for coherent interaction time T, where $\Delta W(\tau)$ is affected by multiple parameters, such as the levels' Stark shifts. The energy difference $\Delta W(\tau)$ is due to the EDM Hamiltonian [24]

$$H = -(\mu_B \vec{B} + D^{\mathcal{P},\mathcal{T}} \vec{E}) \cdot \hat{F}, \tag{2.4}$$

[i] In the remainder of this section we use $|F, m_F\rangle$ unless denoted otherwise.

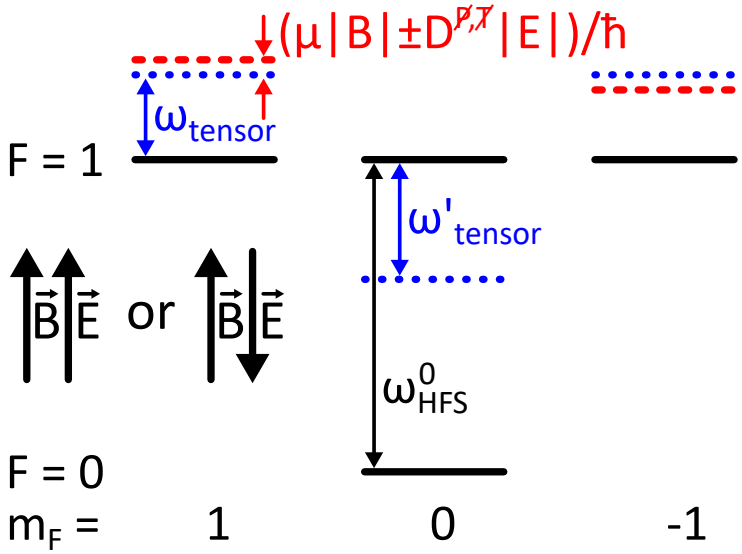

Figure 2.3: BaF ground state ($X^2\Sigma^+$, v=0, N=0, J=1/2) hyperfine structure in electric and magnetic fields [90–92]. Typical frequencies are in Table 2.2. The hyperfine splitting without fields is ω^0_{HFS}. Hyperfine structure becomes $\omega_{HFS}(|E|) = \omega^0_{HFS} + \omega_{tensor}(|E|)$ in an electric field, the $|F = 1, m_F = -1\rangle$ and $|F = 1, m_F = 1\rangle$ levels are shifted by a tensor Stark shift $\omega_{tensor}(|E|)$. The $|F = 1, m_F = 0\rangle$ level shifts by $\omega'_{tensor} = -2\omega_{tensor}$, a level avoided by careful laser polarization selection. With a magnetic field the Zeeman shift $\mu_B|B|/h$ is used to set the experimental working point of phase ϕ (see Eq. 2.3). An eEDM of $\mathcal{O}(10^{-28}\ \mathrm{e\,cm})$ corresponds to a frequency shift of $\mathcal{O}(0.1\ \mathrm{mHz})$ between opposite electric field directions [91]. Phase accumulation in $T = 1\ \mathrm{ms}$ is hence of $\mathcal{O}(1\ \mu\mathrm{rad})$. Sketches are not to scale.

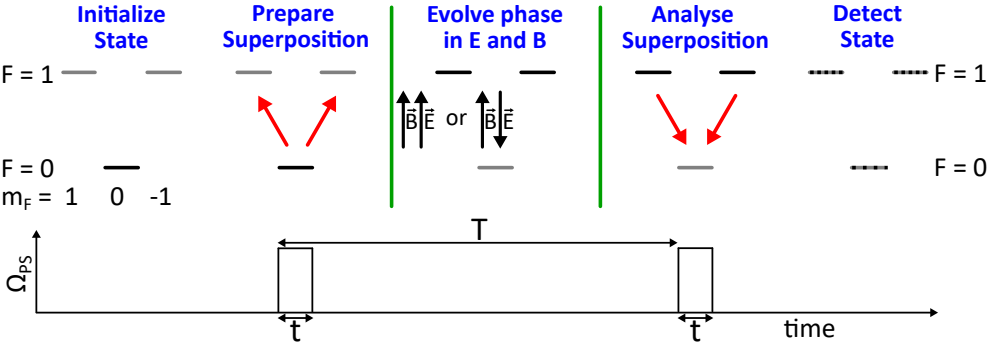

Figure 2.4: In the sequence of spin precession, the $|F = 0, m_F = 0\rangle$ state is a well defined starting state. A laser pulse of duration t prepares the superposition state of $|F = 1, m_F = 1\rangle$ and $|F = 1, m_F = -1\rangle$ (see Eq. 2.2). Phase evolves in electric and magnetic fields for a duration T. Depending upon the phase accumulated in the superposition state, a second laser pulse of duration t analyses the superposition state into the $|F = 0\rangle$ or the $|F = 1\rangle$ state. The sequence ends when resonant laser light probes the population in these states.

where μ_B is the magnetic dipole moment, $\vec{B}$ is the magnetic field, $D^{\not P,\not T}$ is the molecular sensitivity to parity and time-reversal violation [91], $\vec{E}$ is the electric field and

$$\hat{F} = \frac{\vec{F}}{|F|} \tag{2.5}$$

is the unit vector pointing in the direction of the total angular momentum. This Hamiltonian describes a measurement of a permanent EDM in a quantum system as an electric shift, in addition to the existing magnetic Zeeman shift. The phases accumulated during time T are

$$\phi_{\pm} = 2(\mu_B|B| \pm D^{\not P,\not T}|E|)T/\hbar, \tag{2.6}$$

for either parallel $(+)$ or anti-parallel $(-)$ applied magnetic and electric fields. The difference of these accumulated phases is

$$\Delta\phi_D = \phi_+ - \phi_- = 4D^{\not P,\not T}|E|T/\hbar. \tag{2.7}$$

From this the P,T-odd term $D^{\not P,\not T}$ can be extracted, to which the eEDM d_e is one contributor. The phase ϕ is experimentally measured by the population distribution of the hyperfine levels $|F=0\rangle$ and $|F=1\rangle$.

2.3.1 BaF experiment setup

The ability to distinguish state populations (see Fig. 2.5) is employed to detect the state of the molecules (see Fig. 2.4). This state detection leads us to define a signal sensitive to spin precession.

Optical detection of signals N_a and N_b are for transitions a and b respectively, with $N = N_a + N_b$. Transition a corresponds to $|F=0\rangle$, and transition b corresponds to $|F=1\rangle$. The probability of driving transition a is

$$P_a = \frac{N_a}{N} = \frac{N_a}{N_a + N_b}. \tag{2.8}$$

Measuring P_b in a similar fashion [ii] improves contrast. With both signals of P_a and P_b, these are best combined into asymmetry

$$\mathscr{A}_{ab} = \frac{P_a - P_b}{P_a + P_b} = \frac{N_a - N_b}{N_a + N_b}. \tag{2.9}$$

Besides improving contrast, the asymmetry is inherently normalized. In addition, P_a and P_b established in line with Eq. 2.8, combined with Eq. 2.9, can be used for crosschecks.

Within the context of a proposal to perform an eEDM sensitive search with BaF [82], a combination of experimental [93, 94] and theoretical [57, 95] efforts have been made. With at hand both a defined experimental sequence involving spin precession, and a definition of the resulting signal, we draw a schematic representation of essential ingredients of the experimental setup employing BaF (see Fig. 2.6). This schema is worked out, in the form of a setup and its use, in subsequent chapters.

[ii] With optical detection in a different location.

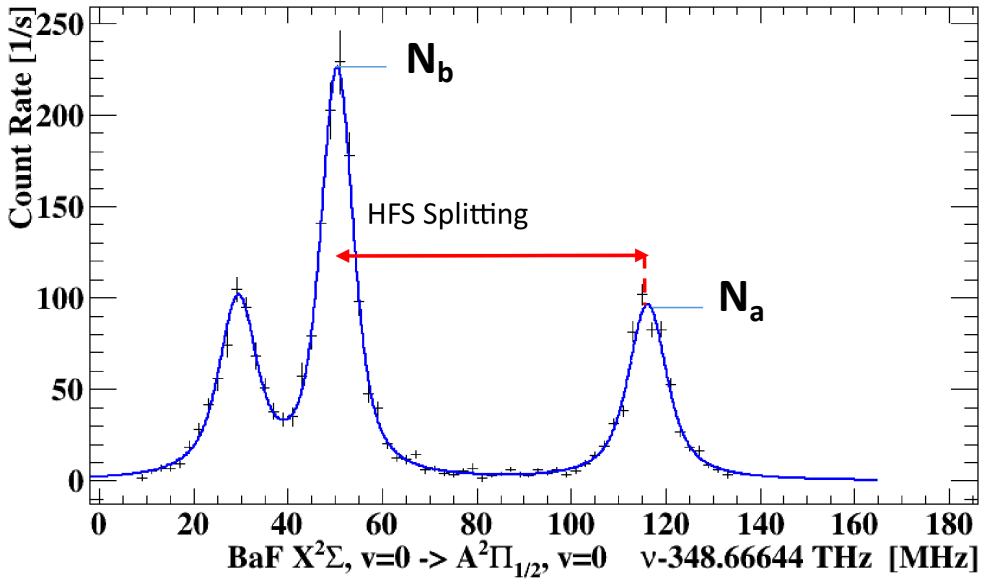

Figure 2.5: The experiment uses laser induced fluorescence and the ability to resolve different hyperfine transitions with high fidelity. Signal N_a corresponds to the amount in the $|F = 0\rangle$ state, signal N_b corresponds to $|F = 1\rangle$ [92, 96].

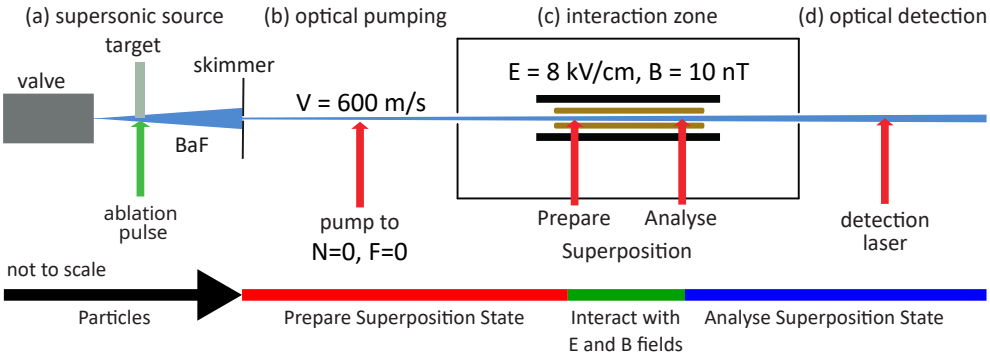

Figure 2.6: Supersonic BaF beam experiment with as essential ingredients in the experiment: (a) source (pulsed) of BaF molecules, (b) optical pumping to desired state, (c) interaction zone with homogeneous E and B fields, and (d) readout of spin precession through optical detection.

2.3.2 eEDM statistical sensitivity

The quantum statistics limited sensitivity σ_d to an electric dipole moment (EDM), assuming the eEDM to be to only P,T-violating source, can be estimated with [24]

$$\sigma_d = \frac{\hbar}{E\, A\, P(E)\, \varepsilon\, T\, \sqrt{n}}, \tag{2.10}$$

which consists of the external applied electric field E (below saturation level, i.e. $E < E_{sat} \cong 8.3\,\mathrm{kV/cm}$ for BaF [91]), the molecular enhancement factor A, with the molecular property $E_{eff} = E\,A$ [57]. Further parameters are the molecular polarization factor $P(E)$ as a function of external electric field E, the efficiency ε associated with, e.g. counting efficiency, apertures and contrast, the coherent interaction time T, and the total number of uncorrelated quantum systems n observed over the duration of the experiment T_{total}. For a beam of flux $\Delta n/\Delta t$ (Δt a generic time variable) you have to replace n by $(\Delta n/\Delta t) \times T_{total}$. The enhancement factor is a function of the external electric field, since the polarization factor is a function of the external electric field. The equation represents a fundamental quantum limit. The EDM can not be measured with greater precision. This is a consequence of the quantum mechanical Heisenberg uncertainty relation, here present in the relation between phase and number [97] in an EDM sensitive superposition state.

With numbers specific to our experiment, measuring the eEDM using a supersonic BaF beam as in Fig. 2.6, we can estimate the eEDM sensitivity to an order of magnitude for one day of measurement time:

- External applied electric field $E = 8\,\mathrm{kVcm^{-1}}$.
- Molecular enhancement factor $A \approx 8.1 \times 10^5$ [57].
- Polarization factor $P(E) \approx 0.5$ [57].
- A counting efficiency of 10^{-3} gives a total efficiency $\varepsilon \approx \sqrt{10^{-3}} \approx 3 \times 10^{-2}$.
- Length of fiducial volume $l = 600\,\mathrm{mm}$.
- Molecular beam forward velocity $v_z = 600\,\mathrm{m\,s^{-1}}$.
- Coherent interaction time $T = l v_z^{-1} = 1\,\mathrm{ms}$, assuming the coherence time is longer than the measurement time.
- A pulse rate $r_{pulse} = 10\,\mathrm{s^{-1}}$ and the number of BaF molecules per pulse $n_{pulse} \approx 5 \times 10^5$ [94] combine to a beam of flux $\Delta n/\Delta t \approx 5 \times 10^6\,\mathrm{s^{-1}}$.
- A duration of the experiment T_{total} of 1 day = 86400 s.
- Total number of uncorrelated quantum systems $n = (\Delta n/\Delta t) \times T_{total} \approx 4 \times 10^{11}$.

Taking data for one day results in an eEDM sensitivity of

$$\sigma_d \approx 10^{-26}\,\mathrm{e\,cm\,day^{-1}}. \tag{2.11}$$

Multiple possible improvements are in progress. Efficiency can be improved by an order of magnitude by increasing the solid angle, using photo diodes with larger quantum efficiency for light collection, and improving contrast by measuring both P_a and P_b (see Section 2.3.1). For a most sensitive experiment, the pulse rate r_{pulse} of the supersonic source should be adjusted to have the overall best sensitivity in the shortest experimental time. Assuming the number of particles per pulse n_{pulse} independent of the pulse rate r_{pulse}, the best eEDM result is to be expected for the highest achievable pulse rate in the experiment.

Another idea currently being pursued is to reduce the velocity v_z in the slow ultracold BaF beam experiment, which increases the measurement time. This is a possible

Table 2.3: Electric and magnetic field requirements for an interaction zone.

	Magnetic field	Electric field
Working point value	10 nT	8 kV/cm
Relative variation in the fiducial volume	10^{-2}	10^{-4}
Relative variation over time	10^{-4}	10^{-4}

improvement, provided the number of particles does not scale down faster than v_z^2. The beam flux will be improved by transverse laser cooling, from which we expect at least a 100x gain from currently ongoing activities. These near future improvements will yield at least one order of magnitude gain in sensitivity. A BaF source with substantially increased flux is a medium term ongoing development.

2.4 Requirements for an interaction zone

The discussion in this chapter leads to a number of design criteria for an actual implementation in an experimental setup. The design criteria require an interaction zone (see Fig. 2.6(c)) with well-defined electric and magnetic fields (see Table 2.3) in which eEDM sensitive searches can be performed. A more precise rendering of the interaction zone is drawn in Fig. 2.7. A vacuum system and optical access for lasers are critical for these searches. We have a beam of BaF molecules in the superposition state (see Eq. 2.2) moving through a central part of the setup (Fiducial Volume, about 50 cm long, 4 cm diameter). The main focus here is on creating, measuring, and con-

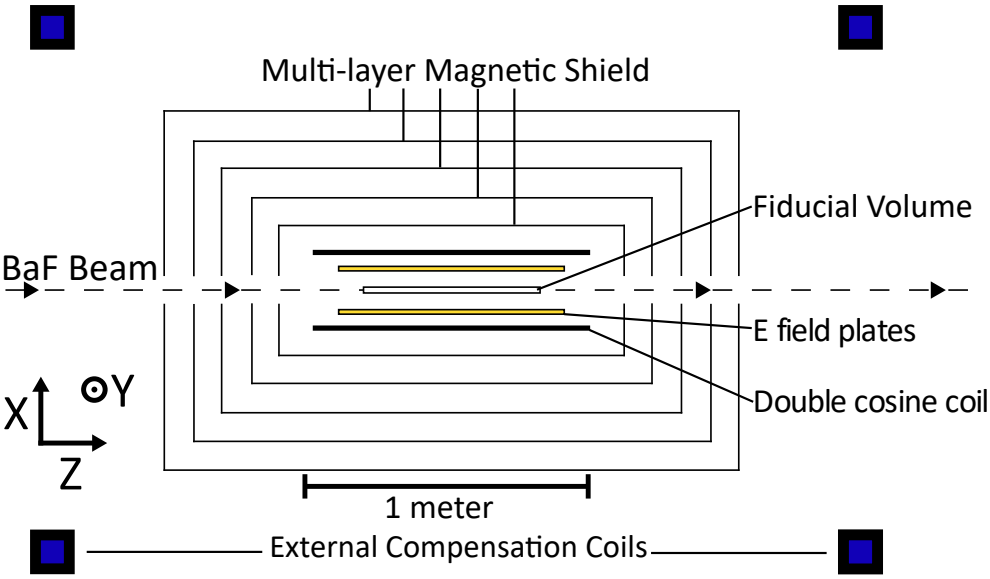

Figure 2.7: Interaction zone: an environment with electric and magnetic fields for eEDM sensitive searches.

trolling the electric and magnetic fields. There is an electric field $\vec{E} = 8\,\mathrm{kV/cm}\,\hat{x}$ in the fiducial volume, which is created by electric field plates. The electric field magnitude $|E|$ should have a relative variation over time less than 10^{-4} for opposite electric field directions (see Fig. 2.3) to avoid unbalanced Stark shifts. The electric field should also have a relative variation in the fiducial volume of 10^{-4}. The double cosine coil generates a magnetic field of $\mathcal{O}(\mathrm{nT})$ with 10^{-2} relative variation in the fiducial volume, parallel or anti-parallel to the electric field. For maximum eEDM sensitivity the magnetic field magnitude $|B|$ should be such that in the superposition state (see Eq. 2.2) a phase $\phi = 2\mu_B|B|T/\hbar = \pi/2$ is accumulated. The magnetic shield and the external compensation coils together are designed to reduce the earth magnetic field of $|B|_{Earth} \approx 70$ μT by 6 orders of magnitude to $|B|_{Shielded} = 70$ pT [iii]. The magnetic shield reduces magnetic field variation over time from outside to inside by 6 orders of magnitude, which results in a relative variation over time of $< 10^{-4}$.

With an interaction zone with the parameters in Table 2.3 a competitive eEDM experiment becomes feasible.

[iii] The nEDM collaboration at PSI has reached fields less than 150 pT designed for the n2EDM project [98], using a magnetic shield with 6 cubic μ-metal layers and 1 aluminium layer.

3 eEDM Experiment Setup

The interaction zone and in particular the homogeneous electric and magnetic fields are designed with the aid of the computational software package COMSOL [66]. The requirements are an $\mathcal{O}(10\,\mathrm{kV/cm})$ electric field and an $\mathcal{O}(\mathrm{nT})$ magnetic field.

The overview of the full setup is discussed in Section 3.1. Section 3.2 up to Section 3.6 are dedicated to the various aspects of magnetic field control necessary to reach the desired magnetic field: compensation coils outside the magnetic shielding, the magnetic shielding, holding field coils inside the magnetic shielding, and handling magnetic and non-magnetic materials. The approach to homogeneous electric field generation is treated in Section 3.7. The design and assembly of a vacuum system that provides a sufficiently low pressure ($p < 10^{-7}$ mbar) and takes the crucial magnetic properties of employed materials into account is treated in Section 3.8 (and Appendix B). Section 3.9 treats the final assembly of the components that are placed inside the magnetic shield. Section 3.10 is on the lasers and Section 3.11 is on the data acquisition system, both of which are necessary for the full working eEDM experiment.

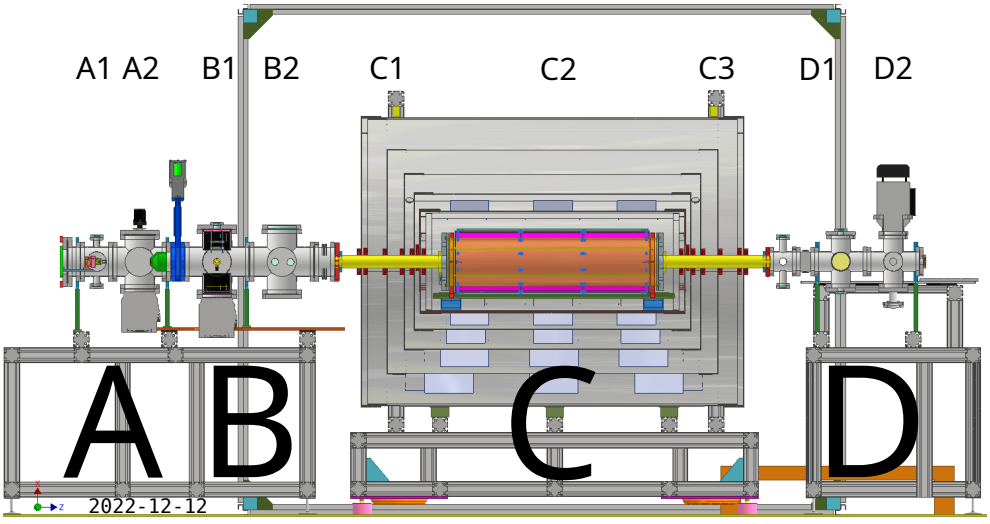

Figure 3.1: Setup of the eEDM experiment employing a supersonic BaF molecular beam. Molecules traverse a distance $l_{setup} = 3.84$ m from the EL-valve at A1 to state detection at the center of D1.

3.1 Full setup

We present the full setup (see Fig. 3.1) and a convention [i] for the coordinate system. The labeling of the functional sections is kept throughout the thesis. Starting from the molecular beam source we have the following sections:

A BaF molecular beam source:

- A1 Barium target ablation into a buffer gas.
- A2 Skimmer. Beam diameter $D_{skimmer} = 0.5\,\mathrm{cm}$.

B Molecular state preparation zone:

- B1 Detection of photon signal S_B.
- B2 Optical pumping out of hyperfine state $X^2\Sigma^+$, v=0, N=0, J=1/2, $|F = 1\rangle$.

C Interaction zone consisting of:

- C1 Titanium tube into magnetic shield.
- C2 Fiducial volume of experiment inside glass vacuum tube.
- C3 Titanium tube out of magnetic shield.

D Detection zone:

- D1 Detection of photon signal S_D. Detected beam diameter $D_{detected} = 2.0\,\mathrm{cm}$.
- D2 Entrance port for counter-propagating laser light beam driving the two-photon transition.

A In the BaF molecular beam source [99], a laser light pulse ablates atoms from a barium metal target (A1). The created plume interacts with an EL-valve (Even-Lavie valve) controlled buffer gas (98% Ar, 2% SF_6, 2 to 14 bar). In collision a BaF molecular beam is formed. A skimmer (A2) collimates the beam. It also reduces the gas pressure in subsequent vacuum parts.

B In the molecular state preparation zone a photon fluorescence signal S_B is employed to measure the number of molecules N_{mol} (B1). In a second step the initial state for the spin precession $X^2\Sigma^+$, v=0, N=0, J=1/2, $|F = 0\rangle$ is prepared (B2).

C The molecules enter the interaction zone. In the fiducial volume (C2) spin precession occurs in homogeneous electric and magnetic fields. While moving through the titanium tubes (C1 and C3), the BaF molecules are in a state that is robust against the $\mathcal{O}(\mu T)$ magnetic field changes present there, e.g. $X^2\Sigma^+$, v=0, N=0, J=1/2, $|F = 0\rangle$ or $|F = 1\rangle$ state.

D In the detection zone the number of molecules N_{mol} in the $X^2\Sigma^+$, v=0, N=0, J=1/2, $|F = 1\rangle$ state is determined by observation of resonance fluorescence (D1) of the hyperfine structure resolved $X^2\Sigma^+, N = 0 \rightarrow A^2\Pi_{3/2}, J = 3/2$ transition. The laser beam counter-propagating to the molecular beam enters the setup through an optical window (D2) on the molecular beam axis.

Timing accuracy is critical for the measurement precision. A Rb-clock (Stanford Research Systems FS725, relative frequency precision $\Delta\nu/\nu = 10^{-12}$) stabilized against a GPS satellite system is used as stable frequency and timing reference. This includes

[i] The provided convention, based on how a BaF molecular pulse moves through the setup over time, is a simple way of communicating the use and modification of the setup.

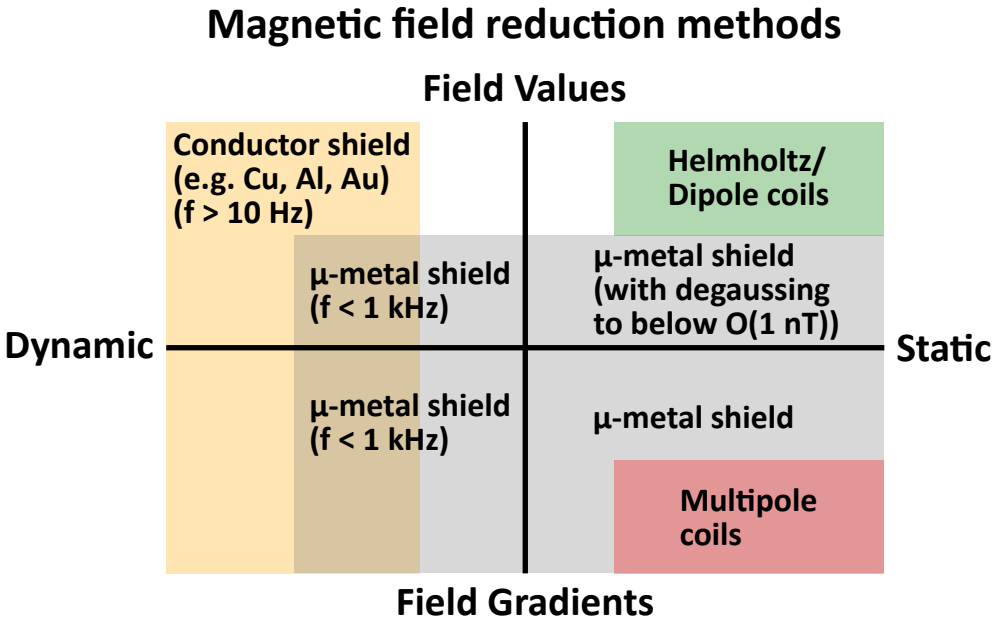

Figure 3.2: Different aspects of the magnetic field are optimally reduced with different methods. Dipole coils can compensate static magnetic field values. Multi-pole coils can compensate static gradients. A μ-metal magnetic shield is a passive method capable of reducing static field gradients, and is also capable of reducing the static field values. It is to a lesser extent (for frequencies below 1 kHz) even capable of reducing dynamic fields. With degaussing field values below 1 nT are accessible [98]. A shield consisting of bulk conductor material such as copper, aluminium, or gold, is a passive method capable of reducing all dynamic fields (for frequencies above 10 Hz).

the source EL-valve trigger, source ablation laser, the waveform generators responsible for the control of the light driving the two-photon transition, and time critical scaler counters inside VME crates that are part of the DAQ system.

3.2 Magnetic field control

EDM searches in molecules require well defined homogeneous magnetic fields, due to the Zeeman splitting of the involved states. An eEDM search using BaF molecules requires a field of $B \approx \frac{9\,\mathrm{ms}}{T} \times \mathrm{nT}$ for $\phi = \pi/2$ accumulated phase, where T is the coherent interaction time, and it requires a relative variation of about 1 %, in a cylinder shaped fiducial volume that is 50 cm long and has 4 cm diameter. A magnetic field of $B \approx 9\,\mathrm{nT}$ is required for a coherent interaction time of $T \approx 1\,\mathrm{ms}$ (see list 2.3.2). The requirements are more stringent when employing a slower beam of molecules in the future, e.g. $T \approx 20\,\mathrm{ms}$ requires $B \approx 450\,\mathrm{pT}$.

The laboratory magnetic field with a magnitude of $70\,\mu\mathrm{T}$ needs to be shielded. To bridge the gap between the laboratory field and the required field multiple methods (see Fig. 3.2) are combined in the experimental setup. Each of the methods is best

suited for a particular magnetic field range. Furthest from the fiducial volume are the six rectangular coils (see Section 3.3). Their purpose is to reduce the laboratory magnetic field by a factor of 10 to 7 μT. The multi-layer µ-metal magnetic shield (see Section 3.4) is exposed to the reduced field. It does the bulk of the magnetic field suppression. By combining layers of materials with maximally different relative magnetic permeability μ_r, i.e. µ-metal and air [ii], the magnetic field inside the µ-metal layer is reduced by a shielding factor. If the µ-metal layers are also placed at a sufficient distance from each other, their individual shielding factors multiply to a combined shielding factor. The envisioned shielding factor is of $\mathcal{O}(10^5)$, which corresponds to a 70 pT field inside the shield. The field is in part limited by the shielding factor. At low magnetic fields the remnant magnetization of the innermost µ-metal layers of the magnetic shield dominates, hence additional µ-metal layers do not reduce the magnetic field further. Inside the magnetic shield is space for magnetic holding field generation coils (see Section 3.5). One is a double cosine coil (see Section 3.5.1), which generates a holding field of $\mathcal{O}(\mathrm{nT/mA})$, with a relative variation of 2% of the full value in the fiducial volume. A coil is present to investigate the effects of transverse fields (see Section 3.5.2). To further reduce magnetic field gradients, an arrangement of multiple coils (see Section 3.5.3) has been studied [102, 103], but at this stage they need not yet be implemented. Passive methods employing µ-metal are preferred due to simplicity. In order to generate a sufficiently well defined field, specific materials (see Section 3.6) are to be avoided because of their magnetic properties.

3.3 Active compensation with external coils

Three pairs of rectangular coils (see Fig. 3.3) are implemented in the laboratory to reduce the magnetic field. One pair of coils generates a field parallel to the BaF beam direction, the Z direction. These coils have dimensions 2.5 m x 2.5 m, and are placed 3 m apart. The two pairs of coils that generate fields in the directions orthogonal to the BaF forward direction Z, generate fields in the X and Y directions. They have dimensions 3 m x 2.5 m, and are spaced 2.5 m apart. These are the maximum dimensions that fit symmetrically around the magnetic shield inside our laboratory. The coils have 25 windings each. With a magnetic field dependence on the current (see Table 3.1) and maximum current delivered by the power supplies (see Table 3.2), each pair of coils can simultaneously generate a magnetic field of 50 μT. At this generated field the power delivered to each pair of coils is of $\mathcal{O}(100\ \mathrm{W})$. By introducing a difference in current between a pair of coils, e.g. at +Z and -Z, a gradient can be obtained from these pairs of coils. In the case of the +Z and -Z coils, it would be a gradient of B_Z in the Z direction. This seems unnecessary given a characteristic feature of magnetic shields, in that they homogenize magnetic fields.

[ii] This implies that air with $\mu_r = 1$ and a superconductor with $\mu_r = 0$ can also be combined into a magnetic shield, since these also have very different magnetic permeabilities [100, 101].

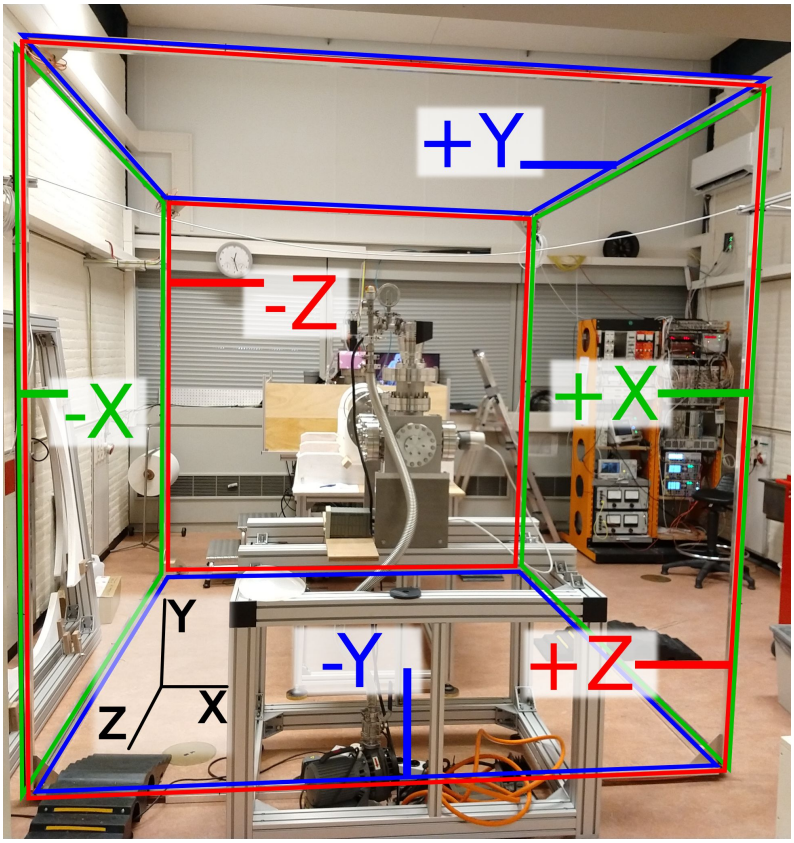

Figure 3.3: Six rectangular coils arranged in three pairs. The aim is to reduce the lab magnetic field by at least a factor 10 with the generated compensating field. The red coils, labeled +Z and -Z, generate a magnetic field B_{Z}, along the BaF beam axis. The blue coils, labeled +Y and -Y, generate a magnetic field B_{Y}. The green coils, labeled +X and -X, generate a magnetic field B_{X}, which in this picture is to the right. The generated field strength at the center of each set of coils is in Table 3.1.

Table 3.1: Magnetic fields B_{X}, B_{Y}, and B_{Z}, generated at the center of the coils in the laboratory, as a function of respectively the coil currents I_{X}, I_{Y}, I_{Z}.

$\Delta B_{\mathrm{X}}/\Delta I_{\mathrm{X}}$	$\Delta B_{\mathrm{Y}}/\Delta I_{\mathrm{Y}}$	$\Delta B_{\mathrm{Z}}/\Delta I_{\mathrm{Z}}$
7.4(1) μT/A	8.0(1) μT/A	5.5(1) μT/A

Table 3.2: Two Rohde&Schwarz HMP4040 power supplies were tested together. They can deliver maximum currents $I_{\mathrm{X},max}$, $I_{\mathrm{Y},max}$, $I_{\mathrm{Z},max}$.

$I_{\mathrm{X},max}$	$I_{\mathrm{Y},max}$	$I_{\mathrm{Z},max}$
8 A	8 A	9 A

3.4 Passive stabilization using a multi-layer μ-metal magnetic shield

The magnetic shield needs to satisfy several constraints, such as: reduce ambient magnetic field, homogenize residual magnetic field, fit inside the laboratory space, has to have sufficient internal space for a BaF molecular beam experiment, budget, ease of use. Several constraints are critical for the physics. Others are more related to the mechanical implementation. Our emphasis is on demands arising from physics constraints. The initial design related to the physics constraints, based upon calculations in COMSOL, is discussed in Section 3.4.1. The mechanical design and implementation produced by the magnetic shield manufacturer Sekels is discussed in Section 3.4.2.

3.4.1 Design and calculations

The initial design is implemented into the software environment COMSOL. Calculations indicate scaling of shielding levels with a perfectly soft ferromagnet. These show no hysteresis and remnant magnetization. They therefore give a lower bound on the shielding, and no information on the remnant fields of a real shield. The calculations help to eliminate designs that do not satisfy the desired magnetic field constraints, and help to distinguish sensitive from unimportant parameters.

All μ-metal layers are simulated with a cylindrical geometry. They have a surface geometry with an assigned thickness of 1.5 mm. The experimental constraints require an innermost layer with dimensions of 50 cm inner diameter and 120 cm length. The magnitude of the externally applied magnetic field is 7 μT. Due to cylindrical symmetry two sets of calculations were performed, with either a homogeneous external field along the axis $B_Z = 7$ μT or perpendicular to the axis $B_X = 7$ μT. No higher order multi-pole field was calculated, since a μ-metal magnetic shield has improved shielding performance with higher order multi-pole fields. The reasoning is as follows. An estimate of the shielding factor is

$$SF \simeq 1 + \frac{\mu_r n t}{D}, \tag{3.1}$$

with relative magnetic permeability $\mu_r = \mu/\mu_0$, μ-metal thickness t, diameter D of the shield, and n the order of the magnetic field, in the limit $D \gg t$ and $\mu_r \gg 1$ [104]. Taking a purely homogeneous (dipole at large distance) field where $n = 1$, gives a low end estimate of the shielding factor. Higher order multi-pole magnetic fields where $n > 1$, result in improved shielding [104] compared to a homogeneous field. Therefore calculations using a homogeneous external magnetic field form the most stringent test of a μ-metal magnetic shield, and no calculation with a higher order multi-pole field was performed. In addition, merely adding linear gradients already increases the number of sets of calculations by 5 to 7, excluding duplicates due to cylindrical symmetry.

The design parameters that were varied in the simulations are shown in Fig. 3.4. All parameters have values as shown in Fig. 3.4 in the conceptual design, unless stated otherwise in variations of those parameters. The cylindrical fiducial volume is the same for all calculations. A calculation takes 2 hours for one field direction. To take

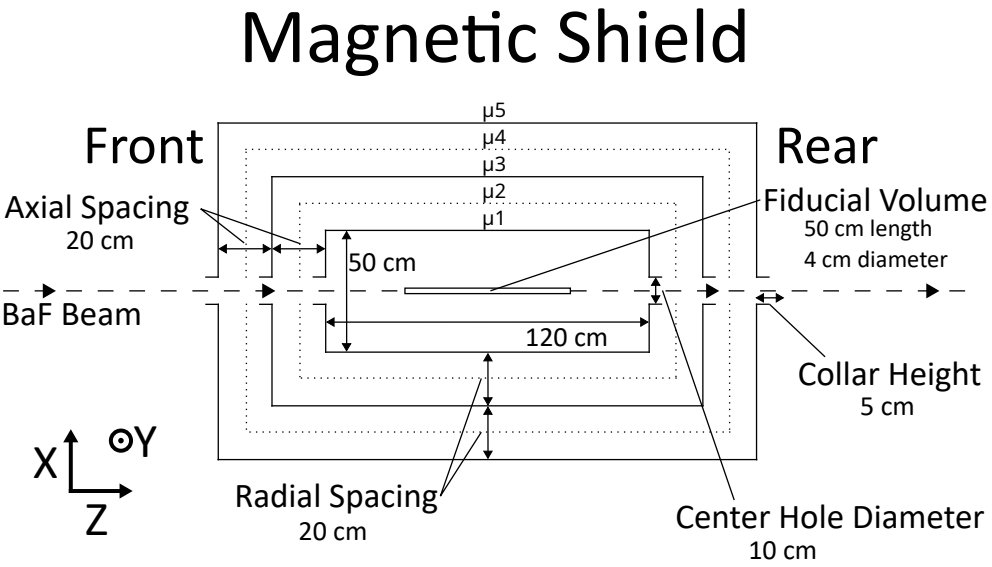

Variations

Axial Spacing	Radial Spacing	Center Hole Diameter	Collar Height	Number of layers
5 cm	5 cm	5 cm	0 cm	3 layers
10 cm	10 cm	10 cm	5 cm	5 layers
15 cm	15 cm	15 cm	10 cm	
20 cm	20 cm	20 cm	15 cm	

Figure 3.4: Conceptual design and considered variations of the magnetic shield. A 3 layer magnetic shield configuration, with the parameters used in all comparisons, except for the parameter that was varied. The 3 layer configuration consists of layers μ1, μ3 and μ5. The 5 layer configuration has the layers μ2 and μ4 added (dotted lines). The variations (green) are only for one parameter at a time. There is one exception: one set of calculations concerns the changing both axial and radial spacing, both with the same value. All other dimensions remain as in the reference design (black). For each variation we applied an external magnetic field $B_Z = 7\,\mu\mathrm{T}$ parallel or $B_X = 7\,\mu\mathrm{T}$ transverse to the magnetic shield cylinder axis. The collar height as drawn was part of calculations. But with these calculations it was found not to affect the magnetic field shielding, and it is therefore not implemented in the setup.

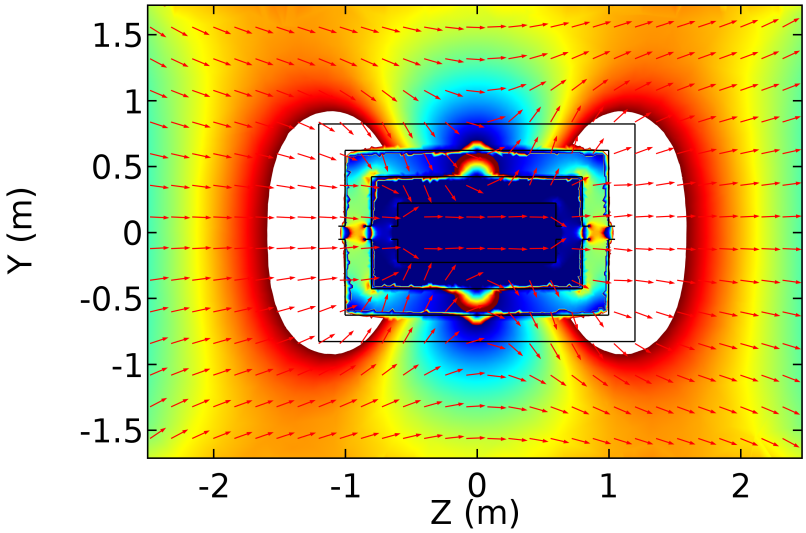

Figure 3.5: 2D image of the YZ plane (X=0 m) of a COMSOL calculation on a 3 layer shield, with an applied field $B_Z = 7\ \mu\mathrm{T}$. The color is a rainbow color where going from red to blue signifies a decrease in magnetic field, recursive for each order of magnitude. The white spots are magnetic fields above $10\ \mu\mathrm{T}$, which are not rendered. The arrows only give the direction, not the magnitude of the magnetic field, i.e. normal vectors. The arrows inside the innermost layer all point towards the right (+Z) direction, contrary to the fields anywhere else in the image. This shows that a magnetic shield does not only reduce the magnetic field, it also homogenizes the magnetic field. A magnetic shield reduces higher order multi-pole magnetic fields more strongly than dipole magnetic fields.

varying properties of μ-metal into account a calculation includes three different values of (relative) magnetic permeability μ_r: 20000, 40000, 80000. The full set of calculations is two such calculations for each of the 22 values of variations (see Fig. 3.4), one for each field direction (B_Z and B_X). Typical images from such calculations are shown in Fig. 3.5, Fig. 3.6 and Fig. 3.7. Multiple images such as these are analyzed and combined into the shown data in Fig. 3.8 and Fig. 3.9.

Variations only in axial spacing gives the same shielding performance for a B_X external magnetic field (see Fig. 3.8(b)). For a B_Z external magnetic field however, 5 cm spacing is insufficient (see Fig. 3.8(a)). In that case, both offset and inhomogeneity of the magnetic field are larger compared to calculations of larger dimensions. Based on this we established a design criterion that at least 10 cm of axial spacing is necessary to get magnetic isolation of different layers.

Fig. 3.8(c) and Fig. 3.8(d) depict that varying both axial and radial spacing in the same direction, changes magnetic shielding performance more than only varying the axial spacing. Fig. 3.8(c), for a B_Z external magnetic field, shielding performance is more sensitive (e.g. red versus yellow lines) to changes in dimension compared to Fig. 3.8(a). For the inhomogeneity of the magnetic field this change is less compared to the average value of the magnetic field. The improvement in shielding performance

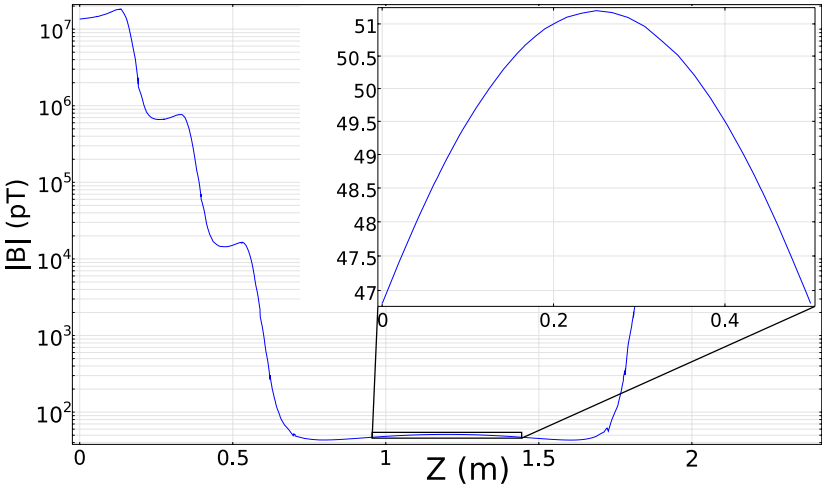

Figure 3.6: 1D image of the field along the Z axis (X=Y=0 m), of the same COMSOL calculation on a 3 layer shield as in Fig. 3.5, with an applied axial Z field of $B_Z = 7\ \mu\mathrm{T}$. The steep downwards slopes are at the locations of the ends of the respective shield layers. The inset concerns the field in the fiducial volume of the interaction zone.

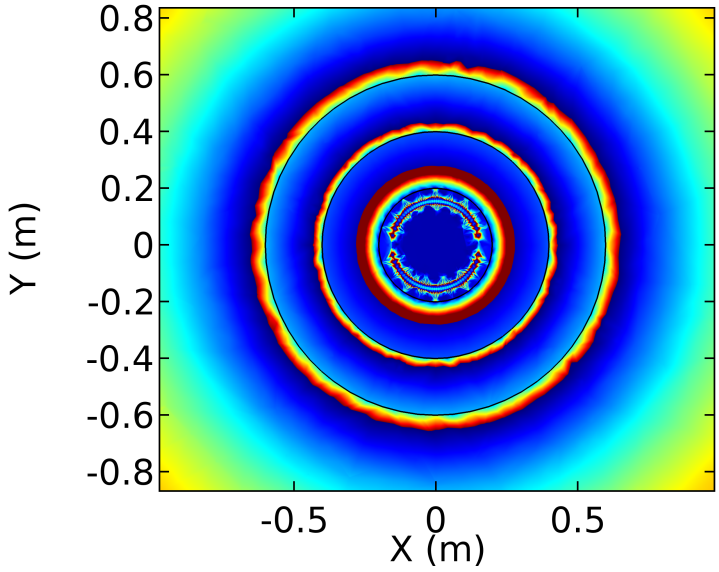

Figure 3.7: 2D image of the XY plane (Z=0 m) of a COMSOL calculation on a 3 layer shield with a double cosine coil inside. An external axial Z field of $B_Z = 7\ \mu\mathrm{T}$ as well as a field with the double cosine coil are applied. The color is a rainbow color where going from red to blue signifies a decrease in magnetic field, which repeats for each order of magnitude. The three black circles represent the three μ-metal layers of the shield. The noise around the coil is an artifact of trying to display the magnetic field across a dynamic range of 8 orders of magnitude, the field around the coil being the lowest field.

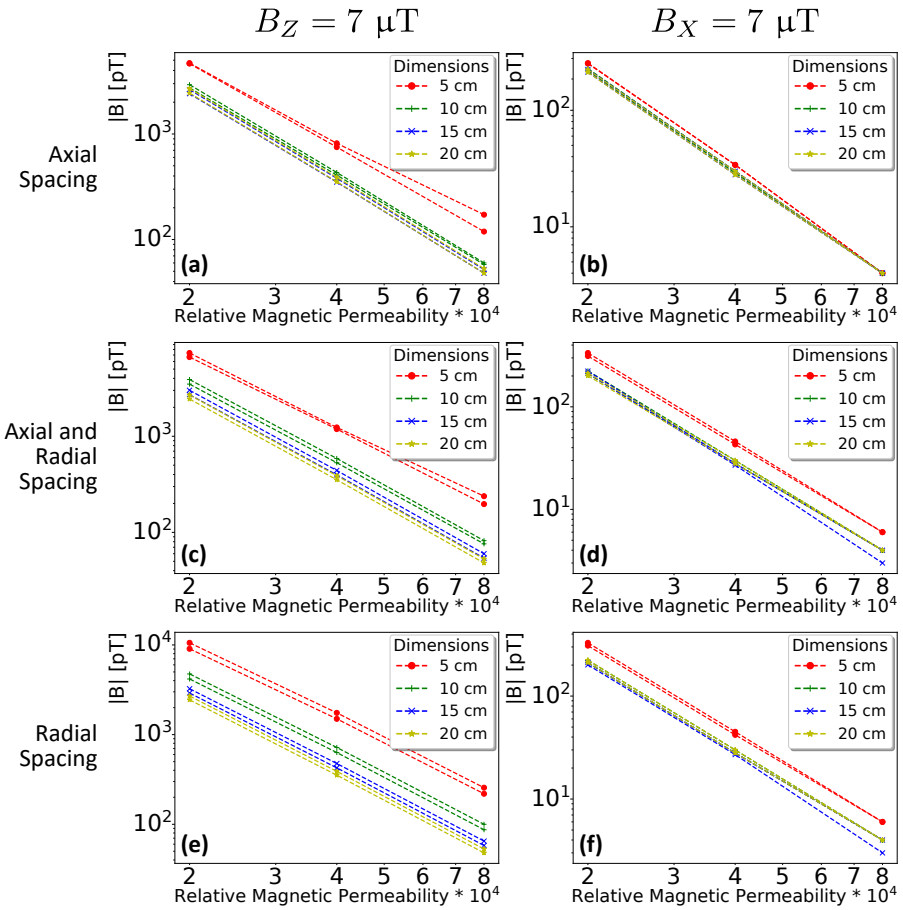

Figure 3.8: The minimum and the maximum magnetic field magnitude inside the fiducial volume is plotted. They indicate both the average value as well as the inhomogeneity in the magnetic field magnitude given some parameters. The dashed lines connect the symbols as optical assistance. (a) Variation in axial spacing. B_Z. An axial spacing of less than 10 cm decreases axial shielding performance. (b) Variation in axial spacing. B_X. Axial spacing has little effect on transversal shielding performance. (c) Variation in both axial and radial spacing together. B_Z. For both an axial and radial spacing less than 10 cm axial field shielding performance decreases most. The effect is mostly due to radial spacing (e) rather than axial spacing (a). (d) Variation in both axial and radial spacing together. B_X. For both an axial and radial spacing less than 10 cm transversal field shielding performance decreases most. The effect is mostly due to radial spacing (f) rather than axial spacing (b). (e) Variation in radial spacing. B_Z. For radial spacing less than 10 cm axial field shielding performance decreases the most. (f) Variation in radial spacing. B_X. For radial spacing less than 10 cm transversal field shielding performance decreases the most. Note that the vertical scales for the diagrams on the left are about an order of magnitude larger than those on the right. This is because of higher shielding performance for the B_X field compared to the B_Z field.

for increasing both axial and radial spacing from 5 to 10 cm compared to 10 to 15 cm and 15 to 20 cm, shows a decrease. The effect of spacing of the magnetic shield layers saturates between 10 and 20 cm. Fig. 3.8(d), for a B_X external magnetic field, shows sensitivity in magnetic shielding. The smallest simulated dimension of both axial and radial spacing, 5 cm, is less effective than the other dimensions in reducing the magnetic field. All other dimensions have the same shielding performance. The difference in minimum and maximum magnetic fields for 15 cm spacing and a relative magnetic permeability $\mu_r = 80000$, is an artifact of accuracy in the calculations. The resolution of this simulation is $1\ \mathrm{pT}$.

Magnetic shielding is more sensitive to only varying radial spacing compared to only varying axial spacing as well as varying both axial and radial spacing. This is only true for a B_Z external magnetic field (see Fig. 3.8(e)). In the case of a B_X external magnetic field the results for varying the radial spacing (see Fig. 3.8(f)) are the same as for varying both axial and radial spacing (see Fig. 3.8(d)).

To summarize the discussion of Fig. 3.8 for this geometry, we can rank by importance: varying only the axial spacing, varying both the axial and radial spacing, and only varying the radial spacing. The effectiveness of spacing on a magnetic shield, from most to least important, depends on

1. radial spacing
2. both axial and radial spacing
3. axial spacing.

From this we conclude that radial spacing should be maximized taking into account further practical constraints, such as the laboratory door size. Radial spacing should be at least 10 cm to insure magnetic isolation of layers. Axial spacing, though less important in terms of magnetic shielding, is most optimal when it is close to or equal to radial spacing. Other constraints, such as the distance between outside and inside the magnetic shield, are best with a minimal axial spacing.

Fig. 3.9(a) and Fig. 3.9(b) depict the effects on magnetic shielding of varying the center hole diameter. The B_X external magnetic field shows the same performance for all dimensions. In the case of B_Z external magnetic field, there is a small effect on shielding performance. The shielding performance is the same for 10 cm or less. Purely based upon magnetic shielding effectiveness, the smaller the hole, the better the shield, leads to a preferred minimal center hole diameter. But taking into account other constraints, such as the diameter of the beam pipe connecting the vacuum inside and outside the magnetic shield, the optimal dimension of the center hole diameter lies there where these other constraints are also satisfied.

Fig. 3.9(c) and Fig. 3.9(d) depict calculations on magnetic shielding effectiveness depending on varying the collar height. Neither for a B_Z nor for a B_X external magnetic field is there any effect of varying the collar height. It is not relevant for magnetic shielding, since there is no effect on shielding. Therefore we do not have to implement a collar.

In Fig. 3.9(e) and Fig. 3.9(f) we compare the shielding effectiveness for a 3 and a 5 layer shield assembly. For the 5 layer shield, one extra layer is added between layers μ1 and μ3 (μ2) and one extra layer is added between layers μ3 and μ5 (μ4) (see Fig. 3.4). The straight lines indicate a logarithmic law. The 5 layer assembly magnetic field reduction has a steeper slope than the 3 layer assembly for both a B_Z and a B_X external magnetic field. More important is that the shielding of the 5 layer assem-

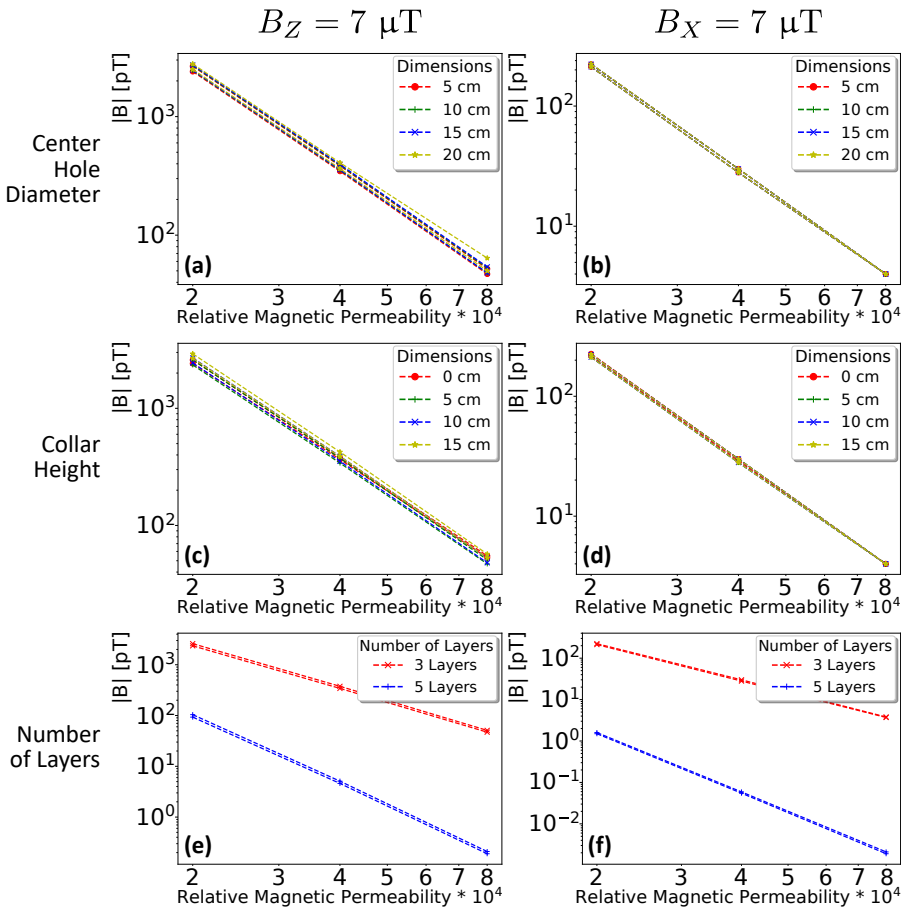

Figure 3.9: The minimum and the maximum magnetic field magnitude inside the fiducial volume is plotted. They indicate both the average value as well as the inhomogeneity in the magnetic field magnitude given some parameters. The dashed lines connect the symbols as optical assistance. (a) Variation in center hole diameter. B_Z. The center hole diameter has a small effect on axial field shielding. (b) Variation in center hole diameter. B_X. The center hole diameter has no effect on transversal field shielding. (c) Variation in collar height. B_Z. Collar height has no effect on axial field shielding. (d) Variation in collar height. B_X. Collar height has no effect on transversal field shielding. (e) Variation in the number of layers. B_Z. Going from 3 to 5 μ-metal layer yields a large increase in axial field shielding performance. (f) Variation in the number of layers. B_X. Going from 3 to 5 μ-metal layer yields a large increase in transversal field shielding performance. Note that the vertical scales for the diagrams on the left are about an order of magnitude larger than those on the right. This is because of higher shielding performance for the B_X field compared to the B_Z field.

Table 3.3: Magnetic shield cylinder inner dimensions from inside to outside. The lids fit over the cylinders. With lids the outer dimensions of the outermost aluminium layer (Al-out) are 1497 mm radius and 2008 mm length. Full technical drawings and in factory shield layer characterization of magnetic permeability are in Appendix C.

Layer	Material	t (mm)	Radius (mm)	Length (mm)	Pieces
Al-in	Aluminum	3	500	1300	1
Mu-1	μ-metal	3	516	1360	1
Mu-2	μ-metal	3	694	1420	1
Mu-3	μ-metal	3	894	1523	2
Mu-4	μ-metal	2	1146	1700	2
Mu-5	μ-metal	2	1461	1900	2
Al-out	Aluminum	4	1477	1960	1

bly can reach below $70\ \mathrm{pT}$ for a relative magnetic permeability $\mu_r > 25000$, where the 3 layer assembly can reach below $70\ \mathrm{pT}$ only for $\mu_r > 70000$. Considering the potential variation in material quality of μ-metal, relative magnetic permeability is between these levels, therefore a 3 layer shield can not tolerate variations in material quality where a 5 layer shield can. Based upon their greater tolerance for varying magnetic permeability, and based upon the fact that magnetic shield manufacturers recommend at least 4 or 5 layers for reaching below $1\ \mathrm{nT}$ fields (e.g. [105, 106]), we decided to use 5 μ-metal layers in our magnetic shield.

In conclusion, a μ-metal magnetic shield with an adequate shielding factor has to meet several conditions. The largest performance improvement arises from employing 5 instead of 3 μ-metal layers. Furthermore, a spacing between layers of less than 10 cm in both axial and radial directions would result in decreased shielding performance. Any increase of the end cap center hole diameter results in a small effect on the shielding. This leads to a preference for a smaller center hole diameter, balanced with the vacuum system and molecular beam diameter requirements.

3.4.2 Implementation

The magnetic shield calculations were used to generate a design which was given to the manufacturer Sekels [105]. The final design provided and implemented by Sekels contains 5 μ-metal magnetic shielding layers and 2 aluminium mechanical support layers (see Table 3.3). Full technical drawings and shield layer characterization in the factory of magnetic permeability are presented in Appendix C. The inner 2 μ-metal layers Mu-1 and Mu-2 are made as full cylinders, with degaussing coils initially installed on Mu-1 only. Degaussing is about isotropic magnetization, which amounts to demagnetization [107, 108]. The outer 3 μ-metal layers Mu-3, Mu-4, and Mu-5 consist of 2 half cylinders because of the size of the available annealing ovens at the manufacturer's site.

The magnetic shield was installed on an aluminium frame in the laboratory (see Fig. 3.10). It was transferred to the laboratory (see Fig. 3.11) using airpads [iii]. Three supports on the frame are shaped to support the mass of the magnetic shield [iv]. Braces

[iii] For more details see Appendix F.

[iv] Its mass including all experimental components installed inside is about 1000 kg.

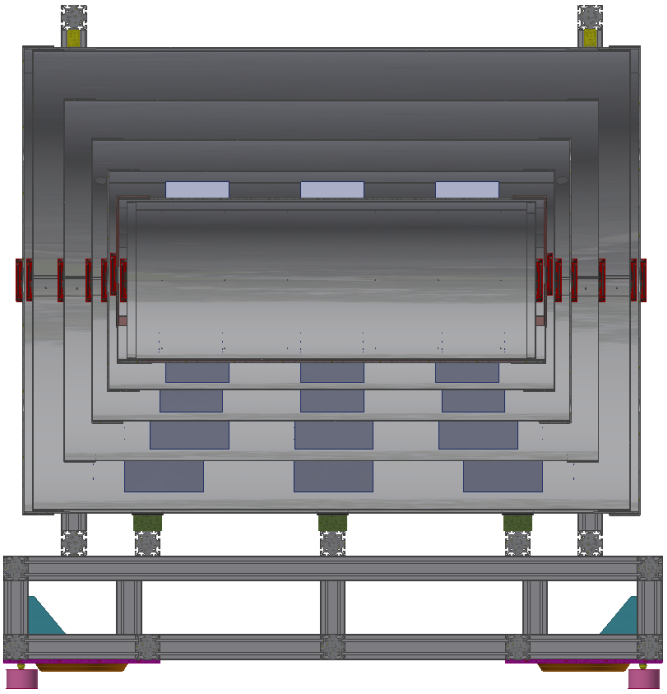

Figure 3.10: Magnetic shield drawing. The shield is supported by an aluminium Boikon frame from below. The frame is supported in normal operation by 4 legs. It can be moved using 4 airpads. On this frame are 3 supports, which are cylindrically shaped to support the weight of the shield from below with minimal stress. Close to the lids are also 2 braces around the sides and top of the magnetic shield, which provide magnetic shield cylinder roundness. The 3 supports and the 2 braces are separated from the magnetic shield with Sorbothane rubber, with the purpose of reducing mechanical stress from uneven surfaces, as well as reducing vibrations.

are installed around the magnetic shield. Their purpose is to maintain the roundness of the cylindrical shape. Besides preserving magnetic properties, maintaining the roundness of the cylinders makes dismounting and re-installing the magnetic shield lids possible when parts are installed inside.

3.5 Magnetic holding field generation

The magnetic holding field is primarily generated by a double cosine coil (see Section 3.5.1). A coil is installed to investigate the effects of transverse fields (see Section 3.5.2). Approaches for additional compensation coils with the purpose of improving the homogeneity of the holding field are discussed (see Section 3.5.3).

3.5.1 Double cosine coil to generate magnetic holding field

The homogeneous holding field of up to 120 nT inside the magnetic shield is generated by a cosine coil. A cosine (Θ) coil is a coil with a wire distribution arranged

Figure 3.11: Magnetic shield installed in laboratory.

on a cylinder that yields a current density with a $\cos\theta$ dependence on the cylinder. θ is the angle as defined in Eq. 3.2 or Eq. 3.3 with respect to the y-axis (see Fig. 3.12 and Fig. 3.13). This satisfies the purpose of generating a homogeneous magnetic field transverse to its cylinder axis. We adapt this to our experiment into a double cosine coil, two cosine coils of different diameters combined. Through COMSOL calculations, an electrical design has been made including manufacturing tolerances. This electrical design was translated into a device at the Nikhef Workshop. Magnetic properties of the double cosine coil, while inside the magnetic shield, have been measured using flux gates as well as using molecules in a magnetic field sensitive state.

The wire distribution required for a cosine coil has for each wire the angle

$$\theta_j(N) = \arctan\left(\left[\left(\frac{N}{2j-1}\right)^2 - 1\right]^{-\frac{1}{2}}\right), \tag{3.2}$$

where N is the total number of wire loops, N being an integer multiple of 2, and where j runs from 1 to N/2 describing the upper right quadrant starting from the y-axis [103]. Other quadrants can be found through reflections in both orthogonal planes transverse to the cylinder axis. The wire distribution $\cos(\theta_j(N))$ can be used as input into COMSOL, with as a result a model that can with minor modifications be translated into a mechanical design.

Such a current distribution yields a magnetic field transverse to the coil cylinder axis. It is a proven method for generating homogeneous magnetic magnetic fields with wires distributed along the cylinder. It saves space for setups with a high degree of cylindrical symmetry, e.g. inside a cylindrical μ-metal magnetic shield around a cylindrical vacuum system. The cosine coil has been used in a variety of experiments, one of which concerns EDM searches with Xe [51].

This conceptual design of a cosine coil as described above, has several properties which are suboptimal to the experiment, which requires $\mathcal{O}(\mathrm{nT})$ magnetic fields with $\mathcal{O}(\mathrm{pT})$ fluctuations. These properties are:

1. A working experiment requires currents flowing through the end-caps.
2. Fields of $\mathcal{O}(\mathrm{nT})$ with $\mathcal{O}(\mathrm{pT})$ fluctuations, require $\mathcal{O}(\mu\mathrm{A})$ currents with even smaller fluctuations $\mathcal{O}(\mathrm{nA})$ over time. This is for N=80 and a cylinder radius of 15 cm.
3. It is limited in the number of wires, with fewer wires resulting in larger spatial inhomogeneities.

Property 1, the presence of end-caps, is not a problem when the experiment is offline. Removable end-caps have been used before [103]. It is a problem when the experiment is online, since end-caps block axial access, which is indispensable for a (molecular) beam experiment. Properties 2 and 3 are trade-offs in a cosine coil, were a design is limited by magnetic field fluctuations in either time or space. Combining two cosine coils with different diameters, forming a double cosine coil, ameliorates all these properties.

A double cosine coil is formed by combining two cosine coils with different diameters. The wire distribution required for a double cosine coil has for each wire, of both inner and outer coil, the angle

$$\theta_j(N) = \arctan\left(\left[\left(\frac{N}{4j-2}\right)^2 - 1\right]^{-\frac{1}{2}}\right), \tag{3.3}$$

where N is the total number of wires in one coil layer [v], N being an integer multiple of 4, and where j runs from 1 to N/4 describing the upper right quadrant starting from the y-axis. Other quadrants can be found through reflections in both orthogonal planes transverse to the cylinder axis. The wire distribution $\cos(\theta_j(N))$ can be used as input into COMSOL, with as a result a model that can with minimal modification be translated into a mechanical design.

The principle of operation of a double cosine coil can be shown by taking the current distribution as in Fig. 3.12, and taking the wires infinitely long. It is formed by two cosine coils in a Russian doll configuration: they have the same length, and the same angular wire distribution, but a different diameter, equal current magnitude,

[v] N is also the number of miniloops.

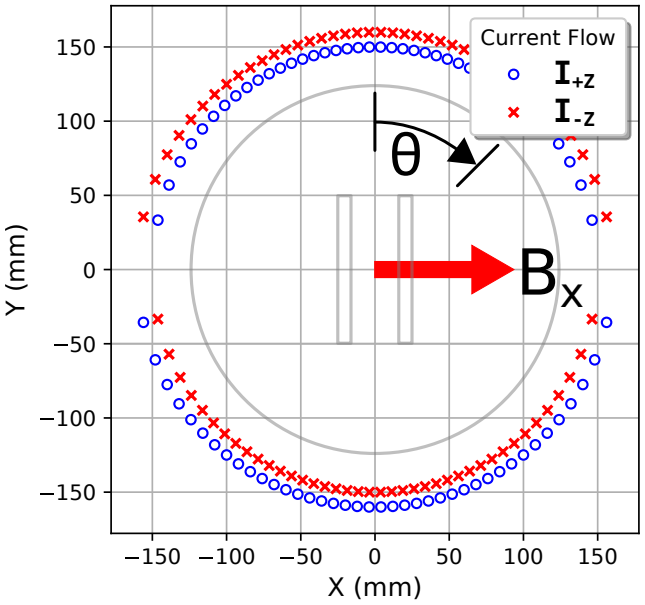

Figure 3.12: Double Cosine Coil, drawing of principle. Projection on a plane perpendicular to the cylinder axis, with all currents flowing parallel/antiparallel to this long axis as represented by I_{+Z}/I_{-Z} (out of/into page). All currents have equal magnitude. There are 80 "pairs" of an inner and an outer layer current in this drawing. The inner layer of currents is closer to x=y=0 than the outer layer, which due to the currents being of equal magnitude results in a net magnetic field $\vec{B} = B_x\hat{x}$ at x=y=0.

but opposite current direction. At the center of the double cosine coil, the resulting magnetic flux density $\vec{B}_{DCC}$ is the difference of the inner coil $\vec{B}_{IC}$ and outer coil $\vec{B}_{OC}$

$$\vec{B}_{DCC} = \vec{B}_{IC} - \vec{B}_{OC}. \tag{3.4}$$

For a double cosine coil of infinite length, on the cylinder axis (x=y=0 mm in Fig. 3.12), since a single infinite wire generates a magnetic field $\vec{B}_{wire} = \mu_0 I/(2\pi s)\hat{\phi}$ at distance s [109], and since radius $R_{OC} > R_{IC}$, we can say

$$\vec{B}_{DCC} = (|B_{IC}| - |B_{OC}|)\,\hat{x} = |B_{IC}|\left(\frac{1}{R_{IC}} - \frac{1}{R_{OC}}\right)\hat{x}. \tag{3.5}$$

The two superposed cosine coils produce a net magnetic field in direction $\hat{x}$. This is the same direction as the magnetic field produced by the inner coil, and opposite in direction produced by the outer coil. For the coil configuration as in Fig. 3.12, the coils have radius $R_{IC} = 150$ mm and $R_{OC} = 160$ mm, hence

$$\vec{B}_{DCC} \approx |B_{IC}| \times 4 \times 10^{-3}\hat{x}. \tag{3.6}$$

Compared to the cosine coil, the double cosine coil has a number of benefits:

1. There is no need for end-caps in a double cosine coil, since all wires can be incorporated in the cylinder tube. The result is full axial access for beams, vacuum chambers and other equipment.

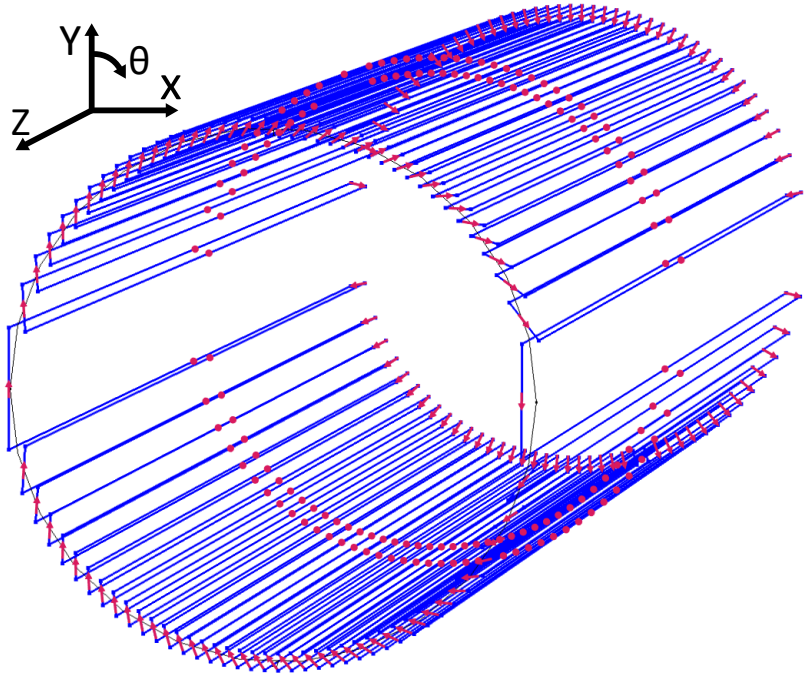

Figure 3.13: Double cosine coil: optimized coil shape. The red arrows represent the direction of current. For cylindrical coordinates with the postive z axis out of the drawing plane, the longitudinal wires, parallel to the z axis, form the coil connected on the +z and -z locations. The connections on the -z side are radial, merely forming a ”miniloop” of 2 longitudinal wires, 1 of the inner and outer layer each. The connections on the +z are slanted so that they connect the ”miniloops”. The slanted connections yield a net current equivalent to circular wire at +z, resulting in a magnetic field along the z axis. This is compensated for by a circular wire (black) with the opposite current flow.

2. The operational current for a small field can be higher than in the cosine coil (see e.g. Eq. 3.6) since the magnetic field is the difference between two cosine coils. The result is better magnetic stability in time.
3. A larger number of wires/wire pairs can be implemented, if it improves homogeneity, which can be offset by reducing the radial distance between the inner and outer coils.

This makes the double cosine coil a better fit for the experiment.

A full single circuit model of the double cosine coil was arrived at inside COMSOL (see Fig. 3.13). The red arrows represent the direction of current flow. Fig. 3.12 is a cut at the plane z=0 mm (for z the axial direction). The coil is 1 meter long. Fig. 3.13 also indicates how to connect all wires, to get a functioning double cosine coil. At one end, the wires of inner and outer coils are connected radially, forming small loops. At the other end, these small loops are connected to each other through non-radial connections. Connecting all small loops like this gives 1 net loop at this latter side along the θ-direction of the coil cylinder, resulting in an additional axial field there.

This can be compensated for by introducing a single compensating loop at the end with the non-radial connections. Except for a connection to a power supply through a twisted pair and the single compensating loop being separate, the coil in Fig. 3.13 is electrically equal to Fig. 3.14.

A double cosine coil inside a magnetic shield interacts with the μ-metal. We compare a double cosine coil in air only with a double cosine coil in a μ-metal cylinder layer (μ_r = 80000, t = 1.5 mm) with 50 cm radius and 130 cm length, by performing calculations for each in COMSOL. Two properties in the fiducial volume of the experiment change with the addition of the μ-metal cylinder layer. First of all, there is a 35% reduction in magnetic field magnitude. Second, the gradients along the z-direction for all magnetic field components are reduced, as the inhomogeneity goes from 5% to 2%. Gradients in the transverse direction are below the resolution of the calculations. Since we are primarily interested in minimizing inhomogeneity, placing the double cosine coil into a μ-metal magnetic shield is predicted to improve its performance in generating a homogeneous magnetic holding field.

The coil is mounted on the outside of the glass tube (see Fig. 3.17) with soft plastic spacers. The current source that has been employed is a precision Knick device [vi] with resolution at $I = \pm 100\ \mathrm{mA}$ of $\sigma_I = 100\ \mathrm{nA}$ or alternatively a DM MCS [vii] 8 channel current supply, with resolution at $I = \pm 4\ \mathrm{mA}$ ($I = \pm 40\ \mathrm{mA}$) of $\sigma_I = 125\ \mathrm{nA}$ ($\sigma_I = 1.25\ \mu\mathrm{A}$). The coil has a linear sensitivity $\Delta|B_{DCC}|/\Delta I_{DCC} \approx \mathcal{O}(\mathrm{nT/mA})$ inside the magnetic shield. It is characterized in Section 4.4. [viii] The coil combined with the power supplies fulfills requirements of setting the magnetic field up to $\pm\mathcal{O}(10\ \mathrm{nT})$ with better than pT resolution.

3.5.2 Coil for transverse field effect investigation

An additional coil is implemented for investigating how the tensor Stark effect affects the sensitivity to magnetic fields transverse to the electric field. These include additional field components from the double cosine coil, the magnetization of the magnetic shield, and the motional magnetic field. It a single wire with a rectangular shape around the vacuum system, which is mounted at the height of the BaF beam. It deviates from the rectangular shape at the front and the back, due to the presence of titanium tubes through which the BaF beam enters and exits the vacuum system inside the interaction zone. The coil generates a vertical field in the setup

$$B_y = \frac{\Delta B_y}{\Delta I_y} I_y, \tag{3.7}$$

with $\frac{\Delta B_y}{\Delta I_y}$ the linear sensitivity to current in $\mathrm{nT\ mA^{-1}}$, and I_y the current in mA. It is characterized in Section 4.4.

3.5.3 Active compensation with internal coils

If higher homogeneity is required, additional compensation and shimming coils can be implemented. This is true for any geometry, but the experiment concerns a cylin-

[vi] Knick Stromgeber Typ J42.

[vii] DM Technologies Multichannel Current Source, see www.dmtechnologies.eu.

[viii] $\vec{B}_{DCC} = |B_{DCC}|\hat{B}_{DCC}$ with $\hat{B}_{DCC} = \hat{x}$.

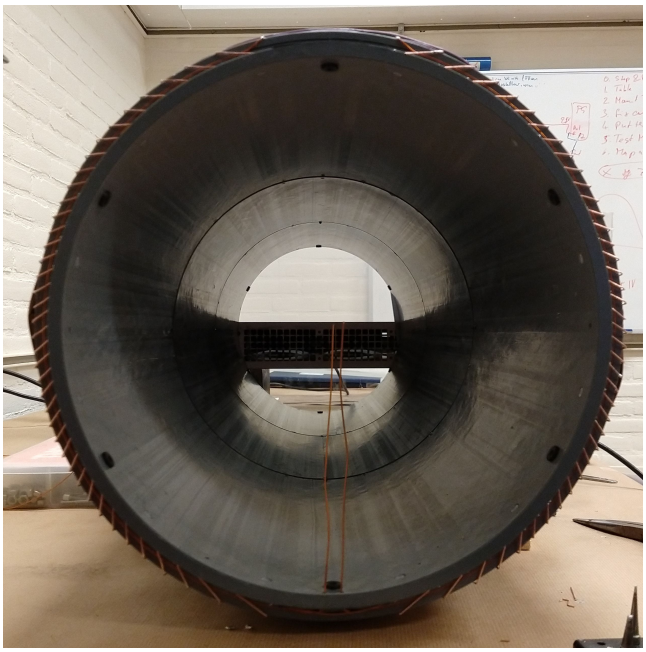

Figure 3.14: Physical realization of the double cosine coil. The magnetic field is here along the vertical axis. Two etched copper coated Kapton foils, with 2 mm wide copper tracks, conduct current along the coil length, one on the inside and one on the outside. By soldering with 0.75 mm copper wires these copper tracks are connected to each other. The interloop copper wire connections on this side are slanted so that they connect all miniloops. The intraloop copper wire connections on the opposite side are radially connected. There is an additional single loop of wire that runs around the whole coil at this side of the coil barrel, which compensates the net axial field resulting from all not radially running interloop connection wires. It is in series with the rest of the coil. The wires in front sticking into the inside of the barrel, are connected to a power supply for operation of the coil.

drical geometry. All approaches require a measurement of the magnetic field. One approach uses (multiple) dedicated coils to counteract specific magnetic field components. This approach was successfully applied in the Xe-EDM experiment [103]. A different approach uses generic coils to target all magnetic field components up to some order. Such a generic coil uses a set of multiple smaller circular or rectangular loops mapped onto a cylinder. One example uses 48 circular loops (6 rows of 8 loops) [110]. Therein it is stated that such an approach has as an essential prerequisite the careful calibration of the coils. This is subsequently used in modeling of the coil configuration to attain the desired field in a single step. The relevance of the latter approach in the experiment was investigated [102].

Table 3.4: Summary table of allowed materials, depending on location.

Location	Allowed materials
Inside inner magnetic shield layer	Plastics, rubber, glass, several titanium alloys
Inside shield, outside inner layer, or lids removed	Aluminium, phosphor-bronze
Outside shield, up to 1 meter from shield	Slightly ferromagnetic stainless steel (A4) washers, nuts, and bolts
Inside lab, further than 1 meter from shield	Ferromagnetic materials should not move
Outside lab	No constraints, monitor if a large magnetic field source is present (e.g. particle accelerator)

3.6 Non-magnetic materials

Magnetic materials in the surroundings of the experiment can spoil the magnetic field homogeneity. Therefore we only employ certain materials depending on their magnetic susceptibility and their location in the laboratory (see Table 3.4).

Inside the magnetic shield, close to the fiducial volume, we prefer using materials with high electrical resistivity (insulators and semiconductors). We only employ materials with very low dia- or paramagnetism. High resistivity reduces eddy currents [ix] and electronic noise. A variety of plastics, as well as rubber, glass and many titanium alloys satisfy this. While aluminium is only slightly paramagnetic (volume susceptibility of $O(10^{-5})$), its low resistivity of $O(10^{-8}\ \Omega\mathrm{m})$ can result in electronic noise.

Inside the magnetic shield but outside the inner layers of the magnetic shield, materials should merely not be ferromagnetic. Therefore aluminium can be used. For mechanical work in the laboratory we have phosphor-bronze tools. When the end-caps are dismounted from the magnetic shield, ferromagnetic materials must be kept away from μ-metal layers, both the cylinders and the end-caps, to prevent their accidental magnetization.

Outside the magnetic shield, but within 1 meter of the magnetic shield, slightly ferromagnetic materials are tolerated. This includes A4 stainless steel washers, nuts and bolts as well as stainless steel vacuum chambers, e.g. material numbers 1.4429 and 1.4435 in the vacuum manual from Pfeiffer [111].

All volume inside the laboratory with a distance to the magnetic shield of more than 1 meter, or at a distance from the magnetic shield larger than the largest dimension of an object, can contain any amount of ferromagnetic material, as long as ferromagnetic materials are not moved after installation and field calibration.

Material outside the laboratory has no constraints on ferromagnetic materials. Effects of co-located laboratories using very high magnetic fields, above $1\ \mathrm{T}$ must be monitored, e.g. a particle accelerator.

All materials have to be evaluated for their magnetic properties before installation in the setup. By moving materials past a flux gate (see Chapter 4) evaluation is possible to nT scale.

[ix] Which are also called Foucault's currents.

3.7 Electric field generation

An eEDM measurement requires a homogeneous electric field of $\mathcal{O}(10\,\mathrm{kV/cm})$. Based on calculations (see Fig. 3.15), and the molecular beam acceptance up to 4 cm diameter, we decided for a configuration of 2 Indium Tin Oxide (ITO) coated glass plates at 4 cm distance. The assembly process (see Appendix D) yields the configuration displayed in Fig. 3.16. Estimates indicate a $\lesssim 10^{-3}$ level relative electric field variation in the region where the molecular beam passes between the plates. The frame design is such that a central third conductive plate could be added at a later stage, yielding opposing electric fields, one parallel and one anti-parallel to the magnetic holding field. This affords improved continuous probing of electric field systematics. With the third plate, estimates indicate a reduction in relative electric field variation to $\lesssim 10^{-4}$ level. The electric potential is provided by two High Voltage (HV) power supplies (Iseg HPn 300 106 and HPp 300 106). They are connected through a custom switchbox (see Appendix E) to the field plates for electric field reversal and monitoring. The time required for electric field reversal depends on the used resistors and the capacity of the used cables [112].

3.8 Vacuum system

A glass tube of 25 cm outer diameter, 110 cm length, 1 cm wall thickness, holds the electric field plates. Glass is non-magnetic. It also does not add to electron noise like a metal chamber would. The goal is to reach a residual pressure of $p < 10^{-7}\mathrm{mbar}$, since that is the pressure at which BaF molecules are transmitted through the vacuum system. The glass tube is closed with 2 titanium endcaps (see Fig. 3.17). The material was chosen for minimal distortion of the magnetic field. These are designed with flexible mechanical mounting to the glass tube, to accommodate manufacturing tolerances of the glass. Each large endcap has a central part for mounting the beam pipe, and 6 for optical fiber- and HV-feedthroughs. Each unused small hole is closed with a titanium cap. All parts are sealed vacuum with Viton (fluorocarbon rubber) O-rings. More details on the vacuum system and its construction can be found in Appendix B.

3.9 Interaction zone internals

Inserting the frame holding the electric field plates (see Fig. 3.16) into the glass vacuum chamber (see Fig. 3.17) yields what is shown in Fig. 3.18. The further addition to the vacuum chamber of the double cosine coil (see Fig. 3.14) and the titanium endcaps, results in a complete assembly (see Fig. 3.19) ready for installation inside the magnetic shield (see Fig. 3.10).

3.10 Lasers

Here we present a generic outline of the laser systems in the experiment. The lasers are physically located in a different room (Laser Lab) than the magnetic shield (eEDM Lab). An in-depth treatment can be found in an accompanying thesis [96]. The laser

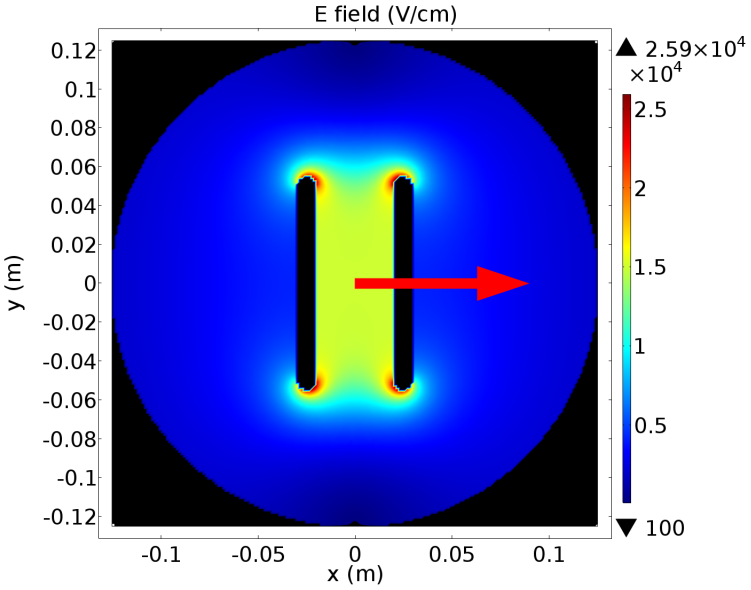

Figure 3.15: Calculation in COMSOL of the electric field between two parallel conductive plates. The red arrow is the electric field direction. The electric field magnitude is represented by a color gradient, from $0\ \mathrm{kV/cm}$ (blue) to $25\ \mathrm{kV/cm}$ (red), for $\pm 20\ \mathrm{kV}$ applied to the field plates.

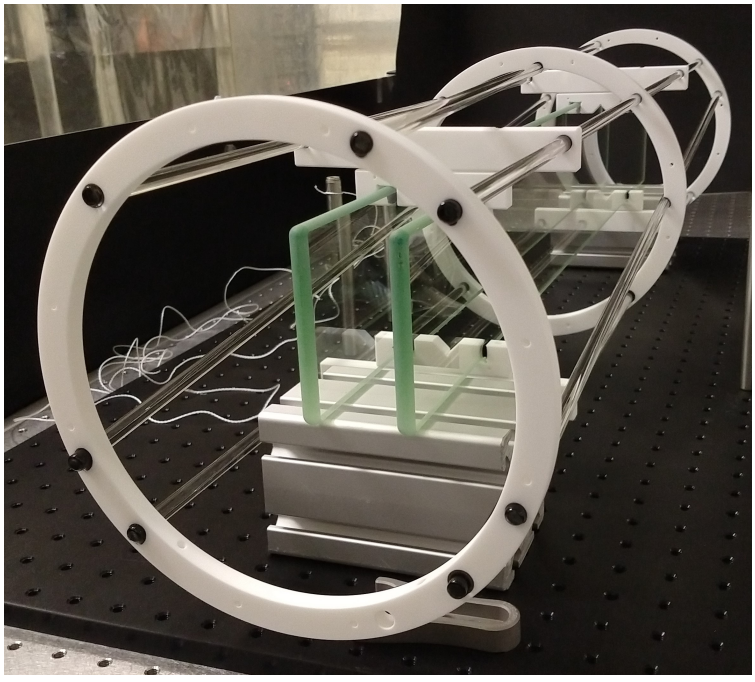

Figure 3.16: Electric field plates in a mounting frame. Specifications and assembly process are given in Appendix D.

Figure 3.17: Glass and titanium vacuum chamber.

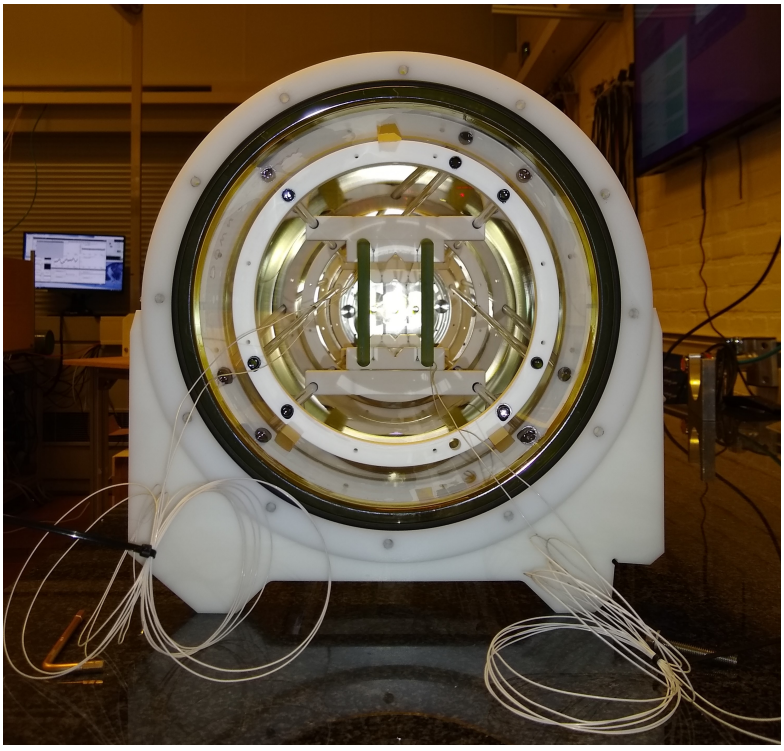

Figure 3.18: Electric field plates in vacuum chamber. Two pairs of cables, each pair connected to a field plate, connect to a high voltage power supply. Two cables are employed for each plate, where each cable makes contact with a different location on the plate surface. This is for ensuring and measuring electrical contact.

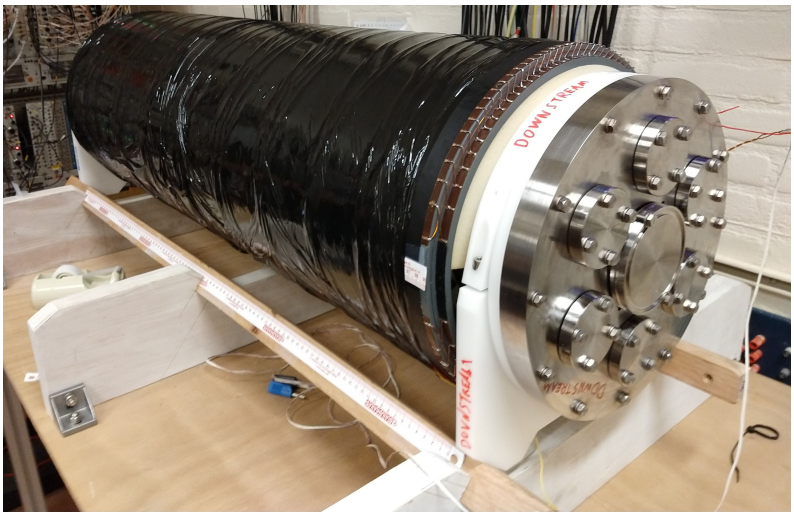

Figure 3.19: Interaction zone internals rest upon a stable insertion frame. Electric field plates are on a frame inside the glass vacuum tube. The double cosine coil is on the outside of the glass vacuum tube. This all rests upon a frame with which it can be inserted into the magnetic shield.

system has parts in the Laser Lab and parts in the eEDM Lab. The light in the Laser Lab is brought by optical fibers to the adjacent eEDM Lab.

Lasers are used for several purposes. A pulse Nd:YAG laser is used to create a Ba atom ablation plume in the source. Various laser systems are used for optical pumping to transfer molecules to a preferred state. We employ Titanium Sapphire (TiSa) lasers, which are highly flexible frequency tunable lasers, and a number of diode lasers. At section B and D (see Section 3.1), lasers are used to drive Light Induced Fluorescence (LIF) in specific molecular states, the signal of which is collected in Photo Multiplier Tubes (PMTs) (see Section 6.1) [x]. The signal at B is used for normalization after the source, but before the interaction zone. The signal at D is used to detect the molecular state after the interaction zone.

Laser light is used to prepare and analyse the BaF superposition state (see Eq. 2.2). The laser light pulses driving this two-photon transition generated with Acousto-Optical Modulators (AOMs) and rf electronics in a manner shown in Fig. 3.20. It starts with a single (tapered amplifier) laser in the Laser Lab. The majority is split by BS1 (Beam Splitter 1) in two beams propagating to AOM1 and AOM2. The frequency difference of the rf signals sent to the AOMs is the hyperfine structure splitting between the levels $|F = 0\rangle$ and $|F = 1\rangle$ (see Fig. 2.3). The AOM frequencies are generated by waveform generators (RIGOL DG 4202 and RIGOL DG 4162), which are stabilized with a 10 Mhz signal from a Rb-clock. The waveform generators also generate the pulse structure (see Fig. 5.1 and Fig. 2.4), specifically the pulse length t and pulse separation T which define the experiment. Light from each AOM is brought by a separate fiber to the eEDM Lab. There the light is brought together in PBS1 (Polar-

[x] The photon signal does not yet saturate the PMTs. Once this is the case the plan is to shift to APDs (Avalanche Photo Diodes) for light collection.

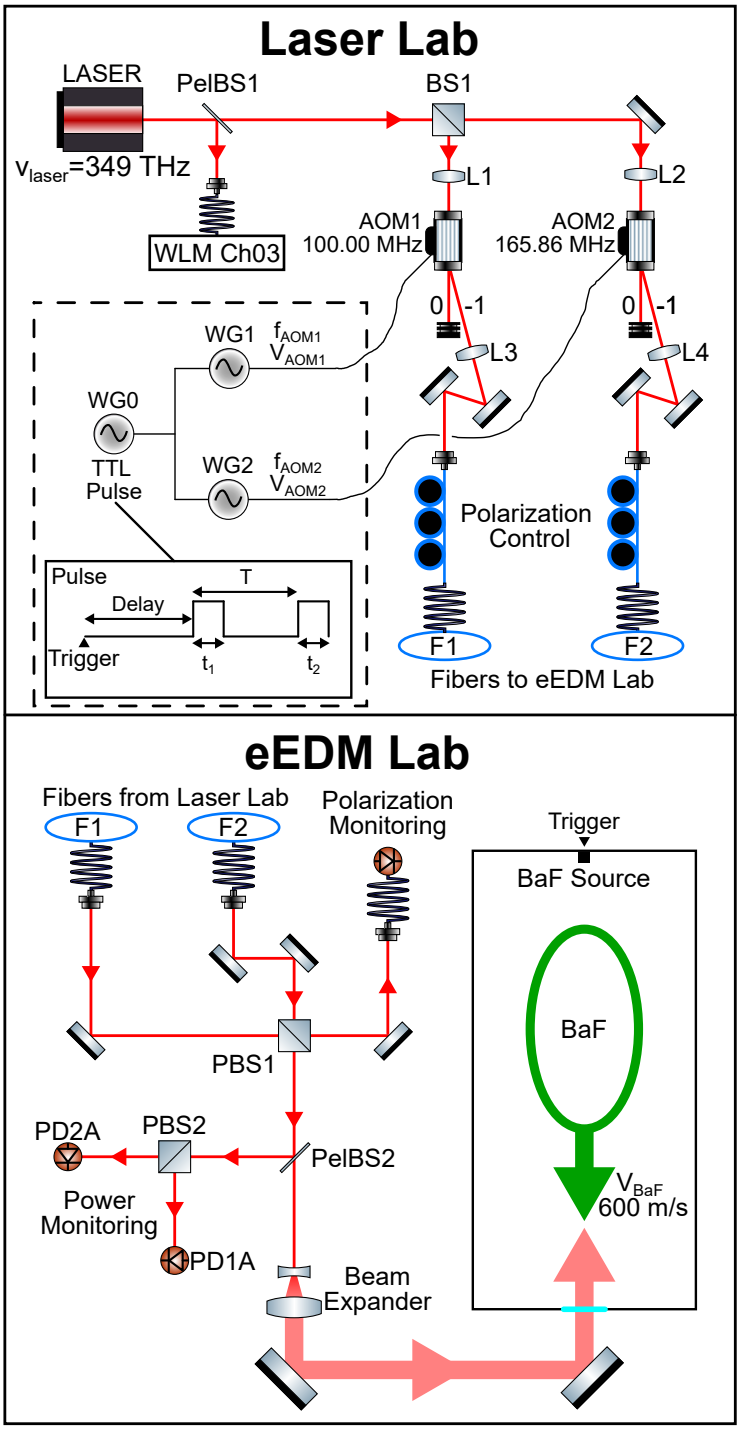

Figure 3.20: Optical and laser light schematic of setup for driving the two-photon transition in BaF (see Fig. 5.1).

izing Beam Splitter 1). Some light is split off for monitoring polarization and power. After passing through a beam expander widening the beam to a few cm diameter and an aperture of 2 cm diameter, the light is brought into the experiment at section D (see Fig. 3.1) counter-propagating to the BaF molecular beam. Pulse timing with respect to the trigger signal and BaF molecular beam velocity determine the location of interaction.

3.11 Data Acquisition

Here we present a generic outline of the Data Acquisition (DAQ) system. An in-depth treatment can be found in an accompanying thesis [112]. The DAQ system can be divided in three layers. The layer closest to the experiment is a hardware preprocessing layer, implemented using various NIM modules. The output signal from the NIM modules is transferred to modules for counting and bit patterns on VME crates. The VME crates and other data sources such as wavelength meters and function generators form the middle layer. Device from this layer send signals to the DAQ pc, which is in the remote layer. It combines the data streams on a back-end computer in a custom built DAQ (Barry and Caddie) [112–114]. The DAQ pc records the signals, and affords remote control of the experimental configuration and live plotting of the recorded data. The DAQ records data after each trigger signal (see Fig. 3.20). It therefore adjusts to the trigger rate, which is typically $10\ \mathrm{s}^{-1}$.

NIM electronic modules are used for signal preprocessing in hardware so that the signal can be recorded. A custom NIM box supplies power to flux gates, and transfers the flux gate signal to a Voltage to Frequency Converter (VFC). The VFC operates at frequencies from 0 to 200 kHz, with at 0 V a frequency offset of about 100 kHz. Before the VFC is an amplifier, which can set the voltage gain to between 1x and 1000x. With 1x gain, the VFC operates at 10 kHz/V [xi]. Readout of all the Light Induced Fluorescence (LIF) signals at section B and D (see Fig. 3.1), including background, is performed with various NIM modules. The photon signals collected at section B are processed into a signal and a background channel. The photon signal collected at section D are processed into one background channel, and a 14 channel Time Of Flight (TOF) signal. The 14 channel TOF has been operated at a time per channel of $51.2\ \mu\mathrm{s}$. In this case the whole TOF spans $716.8\ \mu\mathrm{s}$. If necessary, the time per channel can be set to about $1\ \mu\mathrm{s}$.

The signals from NIM modules are transmitted to SIS3820 scalar counters in VME crates. VME crates and a wavelength meter are attached through an isolated LAN (Local Area Network) to the DAQ pc. Each frontend data source runs a Caddie client which sends data via a network to the DAQ computer upon receiving a trigger signal, where Barry software combines these data streams. The trigger signal is Rb-clock based (see Section 3.1), and is also sent to the source and laser control.

Barry software records the data on disk in raw .eve files, as well as calibrated .root tree files. These files are backed up to a NAS (Network Attached Storage). The DAQ pc monitors which parts of the DAQ systems are active or inactive. Scripts on the DAQ pc are used for live plotting and monitoring of the experiment. The DAQ pc also contains programs that change the configuration of the experiment. It does this by

[xi] So 1000x gain corresponds to 10 kHz/mV.

Figure 3.21: Implemented eEDM experiment setup, which is drawn in Fig. 3.1. BaF molecules move from the source on the right through the interaction zone to the detection zone on the left.

setting a bit pattern in a VME module. For example, this bitpattern is used to set the polarity of electric field using a custom switchbox (see Section 3.7 and Appendix E).

3.12 Conclusion

Searching for an eEDM requires a dedicated effort in the design and implementation of magnetic and electric fields. The completion of the full experiment (see Fig. 3.21) needs a physical description of the measurement procedure [91], the design and implementation of optical means and laser systems [96] and a DAQ systems designed to collect the relevant data [112]. The latter three parts are each the topic of an accompanying thesis. Together they form the new NL-eEDM experimental setup.

4 Generate Homogeneous nT Magnetic Fields in a 70 µT Environment

A stable magnetic holding field of $\mathcal{O}(\mathrm{nT})$ is required in the fiducial volume of the experiment for an EDM sensitive search. The magnetic shield facilitates the suppression of the external field strength by orders of magnitude. However, the environmental field impacts the field in the fiducial volume of the experiment. Three factors affect the magnetic field in the laboratory, the environment of the magnetic shield. First, the Earth magnetic field interacting with magnetic material in the building, forms a magnetic background field of about $70\ \mu\mathrm{T}$ in the laboratory. Magnetic material in the building concerns, e.g. iron reinforced concrete in the laboratory floor. Second, the laboratory is in the neighborhood of varying magnetic fields, e.g. a cyclotron (within 50 m) which operates at varying magnetic fields up to $5\ \mathrm{T}$. Third is the movement of magnetic material, e.g. on the corridor next to the laboratory.

The magnetic field is probed with flux gate sensors. The field is first measured and monitored in an empty lab. After the magnetic shield is installed, field maps of it are generated. The magnetic field of the double cosine coil inside the magnetic shield is mapped.

4.1 Magnetic field probing using flux gates

The FLC3-70 device [115] is a magnetic field probe equipped with 3 flux gates, each capable of probing the magnetic field to better than 1 nT sensitivity in 1 s integration time, each respectively sensitive to the fields B_x, B_y and B_z in the probe coordinate system (see Fig. 4.1). Power supply and sensor output readout of the probes is performed by a custom NIM crate box through a LAN cable (more details in Appendix G). Custom NIM modules with Voltage to Frequency Converters (VFC) digitize the sensor output voltages. The digitized signal is stored using VME based scaler counters (see Section 3.11). These probes, 8 of which have been used in parallel, are continuously monitoring the laboratory magnetic field.

A measurement of the magnetic field over time was performed inside the laboratory (see Fig. 4.2). During the measurements constant monitoring of the environmental magnetic fields is indispensable in order to enable clean data analysis. One systematic effect, of temperature sensitive electronics in combination with temperature variations larger than $10\ ^{\circ}\mathrm{C}$, resulted in $\mathcal{O}(\mu\mathrm{T})$ variations of the measured field.

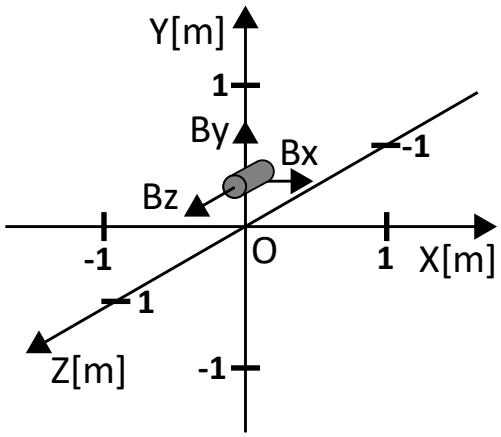

Figure 4.1: Measurements of magnetic field $\vec{B} = (B_x, B_y, B_z)$ are performed on points along the three axes, up to the indicated points 1 meter from origin O, to determine the magnetic field with active compensation coils. Origin O lies at the center of 3 sets of 2 compensation coils (see Fig. 3.3).

Table 4.1: Currents I_{X}, I_{Y}, and I_{Z} flowing through the external compensation coils (see Fig. 3.3), each respectively compensating magnetic field components B_{X}, B_{Y}, and B_{Z}.

I_{X}	I_{Y}	I_{Z}
1558 mA	4097 mA	2656 mA

For example, the higher temperatures in April 2020 [116] resulted in an $\mathcal{O}(\mu\mathrm{T})$ total field change between day 20 and 30. After this we implemented climate control with a temperature stability better than $1\ ^{\circ}\mathrm{C}$. We also adjusted the electronics which further improved the stability. For details on implementation, and the characterization of the resulting stability with the Allan variance [117], see Appendix G.

During magnetic field measurements, a flux gate offset is (self-)calibrated by rotating it (by 180 degrees) into the opposite direction, and taking the difference of the measured values. This difference cancels the magnetic field and yields twice the flux gate offsets. See for example Fig. 4.6, where different flux gates probing the same field (at a 90° phase) measure different amplitudes (amp).

4.2 Environmental impact on magnetic field

The environmental effect of the magnetic field on the experiment demands a measurement of the laboratory magnetic field. A long term measurement was performed with the magnetic field probe at origin O (see Fig. 4.1). A subsequent measurement entails a spatial field map around this origin O. These measurements were performed after compensating the laboratory magnetic field by coils (see Fig. 3.3), operating at currents in Table 4.1.

We performed a long term magnetic field measurement, since we are interested in

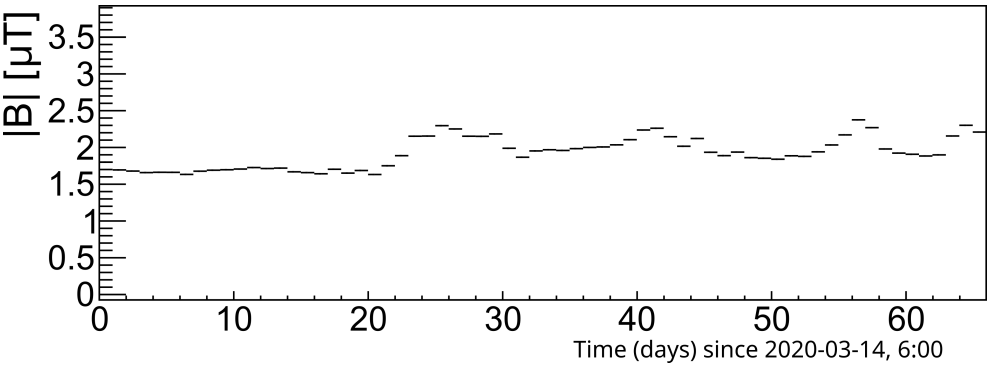

Figure 4.2: Measurement of the laboratory magnetic field over a period of 66 days.

the magnetic field variation in time. A flux gate probe is positioned at the center of the location where the magnetic shield will be after installation, to within a few cm. Over a timescale of more than 2 months, the magnetic field magnitude $|B|$ varies by less than $1\ \mu\mathrm{T}$ at the place of the magnetic shield (see Fig. 4.2).

The field map (see Fig. 4.3) of the laboratory with magnetic field gradients along the X, Y and Z axes (see Fig. 4.1), measured the inhomogeneity of the laboratory field over the volume of the magnetic shield. The magnetic shield (see Section 3.4) would be entirely located in a stable and controlled environmental field of less than $10\ \mu\mathrm{T}$, except for $B_Z(Z = -1\,\mathrm{m})$ where the field exceeded $10\ \mu\mathrm{T}$. This field had been caused by a magnet of a vacuum gauge, which has been replaced by a non-magnetic Bayard-Alpert vacuum gauge before the installation of the magnetic shield. Measurements thereafter show lower fields.

4.3 Field map inside the magnetic shield

After installing (see Appendix F) and degaussing the magnetic shield, a flux gate was used to map the magnetic field inside as a first investigation of its shielding properties (see Appendix H). This forms a reference point for the magnetic field, so that in case some magnetized material ends up inside the shield, it can be noticed. The entire volume inside the inner magnetic shield layer has been mapped for this purpose. If the purpose is improved compensation and homogenization of magnetic fields inside the experimental fiducial volume, the magnetic field can be evaluated in greater detail with this method.

A measurement of the magnetic field was performed by moving and rotating a flux gate stepwise (see Fig. 4.4). Along the z-axis, it was positioned at five locations. For each location the device was rotated to the 16 different angles shown in Fig. 4.4. The flux gate is either rotated around its own axis along the z-axis (FG In state, red dot), or the flux gate is extended (FG Out state, red circle) such that it moves in a circle. The FG In and FG Out state are illustrated by Fig. 4.5. This procedure yields the magnetic field maps presented in Appendix H. An example of the resulting maps (see Fig. H.7 and Fig. H.8) is shown in Fig. 4.6.

The measured maps in Fig. H.7 and Fig. H.8 are summarized in Table 4.2 and Table 4.3. Offset values measured at z = 0 cm (see Fig. H.7 and Fig. H.8) are subtracted

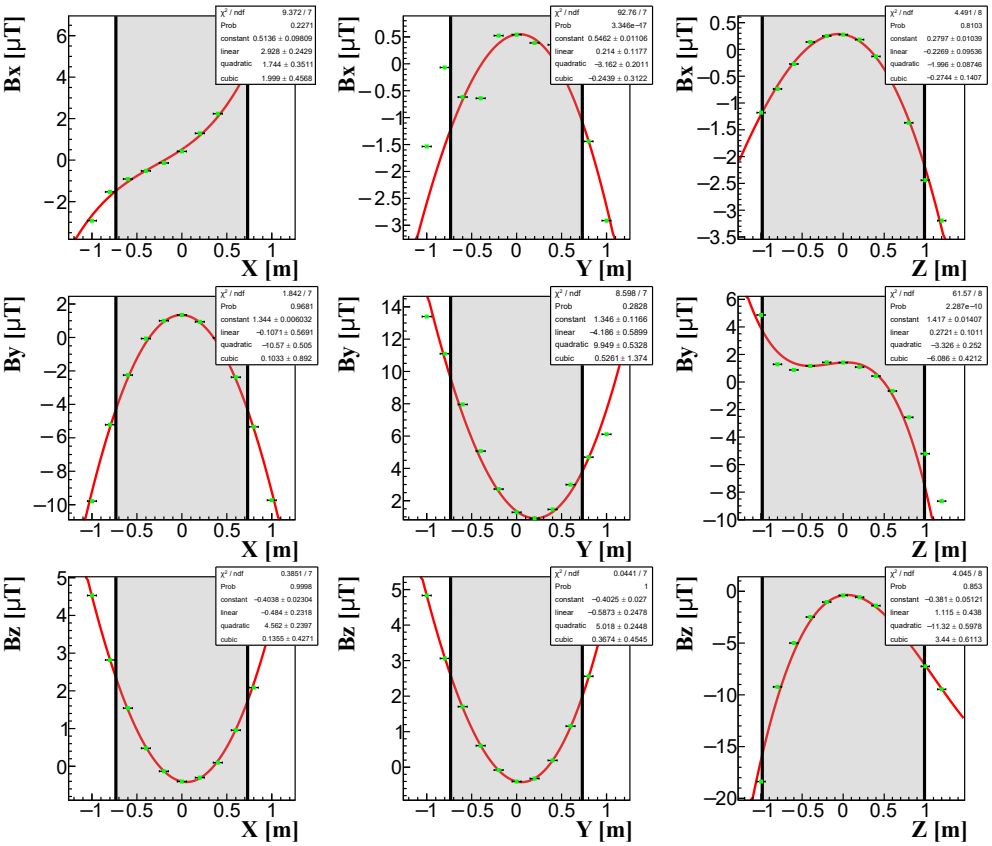

Figure 4.3: Measurement of the laboratory magnetic field, probing the fields along the axes as in Fig. 4.1. The grey areas delimited by lines show the extent of the magnetic shield.

from all measurements [i], since these indicate drift of the flux gate and its electronics. Besides, magnetic field offsets are accounted for by the application of a magnetic holding field (see Section 4.4).

The FG In state (see Fig. H.7) is used to determine field values B at some location z along the z-axis in Table 4.2. Taking differences of field values B for different z locations along the z axis yields the linear field gradients $\Delta B/\Delta z$ in Table 4.3. The field values of B_z in the diagrams (see Fig. H.7) are directly translated into values for $B_z(z)$ listed in the table, with an offset $B_z(z = 0\,\mathrm{cm})$ subtracted

$$B_z(z) - B_z(z = 0\,\mathrm{cm}). \tag{4.1}$$

Since both $B_x(z)$ and $B_y(z)$ measured by the flux gate probe the same field components, merely offset by a 90 degree phase, the amplitudes of both ($|B_x(z)|$ and $|B_y(z)|$)

[i] This is equivalent to putting the magnetic field offset value $\vec{B}_{\mathrm{offset}}$ introduced by the flux gate and its electronics, for each channel to 0, i.e. $\vec{B}_{\mathrm{offset}} = \vec{0}\,\mathrm{nT}$.

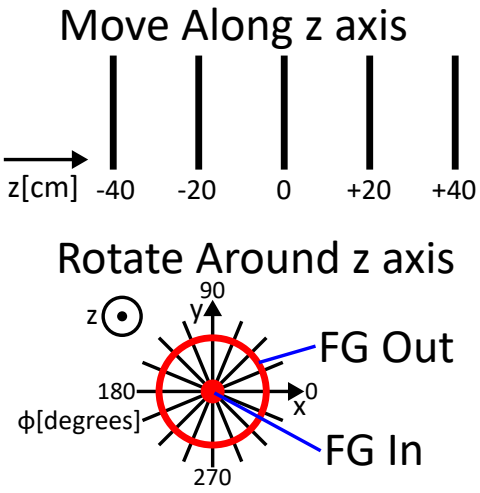

Figure 4.4: Flux gate locations and rotations used in mapping the magnetic field.

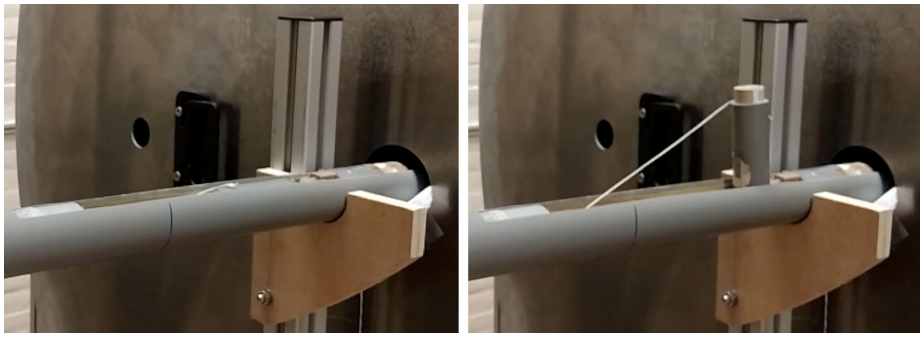

Figure 4.5: Magnetic field mapper with flux gate, usually positioned so that the flux gate is inside the shield as in Fig. 4.4. In one case the flux gate is in the FG In state (left). In the other it is in the FG Out state (right).

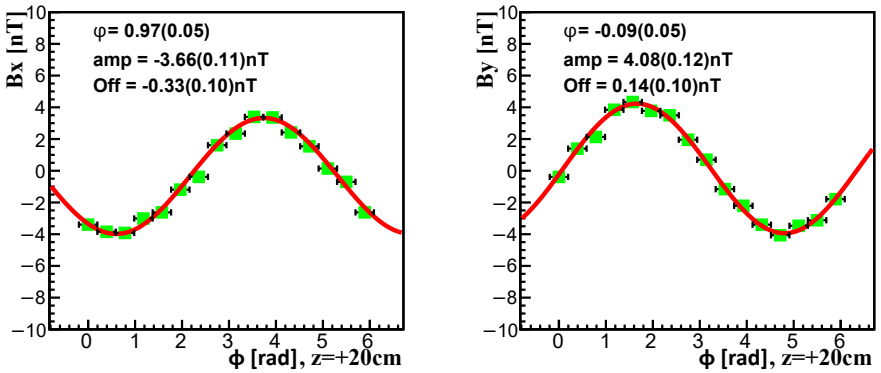

Figure 4.6: Example images from magnetic field mapping procedure Fig. H.7, which together with the values given in Fig. H.8 was used to determine the magnetic fields in Table 4.2 and Table 4.3. A sinusoidal function is fitted (red line) to the data, which has a phase ”φ”, an amplitude ”amp”, and a vertical offset from 0 nT ”Off”.

Table 4.2: Estimates on magnetic field values parallel (B_z) and transverse (B_r) to the z-axis. Shown are field values at the 5 locations, and the linear gradients of the field values with respect to the radial direction ($\Delta B/\Delta r$). The B_z field values are with respect to the offset field value $B_z(z = 0\ \mathrm{cm})$.

z [cm]	-40	-20	0	20	40
Field value B					
$B_r(z)$ [nT]	3.21(8)	3.37(8)	2.57(7)	3.87(8)	4.35(8)
$B_z(z)$ [nT]	$-8.74(5)$	$-4.85(5)$	0.00(5)	2.89(5)	2.65(5)
Linear field gradient $\Delta B/\Delta r$					
$\Delta B_r/\Delta r(z)$ [nT/10cm]	$< 3(1)$	$< 3(1)$	$< 3(1)$	$< 4(1)$	$< 5(1)$
$\Delta B_z/\Delta r(z)$ [nT/10cm]	1.61(9)	0.25(8)	1.72(8)	1.43(8)	0.31(7)

Table 4.3: Summary table of linear gradients along the z direction of field values transverse ($\Delta B_r/\Delta z$) and parallel ($\Delta B_z/\Delta z$) to the z-axis.

z [cm]	-40 to -20	-20 to 0	0 to 20	20 to 40
Linear field gradient $\Delta B/\Delta z$				
$\Delta B_r/\Delta z(z, z + 20\ \mathrm{cm})$ [nT/10cm]	0.08(5)	$-0.40(5)$	0.65(5)	0.24(6)
$\Delta B_z/\Delta z(z, z + 20\ \mathrm{cm})$ [nT/10cm]	1.95(3)	2.43(4)	1.45(4)	$-0.12(4)$

are combined into an average radial field value

$$B_r(z) = \frac{|B_x(z)|+|B_y(z)|}{2}. \tag{4.2}$$

From $B_z(z)$ and $B_r(z)$, their linear gradients along the z-axis $\Delta B/\Delta z$ are arrived at by taking respectively

$$\frac{\Delta B_z}{\Delta z}(z, z + \Delta z) = \frac{B_z(z + \Delta z) - B_z(z)}{\Delta z} \tag{4.3}$$

and

$$\frac{\Delta B_r}{\Delta z}(z, z + \Delta z) = \frac{B_r(z + \Delta z) - B_r(z)}{\Delta z}. \tag{4.4}$$

The FG Out state (see Fig. H.8) is used to determine linear field gradients in the radial direction $\Delta B/\Delta r$ at some location z along the z-axis in Table 4.2. In the FG Out state, the field amplitude of the flux gate y channel $|B_y(z)|$ corresponds to a laboratory magnetic field parallel to the z-axis at radius $R_y = 9.5\ \mathrm{cm}$ from the rotation axis for some location z. A linear gradient in the radial direction of the field component parallel to the z-axis $\Delta B_z/\Delta r$ is arrived at by taking

$$\frac{\Delta B_z}{\Delta r}(z) = \frac{|B_y(z)|}{R_y}. \tag{4.5}$$

The linear gradient transverse to the z-axis of the field transverse to the z-axis $\Delta B_r/\Delta r$ is estimated by studying all channels $B_x(z)$ and $B_z(z)$ (respectively at a radius $R_x =$

$5.5\ \mathrm{cm}$ and $R_z = 7.5\ \mathrm{cm}$ from the rotation axis) for some location z, and estimating the gradients for each channel and angle ϕ

$$\frac{\Delta B(\phi, z)}{2r} = \frac{B(\phi, z) + B(\phi + 180^o, z)}{2r}. \tag{4.6}$$

Here the addition $B(\phi, z) + B(\phi + 180^o, z)$ for values of opposite flux gate directions corresponds to a subtraction of flux gate offsets, leaving only a magnetic field difference. Since field component gradients are smaller than the maximum magnetic field component gradient

$$\frac{\Delta B_r}{\Delta r}(z) < \left(\frac{\Delta B(\phi, z)}{2r}\right)_{max}, \tag{4.7}$$

we tabulate this maximum magnetic field component gradient found for each location z, using Eq. 4.6 for channels $B_x(z)$ and $B_z(z)$.

4.4 Holding field generation inside the magnetic shield

The double cosine coil generates our magnetic holding field $\vec{B}_{DCC} = |B_{DCC}|\hat{B}_{DCC} = |B_{DCC}|\hat{x}$ (see Section 3.5.1). The generated magnetic field at the center of the coil was first determined outside the magnetic shield. It is

$$|B_{DCC}| = \frac{\Delta|B_{DCC}|}{\Delta I_{DCC}} I_{DCC} = 5(1)\frac{\mathrm{nT}}{\mathrm{mA}} \times I_{DCC}, \tag{4.8}$$

with I_{DCC} the current flowing through the double cosine coil in mA. The generated magnetic field inside the magnetic shield was determined by positioning the flux gates at different locations on axis. The flux gate was positioned as FG In shown in Fig. 4.5. Switching the current polarity switches the magnetic field direction. The field at the center of the coil was measured to be

$$|B_{DCC}| = \frac{\Delta|B_{DCC}|}{\Delta I_{DCC}} I_{DCC} = 3.0(1)\frac{\mathrm{nT}}{\mathrm{mA}} \times I_{DCC}. \tag{4.9}$$

Less than 1 % hysteresis is observed at $1\ \mathrm{nT}$ resolution when switching between $60\ \mathrm{nT}$ and $-60\ \mathrm{nT}$. The difference in field, for $B_{DCC} = \pm 60\ \mathrm{nT}$ generated by the coil inside the magnetic shield, between $z = 0\ \mathrm{cm}$ and $z = \pm 25\ \mathrm{cm}$, lies at $B(|z| = 0\ \mathrm{cm}) - B(|z| = 25\ \mathrm{cm}) < 1\ \mathrm{nT}$, i.e. $\Delta B_{DCC}/B_{DCC} < 1\ \mathrm{nT}/60\ \mathrm{nT} \simeq 1.7\ \%$. That the interaction with magnetic material reduces the generated field inside (see Eq. 4.9) compared to outside the shield (see Eq. 4.8), agrees with COMSOL calculations comparing the double cosine coil inside and outside a magnetic shield (see Section 3.5.1). Spin precession measurements employing molecules (see Fig. 6.8) confirm the generated magnetic field. The spin precession measurement yields a lower field value, since it probes 60 cm in the coil, rather than only value at the center of the coil as shown in Eq. 4.9.

In addition to the double cosine coil there is a coil capable of generating a magnetic field component (see Section 3.5.2)

$$B_y = \frac{\Delta B_y}{\Delta I_y} I_y = 3(1)\frac{\mathrm{nT}}{\mathrm{mA}} \times I_y, \tag{4.10}$$

for a current I_y in mA. It serves diagnostic purposes in the EDM measurements.

4.5 Conclusion

We determined the laboratory magnetic field, the magnetic field inside the magnetic shield, and the magnetic holding field generated by the double cosine coil with flux gates. The laboratory magnetic field is continuously monitored with the developed flux gate infrastructure.

A long term measurement shows a variation of the environmental magnetic field magnitude of less than $1\ \mu\mathrm{T}$ over a period of more than 2 months. The field map indicates that the magnetic shield is located in residual environmental magnetic fields less than $10\ \mu\mathrm{T}$. From continuous monitoring in the eEDM laboratory, potential sources can be related to changes in the magnetic field. The AGOR cyclotron within 50 meters operating at up to $5\ \mathrm{T}$, affects the environmental magnetic field by less than $50\ \mathrm{nT}$, which is the resolution of the employed flux gates. The door to the eEDM laboratory causes magnetic field spikes of $100\ \mathrm{nT}$ in section D (see Fig. 3.1) outside the μ-metal magnetic shield.

Inside the magnetic shield the magnetic field is $< 10\ \mathrm{nT}$ over 80 cm distance along the z axis, where the 80 cm distance includes the designed fiducial volume of 50 cm length and 4 cm diameter. The linear gradients in the radial direction ($\Delta B/\Delta r$) are $< 5(1)\ \mathrm{nT}/10\ \mathrm{cm}$. A maximum beam diameter of 4 cm corresponds a maximum field difference $< 2.0(4)\ \mathrm{nT}$. The linear gradients along z ($\Delta B/\Delta z$) are dominated by the gradient $\Delta B_z/\Delta z$, with in particular the largest gradient $\Delta B_z/\Delta z(z = -20\ \mathrm{cm}, z = 0\ \mathrm{cm}) = 2.43(4)\ \mathrm{nT}/10\ \mathrm{cm}$. The double cosine coil generates a stable and homogeneous holding field (see Section 4.4).

For the EDM experiment it is of crucial importance that the environmental magnetic field is controlled to the $10\ \mu\mathrm{T}$ level. The measurements require a holding field of $\mathcal{O}(\mathrm{nT})$ for which a double cosine coil has been designed and built with better than 1.7 % inhomogeneity over the designed fiducial volume. In our measurements we could exploit a fiducial volume of up to 130 cm length (see Fig. 6.9). Here we conclude the building of the magnetic field based apparatus, which concerns design and implementation (see Chapter 3), and which concerns the evaluation of its magnetic properties using flux gates.

5 Electric and Magnetic Field Maps with a BaF Beam - One pulse laser spectroscopy

We embed the developed interaction zone within the newly built setup. Combined with the BaF beam source [99], laser systems [96], DAQ systems [112], and interpretation [91] this yields a complete experiment. The homogeneous electric and magnetic fields for an EDM experiment need to be determined at runtime of the experiment. Here we exploit the electric and magnetic field sensitivity of transitions in the BaF molecule [90]. This permits probing the region the molecules pass, the same as during an EDM search measurement. Stark shifts are of $\mathcal{O}(200\ \mathrm{MHz}/(\mathrm{kV}/\mathrm{cm}))$ on electronic transitions. Tensor Stark shifts are of $\mathcal{O}(10\ \mathrm{kHz}/(\mathrm{kV}/\mathrm{cm}))$ on the hyperfine transitions. Zeeman shifts are of $\mathcal{O}(10\ \mathrm{Hz}/\mathrm{nT})$ on hyperfine sublevels. We measure the electric field and field distribution to V/cm level, which requires a measurement of the tensor Stark shift to $\mathcal{O}(10\ \mathrm{Hz})$. We measure the magnetic field and magnetic field distribution to $100\ \mathrm{pT}$ level, which requires a measurement of the Zeeman shift to $\mathcal{O}(10\ \mathrm{Hz})$. A BaF beam thus employed yields information on the electric and magnetic fields.

5.1 Experimental method

The experiment uses a two-photon transition in order to produce the molecular state that precesses in the interaction zone. Two laser light fields with linear and orthogonal polarizations operating at frequencies $\omega_S/2\pi$ and $\omega_P/2\pi$ drive this transition (see Fig. 5.1). Their generation is described in Fig. 3.20. They are counter-propagating to the BaF beam. At frequency difference

$$\omega_{PS}/2\pi = (\omega_P - \omega_S)/2\pi \tag{5.1}$$

the typical detuning from the $X^2\Sigma^+ - A^2\Pi_{1/2}$ resonance is $\Delta \approx 1\ \mathrm{GHz}$, and two-photon detuning from the $|F=0\rangle$ to $|F=1\rangle$ transition

$$\delta = (\omega_{PS} - \omega_{HFS}(|E|))/2\pi. \tag{5.2}$$

In the experiment δ is of $\mathcal{O}(\mathrm{kHz})$ (see Fig. 2.3). The polarizations $\vec{P}_S$ for laser field $\omega_S/2\pi$ and $\vec{P}_P$ for laser field $\omega_P/2\pi$ are arranged to be linear and orthogonal to each other. The coupling between $|F=0, m_F=0\rangle$ and $|F=1, m_F=0\rangle$ states is selection

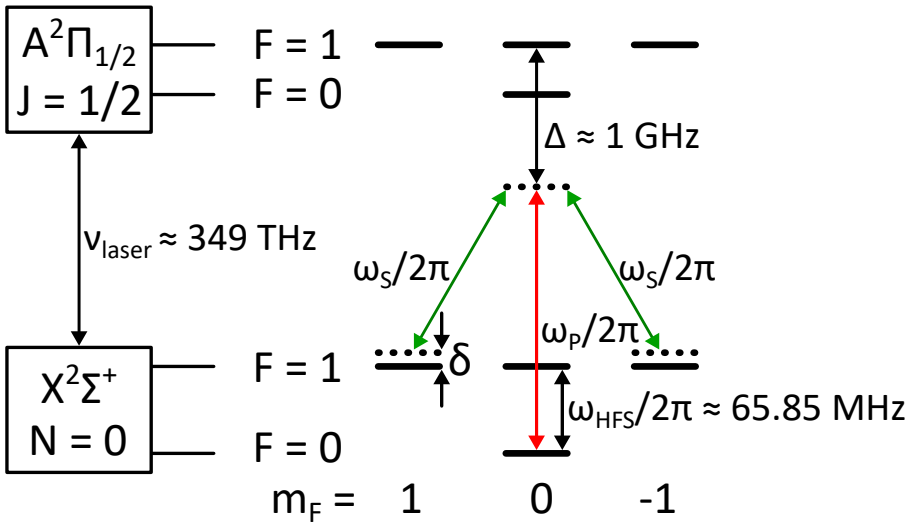

Figure 5.1: Superposition of the $X^2\Sigma^+, |F=1, m_F=1\rangle$ and $|F=1, m_F=-1\rangle$ states is achieved with a two-photon process with detuning Δ from the $X^2\Sigma^+, N=0 - A^2\Pi_{1/2}, J=1/2$ resonance [91, 92]. The experiment operates at $\Delta \gg \omega_{HFS}/2\pi$. The laser light generation is described in Fig. 3.20.

rule suppressed. Such a laser-light pulse creates a molecular superposition state [92]. The two-photon Rabi frequency Ω_{PS} depends on the laser-light pulse intensity, and characterizes the coupling strength between the levels $|F=0\rangle$ and $|F=1\rangle$. If the product of the two-photon Rabi frequency Ω_{PS} and the pulse length t is $\Omega_{PS}t = \pi$, the laser-light pulse fully transfers molecules between the $|F=0, m_F=0\rangle$ state and the superposition of the $X^2\Sigma^+$, $|F=1, m_F=1\rangle$ and $|F=1, m_F=-1\rangle$ states [90–92, 96]. The laser-light pulse is typically operated at intensities of 10 $\mathrm{mW/cm^2}$.

In this chapter specifically we describe a situation with a single pulse of length t (see Fig. 5.2). This method works at low light intensity, i.e. $\Omega_{PS}t \ll \pi/2$ with two-photon Rabi frequency Ω_{PS}, and pulse length t. The forward velocity of the BaF molecular beam and the starting time of the pulse determine the location of the BaF molecules while interacting with the pulse, hence they affect the location of probed fields. The Doppler effect results in a shift [97]

$$\omega_D = 2\pi f_D = \vec{v}\cdot\vec{k} \approx c|k|\left(1+\frac{v_z}{c}\right), \tag{5.3}$$

which is a result of the BaF beam moving at velocity $\vec{v} = v_z\hat{z}$ in the direction opposite to the laser light, which propagates with $\vec{k} = -|k|\hat{z}$ [i]. The spectral width relates to the full width at half maximum [97]

$$FWHM \geqq 1/2\pi t, \tag{5.4}$$

through the pulse length t. This is an equality under the condition that FWHM is limited by the pulse length, e.g. sufficiently small electric and magnetic field gradients in the interaction zone. A deviation from this equality indicates larger field gradients.

[i] With $|k| = 2\pi/\lambda$, and $\vec{k}$ along the Poynting vector.

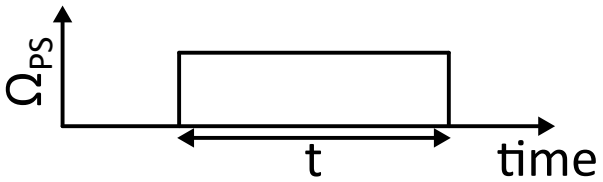

Figure 5.2: One laser-light pulse of length $t \lesssim 1\,\mathrm{ms}$, drives the BaF two-photon transition with the associated Rabi frequency Ω_{PS}.

5.2 Electric field measurements

An electric field measurement in the interaction zone exploits the BaF beam and the tensor Stark shift in the $X^2\Sigma^+$ hyperfine $|F=0\rangle$ to $|F=1\rangle$ transition. An electric field magnitude $|E|$ corresponds to a tensor Stark shift $\omega_{tensor}(|E|)/2\pi$ for the molecular transition (see Fig. 5.3(a)).

The measurements show a difference (see Fig. 5.3(b)) for opposite electric field directions. This is observable through a difference in the observed tensor Stark shift $\omega_{tensor}/2\pi$. The relevance to EDM measurements lies in the crucial dependence on electric field values being the same for both polarities. An eEDM measurement aiming for a resolution $\sigma_d = 10^{-27}\,\mathrm{e\,cm}$ operating at working point $|E| = 10\,\mathrm{kV/cm}$ has an electric field magnitude tolerance $\Delta|E| = 4\times10^{-5}\,\mathrm{kV/cm}$ [91], which corresponds to a relative tolerance of $\Delta|E|/|E| = 4\times10^{-6}$. The difference in electric field magnitudes between measurements

$$\Delta|E| = |E| - |E'| \tag{5.5}$$

correspond to a difference in tensor Stark shift frequencies

$$\Delta\omega_{tensor}(|E|-|E'|)/2\pi = \omega_{tensor}(|E|)/2\pi - \omega_{tensor}(|E'|))/2\pi, \tag{5.6}$$

on condition that other electric field related frequency shifts $\ll \omega_{tensor}/2\pi$.

5.3 Magnetic field measurements

Adding a sufficiently strong magnetic field ($2\mu_B|B|/h \gg FWHM$) causes a separation of the Zeeman levels. We exploit the Zeeman shift for magnetic field measurements in the interaction region. A pulse length of $t \approx 1\,\mathrm{ms}$ yields information on the average magnetic field along the whole interaction zone, since at a molecular velocity $v_z = 600\,\mathrm{m/s}$ it probes the magnetic field in a region of length $l \approx 60\,\mathrm{cm}$. Shorter pulse lengths, at $t \approx 200\,\mu\mathrm{s}$, probe a region of length $l \approx 12\,\mathrm{cm}$. By changing the pulse delay, the shorter pulses have been used to map not only the magnetic field, but also to explicitly determine its change along the beam axis in the interaction zone. We recorded maps for different magnetic field values that were set using the double cosine coil (see Section 3.5.1).

The sufficiently small experimental magnetic fields cause a linear Zeeman splitting of the molecular lines

$$\Delta f_Z = 2\mu_B|B|/h, \tag{5.7}$$

with $\mu_B/h = 14\,\mathrm{Hz/nT}$ [118]. Without an electric field, Δf_Z is used to determine magnetic field magnitude $|B|$. A field typical in the experiment is $|B| = 10\,\mathrm{nT}$. This

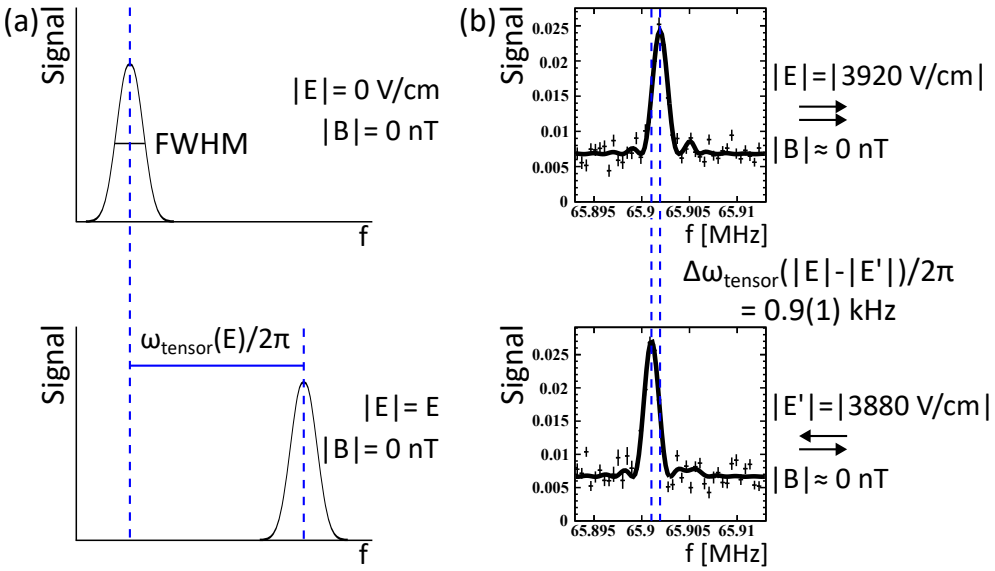

Figure 5.3: (a) The tensor Stark Shift $\omega_{tensor}(E)/2\pi$ is sensitive to the electric field magnitude. The sensitivity to the electric field magnitude of the tensor Stark shift can be exploited to compare different electric field configurations. This includes in particular asymmetries of electric field configurations of opposite polarity. (b) Measurement with electric field configurations $\vec{E} = |E|\hat{x}$ and $\vec{E}' = -|E'|\hat{x}$ (arrows represent their directions), at a working point of about $4\ \mathrm{kV/cm}$. The magnitudes $|E|$ and $|E'|$ show a difference. This difference is observable through a tensor Stark shift difference $\Delta\omega_{tensor}/2\pi = 0.9(1)\ \mathrm{kHz}$, which corresponds to $\Delta|E| = |E|-|E'| \approx 40\ \mathrm{V/cm}$. The pulse length of $t = 500\ \mu\mathrm{s}$ results in a linewidth of $2\ \mathrm{kHz}$. The integration time is 1000 s for both spectra, which corresponds to about 13 seconds per data point. This combination of pulse length and integration time yields a frequency resolution of $\sigma_f \approx 100\ \mathrm{Hz}$, which corresponds to an electric field resolution $\sigma_{|E|} \approx 5\ \mathrm{V/cm}$. It further corresponds to a magnetic field resolution of about $\sigma_{|B|} \approx 4\ \mathrm{nT}$.

corresponds to a Zeeman splitting of $\Delta f_Z = 280\ \mathrm{Hz}$. In an electric field $\vec{E} = |E|\hat{x}$ the tensor Stark shift $\omega_{tensor}/2\pi$ suppresses molecular sensitivity to transverse magnetic field components, which is known from matrix diagonalization [91]. This effect causes an observed splitting

$$\Delta f < \Delta f_Z. \tag{5.8}$$

In the case of a tensor Stark shift $\gg$ Zeeman splitting, the Zeeman splitting is proportional to the magnetic field component $B_\parallel$ parallel to the electric field $\vec{E}$ [90, 91]. One operates in this limit $\omega_{tensor}(|E|)/2\pi \gg \Delta f_Z$ with a sufficiently large electric field $\vec{E} = |E|\hat{x}$. Molecular sensitivity to magnetic field components $B_\perp$ transverse to the electric field becomes negligible, hence splitting is dominated by the Zeeman effect and we have

$$\Delta f_Z = 2\mu_B B_\parallel/h = 2\mu_B B_x/h. \tag{5.9}$$

This only depends on the parallel magnetic field component $B_\parallel = B_x$. With a known absolute magnetic field value $|B|$ and x-component B_x the magnetic field perpendic-

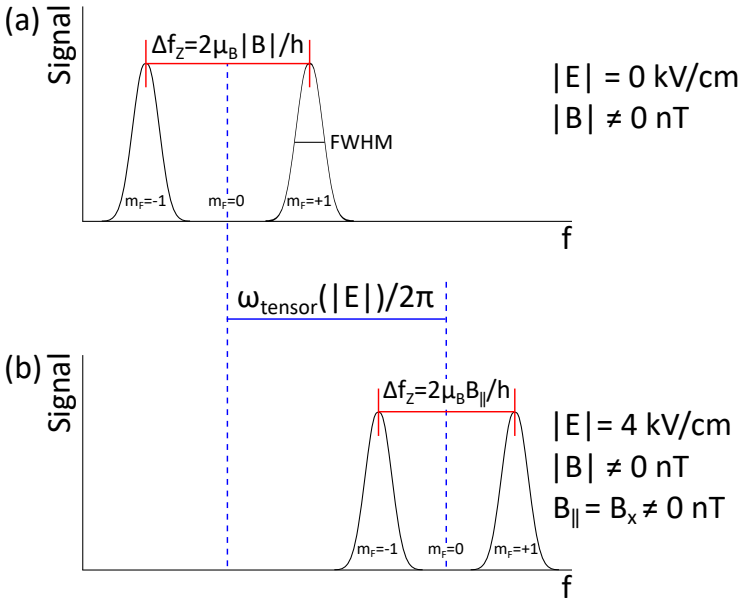

Figure 5.4: In a single pulse two-photon experiment molecular sensitivity to the magnetic field depends upon the electric field. (a) Without electric field one observes Zeeman splitting Δf_Z as a function of $|B|$. (b) An electric field $\vec{E} = |E|\hat{x}$ causes a tensor Stark shift (see Fig. 5.3) and modifies the magnetic field Zeeman splitting. In an electric field molecular sensitivity to all magnetic field components are suppressed except for the one parallel to the electric field. In both cases coupling to the $|F = 1, m_F = 0\rangle$ state is selection rule suppressed by polarization of the two-photon laser light [91, 96].

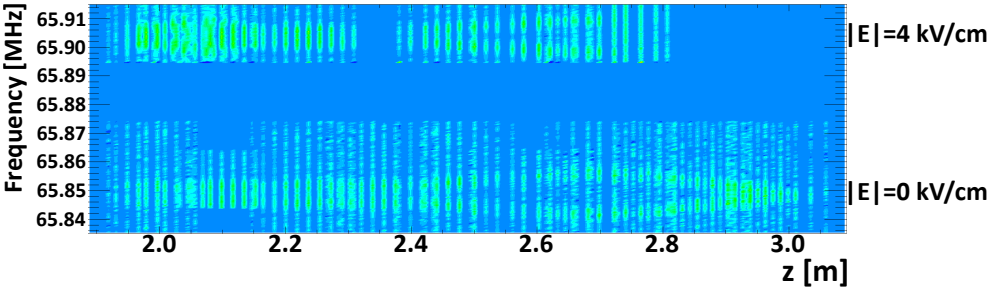

Figure 5.5: Composite figure of multiple spectra for different pulse delay timing and thus position. For electric field magnitude $|E| = 0\,\mathrm{kV/cm}$ and for $|E| = 4\,\mathrm{kV/cm}$. The signal with high electric field is shifted up in frequency, and suppressed molecular sensitivity to magnetic field components transverse to the electric field direction reduces splitting between peaks. Pulse length is $t = 200\,\mu\mathrm{s}$, which corresponds to $5\,\mathrm{kHz}$ wide (FWHM) peaks. Position along the apparatus axis $z = z(v_z, l_{setup}, TOF)$ is a function of molecular beam forward velocity v_z (see Section 2.3.2), path length l_{setup} with respect to the source (see Fig. 3.1), and time of flight TOF with respect to the source. The TOF used to extract the z position has a binning resolution of $51.2\,\mu\mathrm{s}$ on S_D (see Section 3.1). This corresponds to 3 cm position resolution.

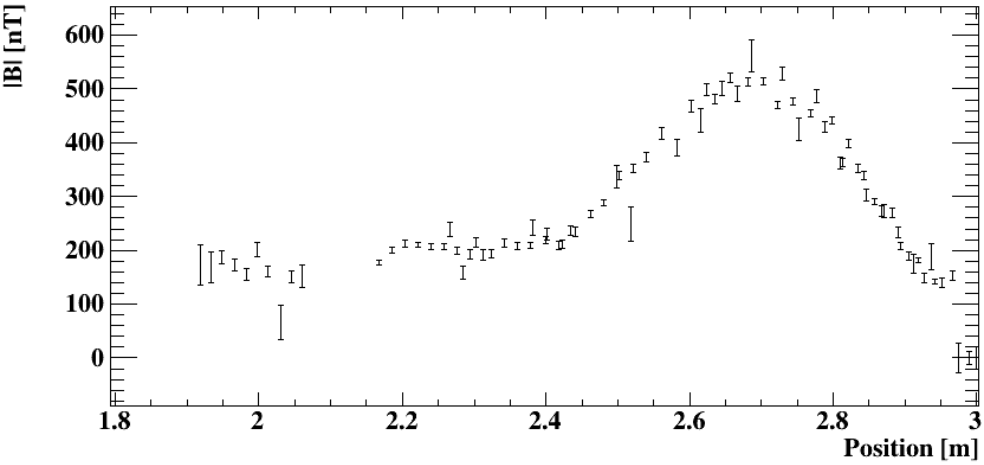

Figure 5.6: Magnetic field map along the center axis of the apparatus for the electric field magnitude $|E| = 0\,\mathrm{kV/cm}$. Based on the measurements compiled in Fig. 5.5. The feature at 2.70 m was due to a magnetic impurity in the setup, which has subsequently been removed.

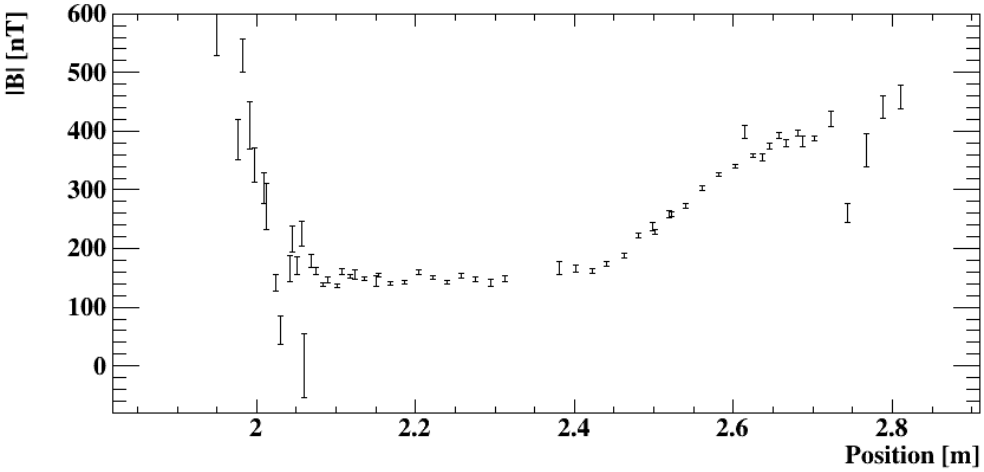

Figure 5.7: Magnetic field map along the center axis of the apparatus for the electric field magnitude $|E| = 4\,\mathrm{kV/cm}$. There is low noise between 2.05 m and 2.70 m. There is rather high noise before 2.05 m and after 2.70 m. The noise originates from the inhomogeneity of the electric field at the edges of the electric field plates (see Fig. 3.15), which causes substantial line broadening. The low noise also indicates that the region with a homogeneous electric field between the plates is some 65 cm long.

ular to the electric field is

$$B_\perp = \sqrt{B_y^2 + B_z^2} \tag{5.10}$$

with

$$B_\perp = \sqrt{2B_x(|B| - B_x)}. \tag{5.11}$$

This situation applies for $B_\parallel \gg B_\perp$.

There is a trade-off between the desired magnetic field magnitude resolution $\sigma_{|B|}$ and the desired (longitudinal) spatial resolution σ_z, that determines the optimal laser light pulse length t. The frequency resolution is given as

$$\sigma_\nu = \frac{FWHM}{S/N}, \tag{5.12}$$

with the full width at half maximum $FWHM$, and the signal to noise ratio S/N. Eq. 5.4 then implies a pulse length t dependence

$$\sigma_\nu(t) = \frac{1}{S/N \times 2\pi t}. \tag{5.13}$$

The frequency resolution corresponds to a magnetic field magnitude resolution

$$\sigma_{|B|}(t) = \frac{1}{S/N \times 2\pi t} \times \frac{h}{2\mu_B|B|}, \text{ where } \frac{2\mu_B|B|}{h} = \frac{28\text{Hz}}{\text{nT}}. \tag{5.14}$$

The (longitudinal) spatial resolution scales as

$$\sigma_z(t) = t \cdot v_z, \tag{5.15}$$

with v_z the forward molecular beam velocity.

A series of measurements at different longitudinal positions, and for two different electric field conditions (see Fig. 5.5), illustrates the principle as drawn in Fig. 5.4. An increase in the electric field magnitude from $|E| = 0$ kV/cm to $|E| = 4$ kV/cm, increases the tensor Stark shift $\omega_{tensor}/2\pi$ to 55 kHz. While both electric field conditions are in the same magnetic field, the splitting due to the Zeeman effect is different. In the eEDM experiment, we have

$$\omega_{tensor}/2\pi \gg \Delta f_Z. \tag{5.16}$$

The tensor Stark shift $\omega_{tensor}/2\pi = \mathcal{O}(100\,\text{kHz})$ is much larger than the Zeeman shift. With the magnetic field in Fig. 5.5 the Zeeman shift is $\Delta f_Z = \mathcal{O}(10\,\text{kHz})$. But Eq. 5.16 holds especially for a typical field of $|B| \approx 10$ nT, where the Zeeman shift is a smaller $\Delta f_Z = \mathcal{O}(100\,\text{Hz})$. The electric field magnitude $|E| = 4$ kV/cm shows less splitting compared to the case with no electric field $|E| = 0$ kV/cm (see Fig. 5.5), because the tensor Stark shift $\omega_{tensor}/2\pi$ suppresses molecular sensitivity to magnetic field components transverse to the electric field.

The difference between field maps taken with flux gates (see Section 4.3) before the interaction zone was installed and the field maps taken with the full setup exploiting the molecules (see Fig. 5.6 and Fig. 5.7), can be explained by a magnetic impurity in the setup. The magnetic impurity was a magnetic wire. After identification and

subsequent removal of this impurity, magnetic fields measured using molecules are consistent with the flux gate maps.

The larger error bars and scatter of data points visible in Fig. 5.7 is related to the electric field distribution around electric field plates. This can be exploited to locate the electric field plates. The low noise region also indicates the length of the homogeneous electric field region.

5.4 Conclusion

The electric and magnetic field sensitivity of some transitions in BaF was exploited by two-photon spectroscopy, summarized in Table 5.1. Besides a determination of the fields, the presented experimental methods can be viewed as a bootstrap procedure to an EDM experiment, due to significant overlap in experimental procedures.

The electric field was determined using the tensor Stark shift of the $|F = 0\rangle$ and $|F = 1\rangle$ hyperfine states. For an averaging time of $T_{ave} = 1000\,\mathrm{s}$, $\sigma_f \approx 100\,\mathrm{Hz}$ frequency resolution was demonstrated, and could be improved with longer averaging times. This corresponds to an electric field resolution of $\sigma_{|E|} \approx 5\,\mathrm{V/cm}$. Similarly the magnetic field was determined with $\sigma_{|B|} \approx 4\,\mathrm{nT}$ resolution. This is sufficient resolution to establish whether a spin precession measurement is a viable next step (see Eq. 6.1).

The magnetic field distribution was determined using the Zeeman splitting between the $|F = 1, m_F = 1\rangle$ and $|F = 1, m_F = -1\rangle$ states. Measurements with different pulse delays probe the magnetic field in different locations. The position resolution of such a measurement is about 3 cm in the current setup. Using our measurement we revealed the presence of a magnetic wire, which could subsequently be identified and removed. In presence of an electric field, transverse and parallel components of the magnetic field can be distinguished.

In addition, the electric field noise was used to locate the electric field plates. The length of the homogeneous electric field region between the plates (see Fig. 5.7) is 65 cm, in agreement with design calculations (see Fig. 3.15). The length of the homogeneous electric field distribution limits the EDM experiment sensitivity for a given molecular velocity.

Table 5.1: Measuring electric and magnetic fields with a BaF beam by two-photon spectroscopy results in the given resolution within $T_{ave} = 1000\,\mathrm{s}$ averaging time. The resolution scales as $1/\sqrt{T_{ave}}$.

Parameter	Observable	Resolution (1000 s averaging)
Frequency	peak position	$100\,\mathrm{Hz}$
Electric field	tensor Stark shift	$5\,\mathrm{V/cm}$
Magnetic field	Zeeman splitting	$4\,\mathrm{nT}$

6 Capabilities of the Experiment for EDM Searches - Two pulse laser spectroscopy

Experiments with two separated pulses (see Fig. 6.1) extend the capabilities of the setup towards a sensitive eEDM search. The derived signal exhibits sensitivity to both the electric and the magnetic field [92]. The extent of homogeneous electric and magnetic fields permit spin precession measurements with a $T = 1\ \mathrm{ms}$ coherent interaction time. Exclusively optical excitation from a collinear laser provides an, in space, time and phase, well defined interaction zone. Employing this the magnetic field inside the magnetic shield is characterized. Measurements of the environmental magnetic field, combined with a limit on the magnetic shield shielding factor obtained using spin precession, demonstrate the stability of the magnetic field inside the magnetic shield. The effect of the electric field on the signal is evaluated. Analysis of EDM experiments concerns probing many parameters that could mimic an EDM. In particular the effect of motional and transverse magnetic fields is estimated [i]. Several other systematic effects are studied.

6.1 Spin precession signal from photon counting

Among the known EDM experiments some have regions for spin precession with a well defined time through an RF pulse [55]. Others have a well defined location through laser beam position [79]. This experiment has both a well defined time and position, with in addition a well defined phase. The experiment depends on a ru-

[i] Fields transverse to the electric field direction.

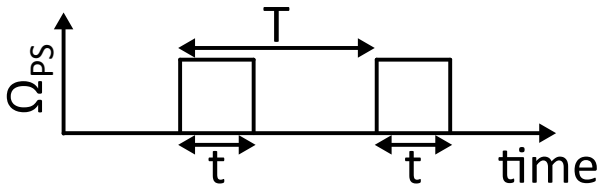

Figure 6.1: Two laser-light pulses of length t drive the BaF two-photon transition (see Fig. 5.1) with the associated Rabi frequency Ω_{PS}, where $\Omega_{PS}t = \pi$ is aimed for. These pulse are separated by a coherent interaction time T. Not to scale.

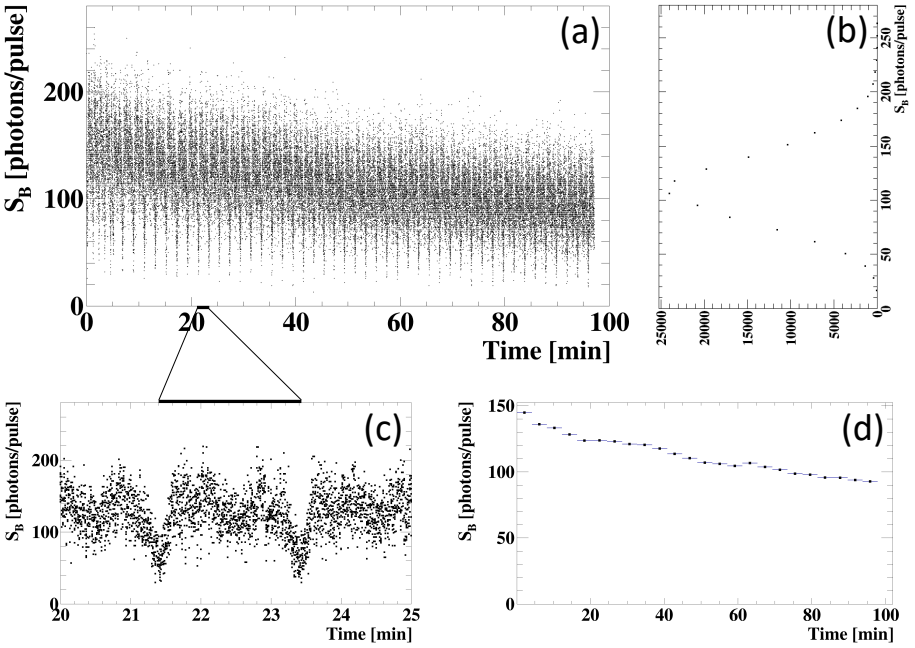

Figure 6.2: (a) Shot to shot fluctuation of the number of molecules N_{mol} is reflected in signal S_B. (b) Projection on axis S_B of the occurrence rate of some number of photons/pulse over the full dataset. (c) On the 1 minute time scale, the rate of BaF from the source varies with the target rotation period. (d) Over the whole measurement, both source BaF yield, and laser frequency in relation to the resonance frequency, cause a drift of the signal. Through the time dependence of the source, signal S_D is correlated with the signal S_B.

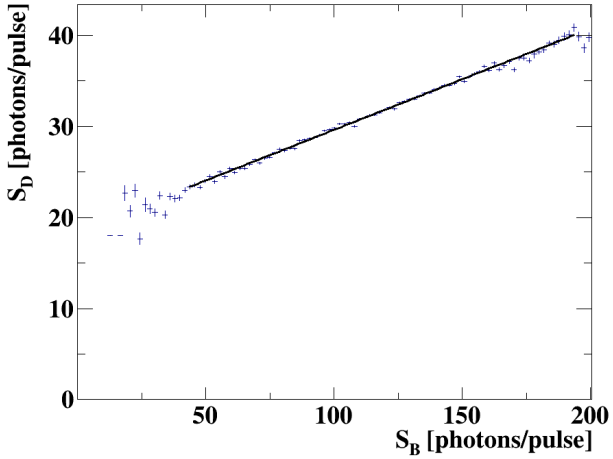

Figure 6.3: This particular measurement yields the parameters $BG_D = 18.51(5)$ photons/pulse and $\epsilon_{D/B} = 0.1112(5)$ for Eq. 6.7. This demonstrates that within 100 minutes the calibration parameters can be determined to better than 1%.

bidium clock frequency stabilized function generators controlling 2 Acousto-Optic Modulators (AOMs). Laser light pulses, collinear but counter-propagating to the BaF beam, determine the spin precession region. Well defined interaction time is due to high resolution optical pulse timing. Well defined position is achieved by stable pulse timing [ii]. The phase is well defined through recombining 2 laser light pulses which were previously split off from a single laser light beam. The frequency difference of the 2 AOMs provides two laser light fields that cause the two-photon transition (see Fig. 3.20).

A spin precession measurement requires sufficiently small magnetic fields and field gradients. The condition for this is that between two extreme opposite classes of molecules, e.g. slowest and fastest, the phase evolution difference is at most

$$\Delta\phi_{max} = \frac{\mu_B \Delta|B|_{max} T}{\hbar} < \pi, \tag{6.1}$$

with the Bohr magneton $\mu_B/\hbar$, the maximum difference of magnetic field magnitude $\Delta|B|_{max}$, and free phase evolution time T, the time between Rabi pulses. The reason is that full phase information can only be maintained with a phase evolution difference of at most 180 degrees. Once the condition in Eq. 6.1 has been determined to be true in a setup using methods such as presented in Chapter 5, an eEDM search employing two pulses becomes viable (see Fig. 2.4).

We define a normalized signal, and show how this improves signal to noise ratio of the experiment. We use the photon fluorescence counts in sections B and D (see Fig. 3.1). The photon rate is subject to Poisson statistics. The observed fluctuation of the photon rate however, is dominated by the variation in the number of molecules N_{mol} produced in the supersonic source [94] (see Fig. 6.2). In order to account for this in the experiment we measure the photon rate at two locations. The spin-precession signal will then be based on the normalization. The measured photon rate signal is S_B at location B and S_B at location D. The signal S_D at location D is a function of the difference frequency $\omega_{PS}/2\pi$ (see Eq. 5.1) of the two co-propagating laser fields.

A useful measurement of S_B depends on two conditions. The first condition is a constant reliable ratio of signals S_D and S_B. We use transitions originating from rotational state N=0 for S_D and N=1 for S_B. This assumes that the rotational temperature of the molecular beam stays constant. By also choosing reliable transitions, which means that they lead to the fluorescent emission of at most a single photon per molecule, the first condition is satisfied. The second condition is $S_B \gg S_D$, so that the statistical uncertainty in S_B does not contribute significantly to uncertainty in the eEDM measurement. This second condition is best satisfied by measuring S_B close to the source. S_B is maximal there, since the experiment has a divergent BaF beam.

The signal at B

$$S_B = k_B N_{mol} + BG_B \tag{6.2}$$

depends upon the number of molecules N_{mol}, the rate of photons per molecule k_B and the background BG_B at location B. Without counterpropagating laser beam the signal at D

$$S_D = k_D N_{mol} + BG_D \tag{6.3}$$

[ii] The BaF source is also sufficiently stable over time in terms of velocity and velocity profile.

Table 6.1: Experiment parameters for the spectrum in Fig. 6.4. The actual pulses have a rise and fall time of $3.9\ \mu s$ each.

$\lvert E\rvert$	t	T	Delay	I_{DCC}	B_x	FG1 scan	FG1 steps
$2.00\ kV/cm$	$80\ \mu s$	$1\ ms$	$3.5\ ms$	$1.00\ mA$	$3\ nT$	$48\ kHz$	$240 \times 200\ Hz$

also depends upon the number of molecules N_{mol} [iii], but now with a rate of photons per molecule k_D and the background BG_D at location D. Eq. 6.2 is rearranged to

$$k_B N_{mol} = S_B - BG_B, \tag{6.4}$$

and Eq. 6.3 is rearranged to

$$k_D N_{mol} = S_D - BG_D. \tag{6.5}$$

The relative efficiency is

$$\epsilon_{D/B} = \frac{k_D}{k_B} = \frac{S_D - BG_D}{S_B - BG_B}. \tag{6.6}$$

In this experiment concerning eEDM searches a linear relation between S_D and S_B of the form

$$S_D = BG_D + \epsilon_{D/B} S_B \tag{6.7}$$

needs to be established for each dataset (e.g. see Fig. 6.3). The uncertainty in BG_D and $\epsilon_{D/B}$ limit the eEDM sensitivity. The normalized signal can be expressed as

$$C = \frac{S_D - BG_D}{S_B \epsilon_{D/B}}, \tag{6.8}$$

if the background BG_B is negligible, i.e. $BG_B \ll S_B$. The signal can be measured with maximal contrast by measuring C (see Eq. 2.8). This probes only the $|F = 1\rangle$ hyperfine state. C', which probes hyperfine state $|F = 0\rangle$, can be measured in a similar fashion. Both C and C' combined double the contrast (see Eq. 2.9), and also afford cross checks. The measurement of both C' and C is being implemented in the ongoing eEDM experiment. The signal C (and C') depends on the applied frequency $\omega_{PS}/2\pi$.

Understanding of the analysis of the signal (see Fig. 6.4), depends on the used parametrization [91, 92], experimental laser control [96], and the DAQ system [112]. The conditions inside the interaction zone are such, that the interference fringes are visible with high contrast. The central part (indicated by the arrow in Fig. 6.4) can be exploited for phase sensitive measurements, which in turn are sensitive to the magnetic field (see Section 6.2) and to the EDM, while a constant electric field is maintained.

[iii] For a normalized measurement, N_{mol} can be different for S_B and S_D. Important is the stability over time in the relative number of molecules per pulse.

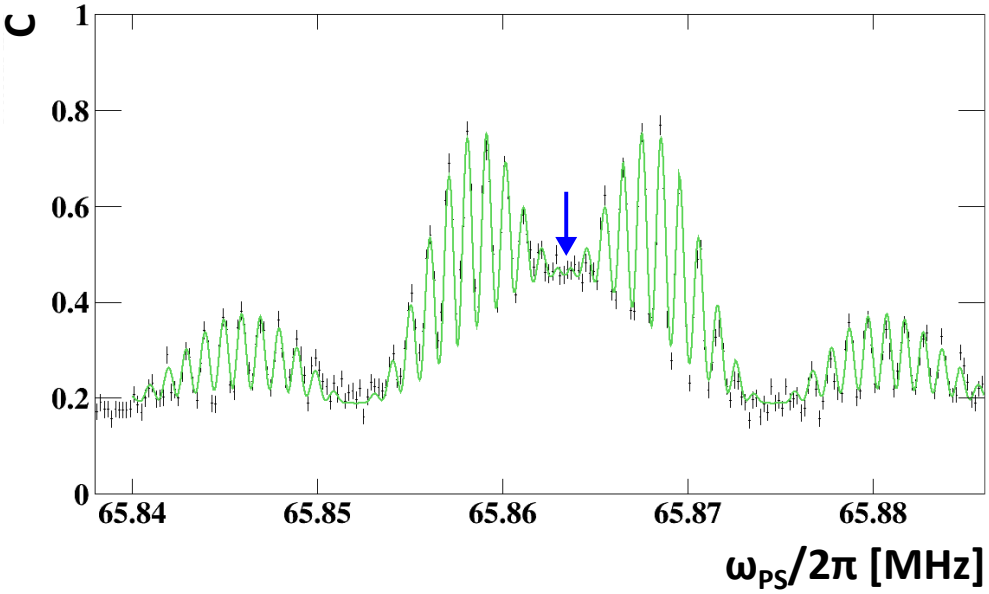

Figure 6.4: Interference signal from spin precession. It is detected by probing the $|F = 1\rangle$ state population. The difference between the two AOM frequencies $\omega_{PS}/2\pi$, is achieved by scanning one of the AOMs with frequency FG1 (see Fig. 3.20). The green line is a fit to the data based on an optical Bloch equation (OBE) model [91, 92]. For $N = 220$ degrees of freedom the reduced chi-squared $\chi^2/N = 1.5$. The width of the envelope function scales with $1/t$, and the width of the fringes scales with $1/T$ [119]. Set parameters are in Table 6.1.

6.2 Magnetic field

The magnetic field inside the interaction zone internal to the magnetic shield is

$$\vec{B}_{int} = \vec{B}_{shield} + \vec{B}_{coil} + \vec{B}_{ext} \times DSF_0, \tag{6.9}$$

with $\vec{B}_{shield}$ formed by the magnetic shield, $\vec{B}_{coil}$ generated by coils inside the shield, $\vec{B}_{ext}$ the magnetic field external to the magnetic shield, and DSF_0 the magnetic shield differential shielding factor for magnetic fields in the frequency limit $\nu \rightarrow 0$ Hz. $\vec{B}_{shield}$ arises from the remnant magnetization of the magnetic material in the shield, due to the state of degaussing and the hysteresis of the material. $\vec{B}_{coil} = |B_{DCC}|\hat{x}$ is applied via the double cosine coil (DCC). This includes interactions of the double cosine coil generated field with the magnetic shield and other material. An additional coil is available in the interaction zone that generates field $B_y\hat{y}$. The interaction of the coils in the interaction zone with the magnetic shield reduces spatial inhomogeneities and also causes hysteresis. These coil generated fields depend on the time stability of the power supplies. $\vec{B}_{ext}$ is the field at the location of the magnetic shield, due to the environmental magnetic field and the coils external to the magnetic shield.

A shielding factor SF at some magnetic field frequency ν_B for a magnetic shield is

$$SF(\nu_B) = \frac{|B_{ext}|}{|B_{int}|}(\nu_B) \tag{6.10}$$

Table 6.2: Common set parameters for the measurements in Fig. 6.5.

$\|E\|$	Delay	T	t	FG1 scan	FG1 steps
1.90 kV/cm	3.5 ms	800 µs	50 µs	40 kHz	200 × 200 Hz

is the ratio of the external magnetic field magnitude $|B_{ext}|$ and the internal magnetic field magnitude $|B_{int}|$. The differential shielding factor DSF at some magnetic field frequency ν_B for a magnetic shield is

$$DSF(\nu_B) = \frac{\Delta|B_{ext}|}{\Delta|B_{int}|}(\nu_B), \tag{6.11}$$

which is the ratio of the change in external magnetic field magnitude $\Delta|B_{ext}|$ and the change in internal magnetic field $\Delta|B_{int}|$. The differential shielding factor for static magnetic fields (right half in Fig. 3.2) is

$$DSF_0 = \lim_{\nu_B \to 0\ \mathrm{Hz}} DSF(\nu_B) = \frac{\Delta|B_{ext}|}{\Delta|B_{int}|}(\nu_B \to 0\ \mathrm{Hz}), \tag{6.12}$$

which is in the frequency limit $\nu_B \to 0$ Hz. [iv]

The external magnetic field of the experiment $\vec{B}_{ext}$ depends on the environmental magnetic field, which is evaluated in Chapter 4 employing flux gates. The magnetic field external to the magnetic shield, is described by

$$\vec{B}_{ext} = \vec{B}_{ext,env} + \vec{B}_{ext,coils}, \tag{6.13}$$

with a $\vec{B}_{ext,env}$ the environmental magnetic field of the experiment, and $\vec{B}_{ext,coils}$ the modification of the field by coils (see Fig. 3.3). In Section 6.2.2 the control by these coils of magnetic field $\vec{B}_{ext}$ is employed to measure the differential shielding factor DSF_0 of the magnetic shield.

6.2.1 Tuning the magnetic holding field with the double cosine coil

In the experiment the magnetic holding field corresponds to the internal magnetic field $\vec{B}_{int}$. Through $\phi_B = 2\mu_B|B_{int}|T/\hbar$ the magnetic holding field sets the experimental working point of the phase. The holding field is primarily adjusted by the double cosine coil field $\vec{B}_{DCC}$ (see Section 3.5.1 for design, Section 4.4 for characterization). For an EDM search the holding field is tuned to correspond to the desired phase $\phi = \pi/2$. Calculations around this working point (see Fig. 6.10(a) and (b)) indicate high sensitivity to the tuning of the phase with the magnetic holding field. Measurements in Fig. 6.5 illustrate the effect on the interference signal of adjusting the magnetic holding field with the double cosine coil. Common set parameters for these measurements are in Table 6.2.

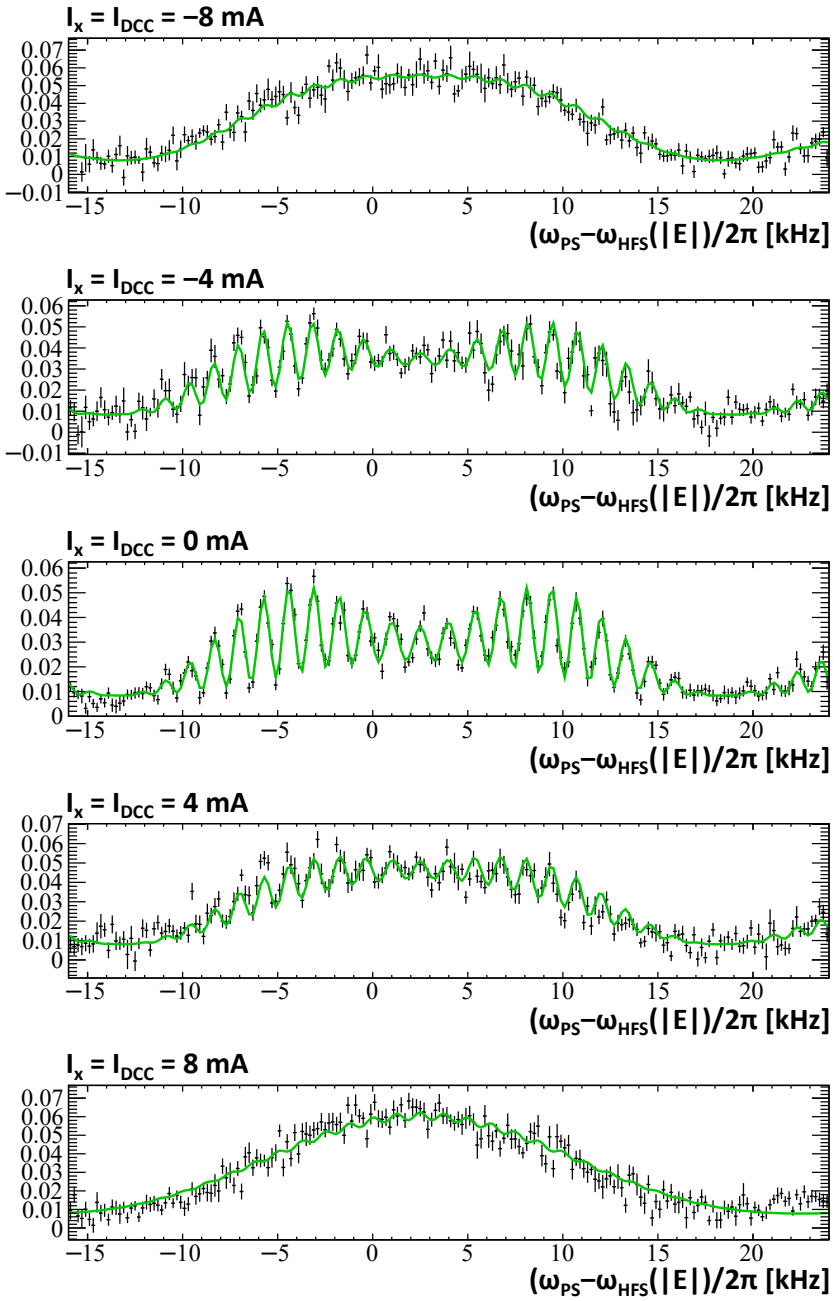

Figure 6.5: The interference fringes are sensitive to changes in the magnetic holding field. The double cosine coil (see Section 3.5.1) operated at different currents, from $I_{DCC} = -8$ mA to $I_{DCC} = 8$ mA, yields different magnetic holding fields. Common set parameters for the measurements are in Table 6.2. The evolution of the fringe pattern while changing the holding field matches the expectations. A change of current by 1 mA corresponds to a 3 nT field change (see Eq. 4.9).

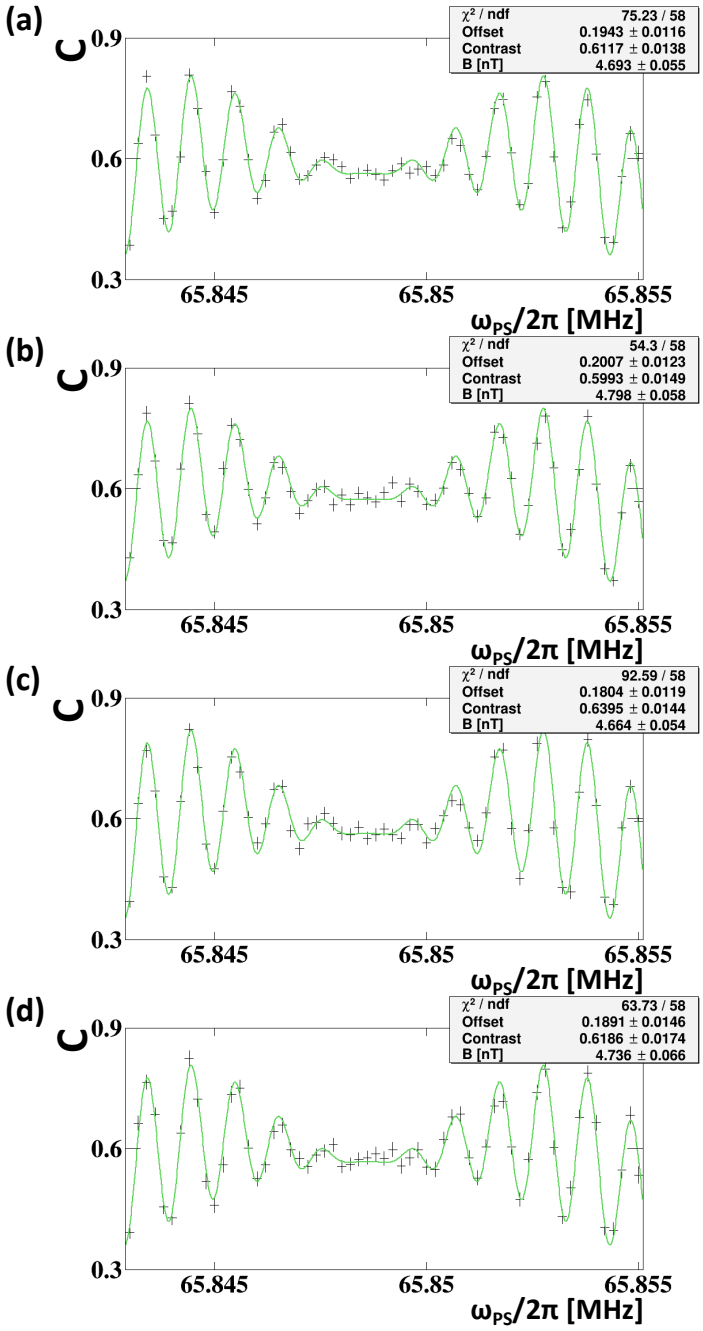

Figure 6.6: The differential shielding factor measurement uses spin interference to measure internal magnetic field $|B_{int}| = B$, while modifying the field external to the shield by $|B_{ext}| = B_{\mathrm{X}}$ in the following sequence: (a) $0(5)$ μT, (b) $+50(5)$ μT, (c) $-50(5)$ μT, (d) $0(5)$ μT. The fringe pattern changes only marginally (see also Fig. 6.7) for a change of 100 μT in the external field $\vec{B}_{ext}$.

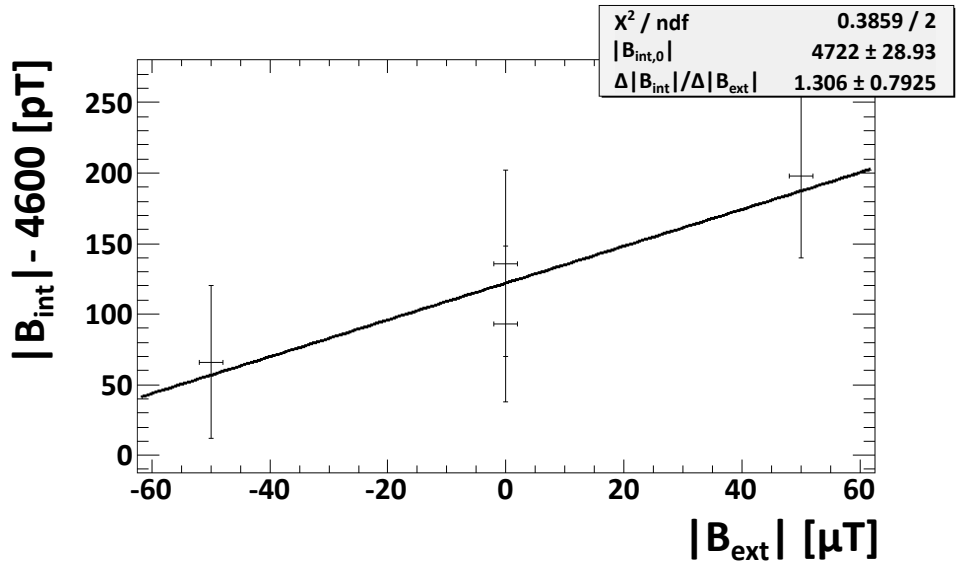

Figure 6.7: The combined data from Fig. 6.6 on the magnetic field external and internal to the magnetic shield, $|B_{ext}|$ and $|B_{int}|$ respectively, reveal an internal offset field $|B_{int,0}|= 4772(29)$ pT, and a suppression factor $\Delta|B_{int}|/\Delta|B_{ext}|= 1.3(8)$ pT/μT $= 1.3(8) \times 10^{-6}$. This corresponds to the differential shielding factor $DSF_0 = \Delta|B_{ext}|/\Delta|B_{int}| \approx 10^6$.

6.2.2 Differential shielding factor of magnetic shield

We now describe a method for determining the differential shielding factor DSF_0 of the magnetic shield. If $\Delta|B_{ext,env}| \ll \Delta|B_{ext,coils}|$, i.e. that environmental changes are much smaller than changes in coil generated fields. In that case a change in the external magnetic field $\vec{B}_{ext}$ is fully determined by a change in the coil generated fields $\vec{B}_{ext,coils}$. By only setting current I_{X} (see Section 3.3), the coil generated field becomes

$$\vec{B}_{ext,coils} = \frac{\Delta B_{\mathrm{X}}}{\Delta I_{\mathrm{X}}} I_{\mathrm{X}} \hat{X}. \tag{6.14}$$

For a current change ΔI_{X} we have a change of the external magnetic field

$$\Delta\vec{B}_{ext} = \Delta|B_{ext}|\hat{X} = \frac{\Delta B_{\mathrm{X}}}{\Delta I_{\mathrm{X}}} \Delta I_{\mathrm{X}} \hat{X} = \Delta B_{\mathrm{X}} \hat{X}. \tag{6.15}$$

The coil currents I_{Y} and I_{Z} can also be used to modify the external magnetic fields B_{Y} and B_{Z} respectively. Because of the symmetry of the magnetic shield (see Section 3.4) changes in B_{Z} are expected to yield a different shielding factor compared to B_{X} as discussed here.

The experimental sequence entails the application of an external magnetic field. A current $I_{ext,\mathrm{X}}$ in the external field coils (see Section 3.5.3), results in coil generated

[iv] In all subsequent uses of DSF_0 the magnetic field frequency ν_B dependence is elided for notational simplicity, i.e. $DSF_0 = \frac{\Delta|B_{ext}|}{\Delta|B_{int}|}$.

Table 6.3: Set parameters that are equal for the spectra in Fig. 6.8 and Fig. 6.9. The pulses have a rise and fall time of $3.9\ \mu s$ each. B_x is the generated field at center of double cosine coil for I_{DCC}, with generated fields tapering off to about $B_x/2$ at the entrance and exit of the 100 cm long coil.

$\lvert E\rvert$	t	I_{DCC}	B_x	FG1 scan	FG1 steps
$0.00\ \mathrm{kV/cm}$	$80\ \mu s$	$1.250\ \mathrm{mA}$	$3.75\ \mathrm{nT}$	$48\ \mathrm{kHz}$	$480 \times 100\ \mathrm{Hz}$

field B_X changing by $100\ \mu\mathrm{T}$ for $\Delta I_{ext,\mathrm{X}} = 13.5\ \mathrm{A}$ in the sequence in Fig. 6.6. The coil generated field changes are much larger than changes in the environmental magnetic fields of $\mathcal{O}(30\ \mathrm{nT})$ (see Fig. G.2). Each measurement in the sequence took about 30 minutes, each yielding a resolution of about $\sigma_{B_{int}} \approx 60\ \mathrm{pT}$. The resulting differential magnetic shielding factor (see Fig. 6.7) is

$$DSF_0 = \frac{\Delta|B_{ext}|}{\Delta|B_{int}|} = \frac{1}{1.3(8) \times 10^{-6}} \approx 10^6. \tag{6.16}$$

Laser frequency drift adds an extra frequency shift term on top of the magnetic field related changes. This indicates possibly even higher shielding factors. The entire sequence with 2 hours integration time was recorded with magnetic field resolution $\sigma_{B_{int}} \approx 30\ \mathrm{pT}$, which corresponds to a frequency resolution $\sigma_\nu \approx 0.8\ \mathrm{Hz}$.

Due to continuous monitoring with flux gates (see Chapter 4) the external magnetic field $|B_{ext}|$ can be evaluated employing the Allan variance (see Fig. G.2). The characteristic time scale for the experiment is between 10 to 100 s, which is determined by electric field switching. The observed Allan variance $\delta B(T_{ave} = 100\ \mathrm{s}) \approx 3\ \mathrm{nT}$ is a measurement of the magnetic field change external to the magnetic shield $\Delta|B_{ext}|$. With the differential shielding factor in Eq. 6.16 this corresponds to a change of $\Delta|B_{int}| \approx 3\ \mathrm{fT}$ inside the magnetic shield.

6.2.3 Length of homogeneous magnetic fields

Homogeneous electric and magnetic fields are ultimately limited by the inner dimensions of the magnetic shield and spacing requirements. The innermost magnetic shield cylinder is 130 cm long and has a 50 cm diameter. The for eEDM signals usable homogeneous magnetic field region even exceeds 120 cm length (see Fig. 6.8, Fig. 6.9, and Table 6.3). This indicates a possibility for upgrading the experiment. By increasing in length the conservatively chosen 60 cm generated homogeneous electric field region and the generated homogeneous magnetic field, the interaction zone could be extended by a factor 2. This would double the phase sensitivity, and hence the eEDM sensitivity. However, this requires an extension of the double cosine coil, of the vacuum chamber inside the double cosine coil, and of the electric field plates inside the vacuum chamber. The primary constraints are the spatial separation of the components, and the lead time necessary for equipment modification, in particular the double cosine coil and the electric field plates.

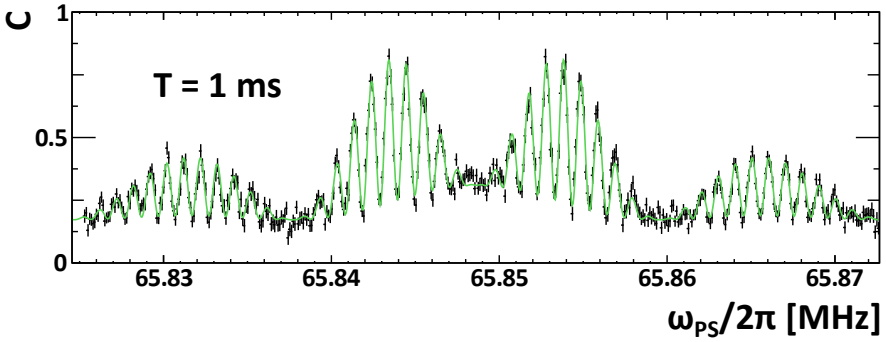

Figure 6.8: Spin precession for an interaction time $T = 1$ ms and a 3.3 ms delay (see Fig. 3.20), probes about a 60 cm distance. The Rabi phase is $\Omega_{PS}t = 1.005(3)\pi$. The observed magnetic field magnitude is $|B| = 2.53(4)$ nT.

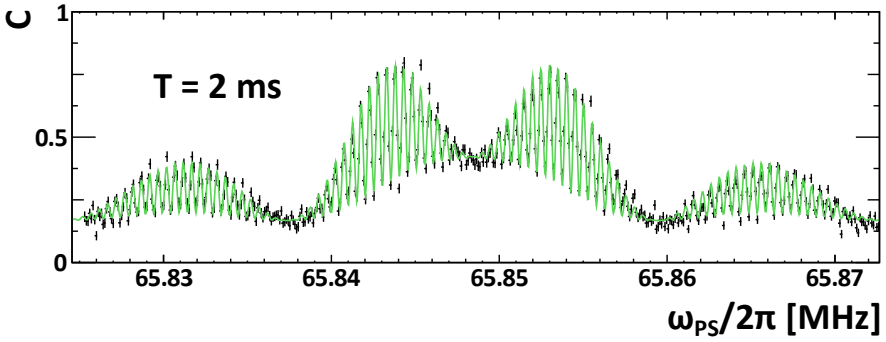

Figure 6.9: Spin precession for an interaction time $T = 2$ ms and a 2.8 ms delay (see Fig. 3.20), probes about a 120 cm distance, twice the distance as in Fig. 6.8. The Rabi phase is $\Omega_{PS}t = 1.001(3)\pi$. The observed magnetic field magnitude is $|B| = 1.86(2)$ nT. The number of fringes is doubled, but their contrast remains the same as for $T = 1$ ms, doubling the phase sensitivity. This shows the possibility of an upgrade of the experiment.

6.3 Electric field

While a change in magnetic field (see Fig. 6.10(a) and (b)) changes the population count $P_{\mathrm{F}=1}$ in the central part (at arrow in Fig. 6.4), a change in the electric field shifts the signal with respect to the frequency axis (see Fig. 6.10(c) and (d)). This enables a quantitative distinction between electric and magnetic field changes. The used OBE model [91, 92] enables the extraction of both the tensor Stark shift related phase, and the Zeeman effect and EDM related phase, and their precision increases with the same statistics. Crucially, when operating across the 8 kHz region (between $\delta = \pm 4$ kHz) instead of only $\delta = 0$ kHz, the sensitivity to an EDM only decreases by about 10%. This [v] leads to a significant reduction in necessary auxiliary measurements of experimental parameters, without compromising the statistics for EDM searches. The electric field

[v] What is described can be considered a form of co-electrometry (analogous to co-magnetometry): a measurement that is sensitive to the electric field, while remaining sensitive to an EDM.

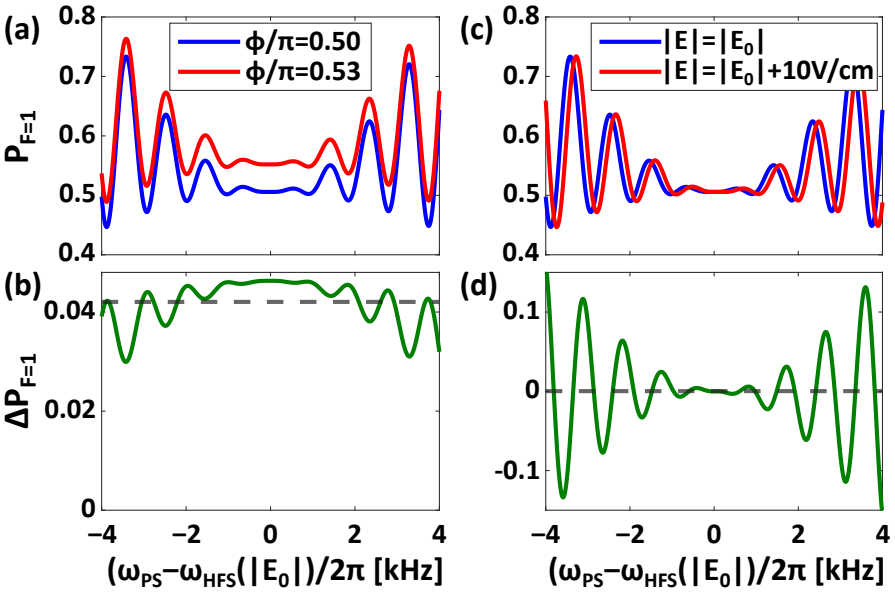

Figure 6.10: (a) Calculation of population $P_{\mathrm{F}=1}$ for different two-photon detuning $\delta = (\omega_{PS} - \omega_{HFS}(|E|))/2\pi$ around the working point of the experiment, i.e. $\Omega_{PS}t \approx \pi$, and $|E_0| = 2\,\mathrm{kV/cm}$, for $\phi/\pi = 0.50$ (blue) and $\phi/\pi = 0.53$ (red). (b) The difference between the red and blue curves in (a), i.e. $\Delta P_{\mathrm{F}=1}$ for a change of $\Delta\phi = 0.03\pi$ as function of the detuning. At $\delta = 0\,\mathrm{kHz}$, $P_{\mathrm{F}=1} \approx \sin^2(\phi/2)$ and therefore $\Delta P_{\mathrm{F}=1} \approx \phi/2$. The dotted line is $P_{\mathrm{F}=1}$ averaged over the interval $\delta = -4$ kHz to $\delta = 4$ kHz. (c) $P_{\mathrm{F}=1}$ as function of δ for $\Omega_{PS}t \approx \pi$ and $\phi = \pi/2$, for electric fields $|E| = |E_0|$ (blue) and $|E| = |E_0| + 10\ \mathrm{V/cm}$ (red). A change in the electric field results in a shift of the spectrum, with an electric-field dependence of the tensor Stark shift $\omega_{tensor}/2\pi$ of 14.9 Hz/(V/cm). (d) The difference between the red and blue curves in (c), i.e. $P_{\mathrm{F}=1}$ for a change of electric field $\Delta|E| = 10\ \mathrm{V/cm}$. This provides the sensitivity to the externally applied electric field due to $\omega_{tensor}(|E|)$. The average value (dotted line) remains zero in this case. The large values of $\Delta\phi$ and $\Delta|E|$ are chosen for visibility [91, 92].

change causes an experimentally observed shift of the spectrum (see Fig. 6.11), due to the electric field dependence of tensor Stark shift. This dependence was determined. Electric field changes less than $0.1\ \mathrm{V/cm}$ become observable.

6.4 Motional and transverse magnetic fields

In beam EDM experiments the static electric field gives rise to an additional motional magnetic field experienced by the moving beam particles. This motional field $\vec{B}_{v\times E}$ is perpendicular to the particle velocity and the electric field vector. This together with the static magnetic field components B_y and B_z transverse to the electric and magnetic holding fields (in direction $\hat{x}$), is discussed here. These magnetic fields are within one order of magnitude of the magnetic holding field, i.e. large enough to notice. The molecular sensitivity to these fields is suppressed by the tensor Stark

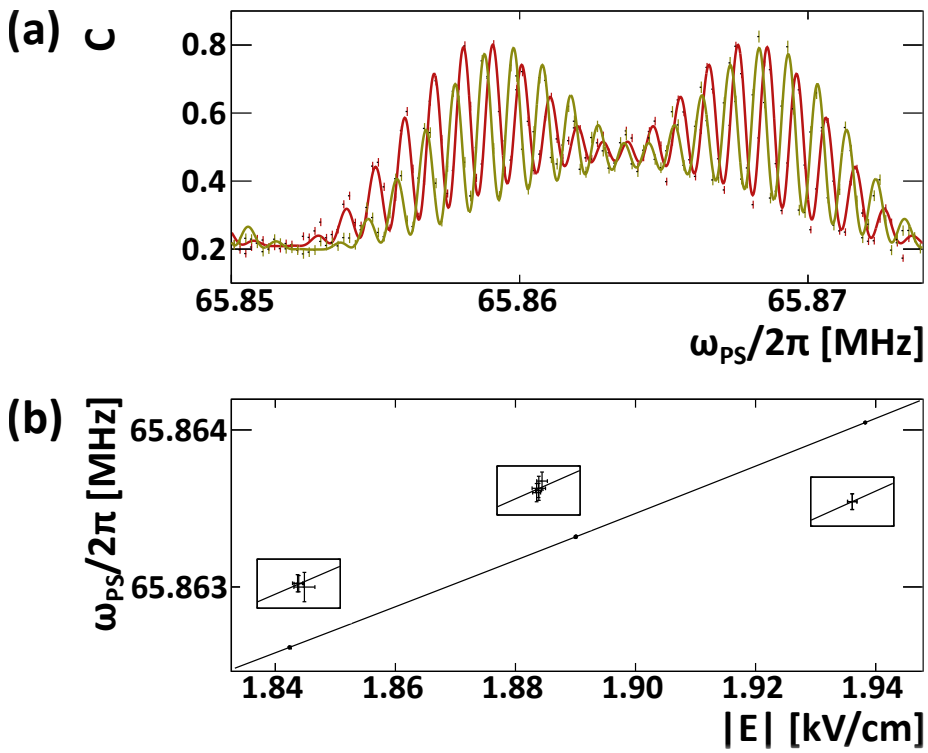

Figure 6.11: (a) Observed interference pattern for electric field $|E| = 1.8900(3)\ \mathrm{kV/cm}$ (red) and $|E| = 1.9383(3)\ \mathrm{kV/cm}$ (olivebrown). The electric-field-dependent hyperfine structure $\omega_{HFS}(|E|)$ is determined by the center frequency of the interference pattern. The magnetic field is $|B| = 4.04(7)\ \mathrm{nT}$ and the timings are $T = 1\ \mathrm{ms}$ and $t = 80\ \mu\mathrm{s}$. The contrast C (see Eq. 6.8) is the experimental realization of $P_{\mathrm{F}=1}$. The uncertainties of the data points are determined by the counting statistics of the fluorescence signal. (b) The hyperfine structure splitting $\omega_{HFS}(|E|)$ changes with the electric field by $14.99(7)\ \mathrm{Hz/(V/cm)}$ at $|E| = 1.9\ \mathrm{kV/cm}$. The three insets are at 100 times enlarged scale to show the uncertainties (i.e. $1\ \mathrm{V/cm}$, resp. 20 Hz) [91, 92].

effect. Starting from a static magnetic field in the laboratory frame

$$\vec{B}_{lab} = \begin{pmatrix} B_x \\ B_y \\ B_z \end{pmatrix}, \tag{6.17}$$

the magnetic field in the motional molecular frame becomes

$$\vec{B}_{mol} = \begin{pmatrix} B_x \\ B_y \pm B_{v\times E} \\ B_z \end{pmatrix}, \tag{6.18}$$

for velocity $\hat{v} = \hat{z}$ and electric field $\hat{E}_{plates} = \pm\hat{x}$ directions. $B_{v\times E}$ changes sign with electric field reversal. Detailed measurements and analysis are required to distinguish these fields from an EDM, since the term $B_y \pm B_{v\times E}$ reverses asymmetrically

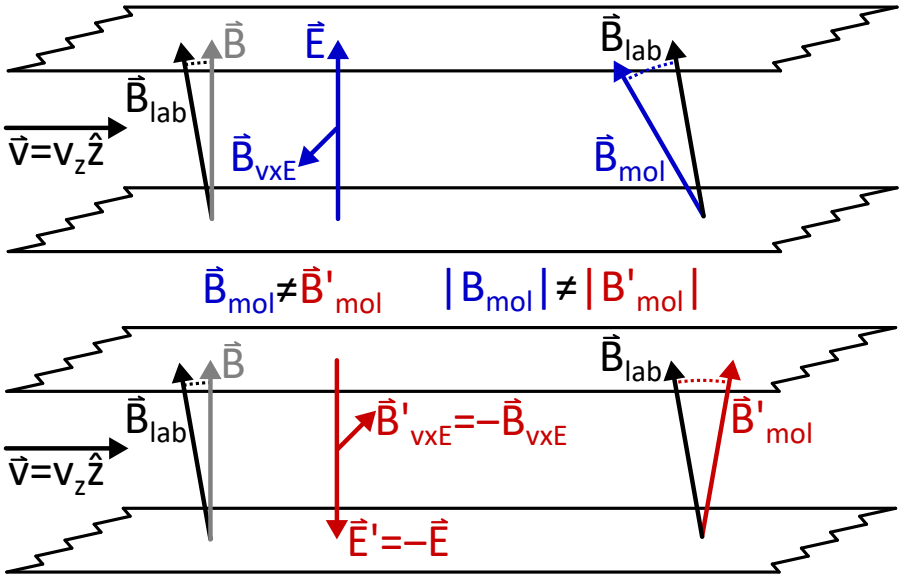

Figure 6.12: Sketch of motional and transverse magnetic fields in an EDM experiment. Electric field plates generate $\vec{E} = |E|\hat{x}$ between them (blue, upper drawing), or $\vec{E}' = -|E|\hat{x}$ (red, lower drawing) after field reversal. The molecules move through the electric field between the plates at velocity $\vec{v} = v_z\hat{z}$. The static laboratory field $\vec{B}_{lab}$ is imperfectly aligned with the electric field, i.e. in addition to the desired field $\vec{B}$ (grey) parallel/anti-parallel to the electric field, it has field components B_y and B_z transverse to the electric field. In the molecular frame arises motional magnetic field $\vec{B}_{v\times E}$ (blue) due to the motion through electric field $\vec{E}$, which becomes $-\vec{B}_{v\times E}$ (red) with electric field $\vec{E}' = -\vec{E}$. In the molecular frame, not only are the directions of the magnetic field asymmetrically different between $\vec{B}_{mol}$ (blue) before and $\vec{B}'_{mol}$ (red) after electric field reversal due to the static magnetic field components B_y and B_z transverse to the electric field. But also the magnitudes $|B_{mol}|$ before and $|B'_{mol}|$ after electric field reversal are asymmetrically different. The phases associated with these asymmetries have to be distinguished from an EDM phase.

along with an electric field reversal (see Fig. 6.12). This is treated in this section by answering the following questions. How large is the effect of the motional and transverse magnetic fields on the phase? What are the consequences for eEDM searches?

The molecules move through the interaction zone at velocity $\vec{v} = v_z\hat{z}$ in an electric field $\vec{E}_{plates} = |E|\hat{x}$ and a magnetic field $\vec{B}_{int}$ (see Eq. 6.9). This causes two competing electric field dependent effects in the molecule: a motional magnetic field

$$\vec{B}_{v\times E} = \frac{\vec{v}\times\vec{E}}{c^2} = \frac{v_z\hat{z}\times|E|\hat{x}}{c^2} = \frac{v_z|E|}{c^2}\hat{y} \tag{6.19}$$

transverse to the double cosine coil holding field $B_x|\hat{x} = B_{DCC}|\hat{x}$, and suppression of molecular sensitivity to all magnetic field components transverse to the electric field $\vec{E}_{plates}$ due to the tensor Stark shift $\omega_{tensor}(|E|)$ (see Section 5.3). For $\omega_{tensor}(|E|) \gg \mu_B|B|/\hbar$ with $|B|$ the magnetic field magnitude in the molecular frame, $|B| \gg |B_{v\times E}|$,

and $|B| \gg B_y$ [vi], the phase accumulation for electric field $\vec{E}_{plates} = |E|\hat{x}$ is

$$\phi = \mu_B T/\hbar \left(2B_x - \gamma_{tensor} \left(\frac{(B_y + B_{v\times E})^2}{|B|} \right) \right). \tag{6.20}$$

Here we have the magnetic moment $\mu_B/\hbar = 2\pi \times \mu_B/h$, the coherent interaction time T, the holding field $B_x = |B_{DCC}|$, the tensor Stark shift dependent suppression factor

$$\gamma_{tensor} = \left(\frac{\mu_B |B|/\hbar}{\omega_{tensor}(|E|)} \right)^2, \tag{6.21}$$

the magnetic field transverse to the holding field B_y, the electric field magnitude $|E|$, the molecular velocity v_z, and the speed of light c (see also Equation 14.64, page 548 in reference [27]). If the conditions for Eq. 6.20 are not satisfied, an approach employing matrix diagonalization [91] is needed.

For an EDM sensitive search the magnetic holding field B_x is typically tuned (see Section 6.2.1) such that the working point of the magnetic holding field phase is

$$\phi_B = 2\mu_B B_x T/\hbar = \pi/2. \tag{6.22}$$

In order to study the effect of the motional magnetic field and the transverse magnetic field on the phase $\phi_{v\times E,y}$ separately from the magnetic holding field phase ϕ_B, we subtract ϕ_B from Eq. 6.20

$$\phi_{v\times E,y} = \phi - \phi_B = -\frac{\mu_B T \gamma_{tensor}}{\hbar} \left(\frac{(B_y + B_{v\times E})^2}{|B|} \right) = -\frac{\mu_B T \gamma_{tensor}}{|B|\hbar} (B_y + B_{v\times E})^2. \tag{6.23}$$

What matters in an EDM search is the difference in phase accumulation, which for electric fields $\vec{E}_+ = +|E_+|\hat{x}$ and $\vec{E}_- = -|E_-|\hat{x}$ is

$$\Delta\phi_{v\times E,y} = \phi_{v\times E,y}(\vec{E}_+) - \phi_{v\times E,y}(\vec{E}_-). \tag{6.24}$$

The electric field magnitudes $|E_+|$ and $|E_-|$ are determined using the tensor Stark effect (see Section 6.3). Different electric field magnitudes $|E_+| \neq |E_-|$ yield

$$\Delta\phi_{v\times E,y} = -\frac{\mu_B T}{|B|\hbar} \left[\gamma_{tensor,|E_+|}(B_y + B_{v\times|E_+|})^2 - \gamma_{tensor,|E_-|}(B_y - B_{v\times|E_-|})^2 \right], \tag{6.25}$$

where $\gamma_{tensor,|E_+|}$ and $\gamma_{tensor,|E_-|}$ are different since they depend on the electric field magnitude (see Eq. 6.21). Similarly Eq. 6.19 also yields a different magnitude for $B_{v\times|E_+|}$ and $B_{v\times|E_-|}$. Eq. 6.25 simplifies for constant magnitudes $|E_+| = |E_-| = |E|$ for both electric field orientations to

$$\Delta\phi_{v\times E,y} = -\frac{\mu_B T \gamma_{tensor,|E|}}{|B|\hbar} \left[(B_y + B_{v\times E})^2 - (B_y - B_{v\times E})^2 \right], \tag{6.26}$$

since $\gamma_{tensor,|E|}$ and $B_{v\times E}$ (magnitude) remain constant for constant electric field magnitudes. To further simplify this equation, we discuss here the term

$$(B_y + B_{v\times E})^2 = B_y^2 + 2B_y B_{v\times E} + B_{v\times E}^2. \tag{6.27}$$

[vi] With the magnitude of magnetic field components transverse to the electric field $|B_T| = \sqrt{B_y^2 + B_z^2} = B_y$, assuming $B_z = 0$ nT.

In Eq. 6.27 the terms with

$$B_y^2 \quad \text{and} \quad B_{v\times E}^2 \tag{6.28}$$

are distinguishable from an EDM phase shift, since they do not change if the electric field direction reverses. The cross-term with

$$2B_y B_{v\times E}, \tag{6.29}$$

it is odd in $\vec{E}$, $\vec{B}$. This is the same behavior as displayed by an EDM. This term is also odd in $\vec{v}$. This is true even for equal electric field magnitudes between different switch states. Putting cross-term Eq. 6.29 back into Eq. 6.26 yields

$$\Delta\phi_{v\times E,y} = -\frac{\mu_B T \gamma_{tensor,|E|}}{|B|\hbar}\left[4B_y B_{v\times E}\right], \tag{6.30}$$

since only the cross-term remains for constant electric field magnitudes.

Distinguishing the phase in Eq. 6.25 or Eq. 6.30 in an EDM search experiment from an EDM phase requires additional information. For this a coil is implemented and available, capable of generating magnetic field component B_y (see Section 3.5.2), for measurement of the combined effect of the motional magnetic field and this B_y field on the phase difference. This method is sensitive to hysteresis, since it changes the magnetic field inside the magnetic shield. There are other methods, which add a symmetry to the experiment, so that there is a motional magnetic field parallel and a motional magnetic field anti-parallel to the B_y field. This can be achieved by having at the same time the electric field in opposite directions, or the velocity of the molecular beam in opposite directions. For example, both methods are present in a thallium beam based eEDM experiment [54]. One method, by introducing a third electric field plate, arrives at two opposite electric field directions. This experiment is designed such that a third plate can be added in the future (see Section 3.7). The other method, by adding a second molecular source, arrives at two opposite molecular velocity directions.

We use the magnitude $|\Delta\phi_{v\times E,y}|$ in the rest of the section, since here we are primarily interested in estimating the magnitude of the effect. For the remainder of the section we use Eq. 6.30, since we also assume constant electric field magnitudes for the estimates made. For probing an eEDM $d_e = 10^{-28}\,\mathrm{e\,cm}$ in BaF, switching between $\pm|E| = \pm 4\,\mathrm{kV/cm}$ corresponds to a frequency difference [91]

$$\Delta\nu_{\pm 4\mathrm{kV/cm}} = \nu_{+4\ \mathrm{kV/cm}} - \nu_{-4\ \mathrm{kV/cm}} \approx 0.18\ \mathrm{mHz}. \tag{6.31}$$

For a coherent interaction time $T = 1\ \mathrm{ms}$ that results in a phase difference

$$\Delta\phi_d = \Delta\omega T = 2\pi\Delta\nu_{\pm 4\ \mathrm{kV/cm}} T = 2\pi \times 0.18\ \mathrm{mHz} \times 1\mathrm{ms} \approx 1\ \mu\mathrm{rad}. \tag{6.32}$$

Even including the tensor Stark dependent suppression factor γ_{tensor}, the motional and transverse magnetic field change the (absolute value of the) phase difference by $|\Delta\phi_{v\times E,y}|$ (see Table 6.4 and Table 6.5). This is the same order of magnitude as the phase difference $\Delta\phi_d$ for $d_e = 10^{-28}\,\mathrm{e\,cm}$. In order to perform eEDM measurements at this or greater precision, it is critical to take into account the motional and transverse magnetic field. This necessitates adding to the experiment (some of) the symmetries discussed after Eq. 6.30.

Table 6.4: Parameters used in the analysis in Section 6.4 and Section 6.5, unless specified otherwise. * See Fig. 5.5. ** Based on Table 4.2.

T	TOF bin	l	v_z	$\lvert E\rvert$	$\omega_{tensor}(4\ \mathrm{kV/cm})/2\pi$
1 ms	51.2 µs	60 cm	600 m/s	4 kV/cm	55 kHz *

$\mu_B/\hbar$	B_x	$\Delta\lvert B\rvert/\Delta r$	$\Delta\lvert B\rvert/\Delta z$	$\lvert B_T\rvert$
88 (rad/s)/nT [118]	8.9 nT	$< 5(1)$ nT/10cm**	$< 2.46(6)$ nT/10cm**	< 2 nT

Table 6.5: Intermediate parameters derived from Table 6.4, are put into Eq. 6.30 to arrive at $|\Delta\phi_{v\times E,y}|$. $B_y \leqq \sqrt{B_y^2 + B_z^2} = |B_T| < 2$ nT, thus $B_y < 2$ nT.

$B_{v\times E}$	B_y	$\lvert B\rvert$	γ_{tensor}	$\lvert\Delta\phi_{v\times E,y}\rvert$
2.7 nT	< 2 nT	9.3 nT	5.6×10^{-6}	< 1.1 µrad

Table 6.6: A change of parameters in the experiment (marked with ′) in Table 6.4 changes the phase $\Delta\phi_{v\times E,y}$ (see Table 6.7).

T'	l'	v_z'	$\lvert E'\rvert$	B_x'	$\lvert B_T'\rvert$
10 ms	60 cm	60 m/s	4 kV/cm	0.89 nT	< 0.2 nT

Table 6.7: Intermediate parameters (marked with ′) derived from changed parameters in Table 6.6 and the remaining unchanged parameters in Table 6.4, are put into Eq. 6.30 to arrive at $|\Delta\phi'_{v\times E,y}|$. $B'_y \leqq \sqrt{B_y^2 + B_z^2} = |B'_T| < 0.2$ nT, thus $B'_y < 0.2$ nT.

$B'_{v'\times E}$	B'_y	$\lvert B'\rvert$	γ'_{tensor}	$\lvert\Delta\phi'_{v\times E,y}\rvert$
0.27 nT	< 0.2 nT	0.93 nT	5.6×10^{-8}	< 11 nrad

Changes in the experiment (e.g. Table 6.6 compared to Table 6.4) require a recalculation of the effect of these fields on the phase difference $|\Delta\phi'_{v\times E,y}|$ (see Table 6.7). An eEDM $d_e = 10^{-28}$ e cm and a coherent interaction time $T' = 10$ ms result in a phase shift difference

$$\Delta\phi'_d = \Delta\omega T' = 2\pi\Delta\nu_{\pm4\ \mathrm{kV/cm}}T' = 2\pi \times 0.18\ \mathrm{mHz} \times 10\ \mathrm{ms} \approx 11\ \mu\mathrm{rad}. \tag{6.33}$$

In this experimental configuration the motional and transverse magnetic field phase difference $|\Delta\phi'_{v\times E,y}|$ is about a factor 10^3 times smaller than the eEDM related phase difference $\Delta\phi'_d$. This reduces the necessity of adding to the experiment the symmetries discussed after Eq. 6.30. For another experimental configuration the phase term $|\Delta\phi''_{v\times E,y}|$ could be much larger than $\Delta\phi''_d$, which requires the measurement of this phase term with much greater precision.

6.5 Systematic effects

The effect of crucial parameters on the measured phase can be estimated by comparing the phase evolution associated with them to the eEDM phase difference $\Delta\phi_d$ with electric field flipping (see Eq. 6.32). Input parameters are in Table 6.4.

(1) In particular the phase difference $|\Delta\phi_{v\times E,y}|$ due to the transversal and motional magnetic field is estimated in Table 6.5. This phase changes with electric field flipping. It needs to be distinguished from an EDM with additional measurements.

(2) The rotation of the Earth causes a rotation of the experiment. This adds a phase $\Delta\phi_{Earth}$. The Earth rotates at angular frequency [120]

$$\omega_{Earth} = 72.7\ \mu\mathrm{rad/s}. \tag{6.34}$$

The experimental magnetic holding field parallel to the Earth's surface rotates at angular frequency

$$\omega_{Earth,Exp} = \omega_{Earth}\cos(\alpha)\cos(\Theta_L), \tag{6.35}$$

with α the angle between the magnetic holding field and north, and Θ_L the latitude of the experiment [103]. For this experiment, magnetic holding field B_x is at an angle with the north of about $\alpha \approx 60^{\circ}$. The latitude of Groningen is $\Theta_L = 53.13'0^{\circ}$. All these effects combined result in an additional phase

$$\Delta\phi_{Earth} = \omega_{Earth}\cos(\alpha)\cos(\Theta_L)T \approx 22\ \mu\mathrm{rad/s} \times 1\ \mathrm{ms} = 22\ \mathrm{nrad}. \tag{6.36}$$

This phase does not change with electric field flipping. It is therefore distinguishable from an EDM.

(3) The molecular beam accelerates towards Earth due to gravity. This acceleration g combined with transverse magnetic field gradient $\Delta|B|/\Delta r$ adds a phase $\Delta\phi_{gravity}$. The phase difference $\Delta\phi_{gravity}$ is maximal if the gradient changes only the field component in the $\hat{x}$ direction, i.e. $\Delta|B|/\Delta r = \Delta B_x/\Delta r$. Then the magnetic field changes

$$\Delta B(\tau) = \iint_0^T g\frac{\Delta|B|}{\Delta r}d\tau^2, \tag{6.37}$$

which for inserting values from Table 6.4, since $\Delta W(\tau) = \mu_B \Delta B(\tau)$, yields phase difference

$$\Delta\phi_{gravity} = \int_0^T \frac{\Delta W(\tau)}{\hbar}d\tau = \iiint_0^T \frac{\mu_B g}{\hbar}\frac{\Delta|B|}{\Delta r}d\tau^3 = \frac{\mu_B g}{6\hbar}\frac{\Delta|B|}{\Delta r}T^3 < 7.2\ \mu\mathrm{rad}, \tag{6.38}$$

where $g \approx 9.8\ \mathrm{m/s^2}$ is the gravitational acceleration, T is the coherent interaction time, and $\Delta|B|/\Delta r$ is the transverse gradient. This phase does not change with electric field flipping. It is therefore distinguishable from an EDM.

(4) Applying an electric potential U to electric field plates (see Section 3.7) to generate an electric field $\vec{E} = |E|\hat{x}$, results in a leakage current

$$I_{leak} = \frac{U}{R_{leak}} = \frac{|E|d}{R_{leak}}, \tag{6.39}$$

where R_{leak} is the resistance to this leakage current, and d is the distance between electric field plates. R_{leak} has been measured [112]. The leakage current results in an additional magnetic field in the experiment. If a surface current flows over the full conductive surface along direction $\hat{z}$, which we assume here, this magnetic field

Table 6.8: Parameters used to calculate $|\Delta\phi_{leak,y}|$ (see Eq. 6.43), in addition to parameters in Table 6.4. I_{leak} and $|B_{leak}|$ are intermediate calculated parameters.

μ_0 $[\frac{\mathrm{Tm}}{\mathrm{A}}]$	d [cm]	b [cm]	R_{leak} [GΩ]	I_{leak} [nA]	$\lvert B_{leak}\rvert$ [fT]
1.26×10^{-6} [118]	4	9	700 [112]	23	161

causes the largest effect on the phase. This surface leakage current results in an additional magnetic field

$$\vec{B}_{leak,\pm} = \pm|B_{leak}|\hat{y}, \tag{6.40}$$

for electric field

$$\vec{E}_{plates,\pm} = \pm|E|\hat{x}, \tag{6.41}$$

with the electric field parallel (+) or anti-parallel (−) to the magnetic holding field B_x. We estimate for $b \gg d$

$$|B_{leak}| = \frac{\mu_0 I_{leak}}{2b} = \frac{\mu_0 |E| d}{2b R_{leak}}, \tag{6.42}$$

where μ_0 is the vacuum magnetic permeability, $|E|$ is the electric field, d is the distance between electric field plates, b is the height of electric field plate conductive area, and R_{leak} is the leakage resistance. The leakage current I_{leak}, by taking the magnitude of Eq. 6.30 and replacing $B_{v\times E}$ with $|B_{leak}|$, results in a phase shift difference with electric field flipping

$$|\Delta\phi_{leak,y}| = \frac{\mu_B T \gamma_{tensor,|E|}}{|B|\hbar}\left(4B_y|B_{leak}|\right) < 1.4 \times 10^{-10}\ \mathrm{rad}, \tag{6.43}$$

which is arrived at by inserting the parameters in Table 6.8 and Table 6.4 into Eq. 6.42 and subsequently Eq. 6.43. This phase changes with electric field flipping. It needs to be distinguished from an EDM with additional measurements.

(5) A time resolution of $\Delta T = 1$ ns for coherent interaction time $T = 1$ ms on a single BaF molecular pulse results in a phase difference

$$\Delta\phi_{\Delta T} = \frac{2\mu_B B_x \Delta T}{\hbar} = \phi_B \frac{\Delta T}{T} = \frac{\pi}{2} \times 10^{-6} \approx 1.6\ \mu\mathrm{rad}, \tag{6.44}$$

operating at the working point of the phase $\phi_B = \pi/2$ (see Section 6.2.1). The Rigol function generator with the Rb-clock as frequency reference (see Section 3.1), attains a timing resolution $\Delta T \ll 1$ ns, hence $\Delta\phi_{\Delta T} \ll 1$ µrad. This phase does not change with electric field flipping. It is therefore distinguishable from an EDM.

(6) The BaF molecular beam has a diameter D, of which the distribution of particles in magnetic field gradients probes different magnetic fields. This leads to a magnetic field gradient shift. The goal here is to get a lowest order worst case estimate. One can describe a beam diameter

$$D_{beam}(z) = \frac{\Delta D}{\Delta z}(z - z_0) + D_{z_0} \tag{6.45}$$

in cm as a function of the distance $z - z_0$ in m from the skimmer part of the source, and the beam divergence $\Delta D/\Delta z$ in cm/m, and the initial beam diameter D_{z_0} in cm.

At the skimmer the beam diameter $D_{skimmer} = D(z_0 = 0.27\,\mathrm{m}) = D_{z_0} = 0.5\,\mathrm{cm}$ (see Section 3.1). At the detection region the detected beam diameter $D_{detected} = D(z = 3.84\,\mathrm{m}) = 2.0\,\mathrm{cm}$. Hence the estimated beam diameter [vii] for the experiment is

$$D_{beam}(z) = \frac{(2.0 - 0.5)\,\mathrm{cm}}{(3.84 - 0.27)\,\mathrm{m}}(z - 0.27\,\mathrm{m}) + D_{z_0} = 0.42\,\frac{\mathrm{cm}}{\mathrm{m}}(z - 0.27\,\mathrm{m}) + 0.5\,\mathrm{cm}. \quad (6.46)$$

If the interaction zone lies between $z = 2.05\,\mathrm{m}$ and $z = 2.70\,\mathrm{m}$ (see Fig. 5.7), these respectively correspond to a beam diameter $D(z = 2.05\,\mathrm{m}) = 1.25\,\mathrm{cm}$ and $D(z = 2.70\,\mathrm{m}) = 1.52\,\mathrm{cm}$. Magnetic field gradients are different for different values of z (see Table 4.2), which can be described in a more detailed calculation. Since the goal is to perform a lowest order estimate, we take the average beam diameter

$$D_{ave} = \frac{D(z = 2.05\,\mathrm{m}) + D(z = 2.70\,\mathrm{m})}{2} = 1.38\,\mathrm{cm}, \quad (6.47)$$

i.e. the maximum relative distance of particles in the beam is taken to be $\Delta D = D_{ave}$. The worst case estimate on the magnetic field gradient transverse to the $\hat{z}$ direction is $\Delta|B|/\Delta r$ in Table 6.4. The phase difference $\Delta\phi$ is maximal if this gradient changes only the field component in the $\hat{x}$ direction, i.e. $\Delta|B|/\Delta r = \Delta B_x/\Delta r$. Taking the maximum relative distance of particles in the beam ΔD then yields an estimated absolute value of the magnetic field gradient shift

$$|\Delta\phi_{\Delta D}| = \frac{2\mu_B T}{\hbar}\frac{\Delta|B|}{\Delta r} \times \Delta D \lesssim 1.2 \times 10^5\ \mu\mathrm{rad}. \quad (6.48)$$

Though large compared to the eEDM phase, this phase does not change with electric field flipping. This only causes a phase offset. It causes a broadening of the phase distribution if taking the full beam properties and magnetic field gradients into account. Which also does not change with electric field flipping. Since such broadening would have been observed as a broadening of the structure in all figures in this chapter containing spin interference fringes, this effect appears not yet prohibitive in terms of phase sensitivity.

Similar to Table 5.4 in [103] we arrive for the experiment at a table of covered systematic effects (see Table 6.9). Although some of the effects are rather large, for EDM searches only their change with a change in the electric field matters, i.e. with electric field flipping.

6.6 Conclusion

The combination of

1. a well defined time, location and phase of the two-photon pulses interacting with BaF,
2. a well defined signal, including source fluctuation normalization,
3. and a homogeneous electric and magnetic field region,

yield high resolution spin precession signals. The measurement of both normalized signals C and C' is being implemented.

[vii] Of detected BaF molecules.

Table 6.9: Summary of examined systematic effects (1)-(6). For a given parameter, there is an effect on the experiment. The effect size of the parameter corresponds to a phase difference in the experiment. This is compared to the eEDM phase difference observed in BaF with electric field flipping if the eEDM $d_e = 10^{-28}\,\mathrm{e\,cm}$ (see Eq. 6.32). The column Flip refers to whether the phase difference for a parameter changes if the electric field is flipped. The column Fit refers to whether the parameter is part of the fit procedure developed in [91, 92] (e.g. see Section 6.3).

	Flip	Fit	Phase Shift [μrad]
eEDM in BaF (Eq. 6.32)	yes	yes	≈ 1
(1) $B_{v\times E}$ and B_T (Table 6.5)	yes	yes	< 1.1
(2) Earth rotation (Eq. 6.36)	no	no	$\approx 2.2 \times 10^{-2}$
(3) Gravity (Eq. 6.38)	no	no	< 7.2
(4) Leakage current and B_T (Eq. 6.43)	yes	no	$< 1.4 \times 10^{-4}$
(5) Timing (Eq. 6.44)	no	no	$\ll 1$
(6) Magnetic gradient shift (Eq. 6.48)	no	no	$\lesssim 1.2 \times 10^{5}$

The magnetic field can be tuned to the desired phase working point by tuning the magnetic holding field, using in particular the double cosine coil for this purpose. The magnetic field stability of the interaction zone, due to the laboratory environment and differential shielding factor of the magnetic shield, is not a limiting factor for eEDM searches. With adequate modification the interaction zone can be increased in size by a factor 2, which increases the experimental sensitivity.

Methods for analysis are developed [91, 96, 112]. A new approach to spin precession, using Optical Bloch Equations (OBEs) for calculations [91, 92], treats multiple parameters such that sensitivity to their systematic effects are included in the eEDM sensitive searches. This includes in particular the electric and the magnetic field (see Fig. 6.10).

One systematic effect, which arises due to the combination of motional and transverse magnetic fields, was discussed in Section 6.4.

The effect of several systematics on the phase difference are estimated, and compared to an eEDM phase. With electric field flipping the motional and transverse magnetic field causes a phase difference larger than the phase difference that would be caused by an eEDM $d_e = 10^{-28}\,\mathrm{e\,cm}$. Parameters such as these have to be monitored closely during experimental runs, and they have to be integrated into the analysis of the resulting data.

7 Summary

Permanent electric dipole moments (EDMs) violate parity (P) and time reversal (T) symmetries. Assuming combined CPT symmetry, EDMs also violate the combined CP symmetry. New searches of CP violation beyond the Standard Model (SM), could for example contribute to explaining the matter-antimatter asymmetry in the universe. A new experiment to search for an EDM on the electron (eEDM), set up by the NL-eEDM collaboration, employs a molecular BaF beam. The purpose is to find or limit CP violation beyond the SM. The actual experiment is performed on a superposition state in the BaF molecule. This state experiences in external electric and magnetic fields during coherent interaction time T a phase accumulation

$$\phi = \int_0^T \frac{\Delta W(\tau)}{\hbar} d\tau \tag{7.1}$$

related to an energy difference $\Delta W(\tau)$, which arises from the interaction between the molecule and the external fields. If an EDM exists, $\Delta W(\tau)$ and hence ϕ are different for a change in relative orientation of the magnetic and electric fields, e.g. by reversing one of them. In the experiment the phase ϕ is measured.

For the experiment we have built an interaction zone through which a BaF beam passes. The investigation on the superposition state takes place in a 5 layer µ-metal magnetic shield, which was newly developed for the NL-eEDM experiment. Together with additional Helmholtz-like compensation coils we achieve external magnetic field compensation to the 10^{-6} level. For inside the magnetic shielding we developed a new double cosine Θ coil. It provides a magnetic field of $\mathcal{O}(10\,\mathrm{nT})$, with 2% relative precision in space and $\mathcal{O}(\mathrm{pT})$ stability in time.

The magnetic field in the experiments' central interaction zone was first characterized with flux gates and then together with the electric field in spectroscopy experiments. The latter exploited the superposition of $X^2\Sigma^+$, $|F = 1, m_F = 1\rangle$ and $|F = 1, m_F = -1\rangle$ hyperfine states of BaF.

Experimental searches for an eEDM require a quantitative discussion of the apparatus and the measurement principle. In particular the symmetry of the setup is of crucial importance. In the first part of the thesis care was taken for the generation of homogeneous electric and magnetic fields. In parallel further aspects of an EDM search were addressed in accompanying theses on the details of the measurement process [91], the implementation and use of the laser systems [96], and the data acquisition system [112].

The second part of the thesis discusses the performance when all parts are integrated in one experiment. Measurements demonstrate how to measure (and map)

electric fields and magnetic fields to $\mathcal{O}(100\,\mathrm{Hz})$ frequency resolution with one pulse laser spectroscopy. Two pulse laser spectroscopy shows interference fringes with high contrast and high frequency resolution. One way this has been exploited, is to determine the shielding performance of the magnetic shield. It was also used to determine that the length of the usable homogeneous magnetic field region extends to more than twice the initially designed region.

The experiment to search for a permanent eEDM employing BaF is very sensitive to potential systematic effects. Those were examined and approached by developing a new measurement strategy [91, 92], and by investigating the effects not removed by this measurement approach. Among these is the motional magnetic field, which a moving particle experiences passing through an external electric field. We find in contrast to previous treatments that this is important, once the experiment reaches the eEDM level of $10^{-28}\,\mathrm{e\,cm}$.

First measurements show that the experiment works and that in one day we can expect $\sigma_d \approx 10^{-26}\,\mathrm{e\,cm\,day^{-1}}$ sensitivity. In the future the experiment will be improved by a slower BaF beam [99, 121], higher molecular flow rates [122] and improved light collection. With this a search with competitive eEDM result can be expected.

8 Nederlandse samenvatting

Beheersing van elektrische en magnetische velden voor zoektochten naar elektrische dipoolmomenten

Permanente elektrische dipoolmomenten (EDM's) schenden pariteits- (P) en tijdsomkeringsymmetrie (T). Als we aannemen dat CPT een symmetrie van de natuur is, schenden EDM's ook de combinatie van CP-symmetrie. Nieuwe zoektochten naar CP-schending voorbij wat het Standaard Model (SM) voorspelt, kunnen bijdragen aan een verklaring van bijvoorbeeld de onbalans van materie en antimaterie in het universum. Een nieuw experiment voor het zoeken naar een EDM van het elektron (eEDM), opgesteld door de NL-eEDM collaboratie, maakt gebruik van een moleculaire BaF bundel. Het doel is het vinden van of begrenzen van CP-schending voorbij wat het SM voorspelt. Het daadwerkelijke experiment maakt gebruik van een superpositietoestand in het BaF molecuul. Deze toestand ondervindt in externe elektrische en magnetische velden gedurende een coherente interactietijd T een fase-accumulatie

$$\phi = \int_0^T \frac{\Delta W(\tau)}{\hbar} d\tau \tag{8.1}$$

gerelateerd aan een energieverschil $\Delta W(\tau)$, die ontstaat door de interactie tussen het molecuul en de externe velden. Als een EDM bestaat, dan verandert $\Delta W(\tau)$ en daardoor ook ϕ door een verandering van de relatieve orientatie van elektrische en magnetische velden, bijvoorbeeld door één van tweëen om te draaien. In het experiment wordt de fase ϕ gemeten.

We hebben een interactiegebied gebouwd voor het experiment, waar een BaF bundel doorheen gaat. De meting aan de superpositietoestand vindt plaats binnen een 5 laags μ-metaal magnetisch schild, nieuw ontwikkeld voor het NL-eEDM experiment. Samen met extra Helmholtz-achtige compensatiespoelen hebben we een compensatie van het externe magnetisch veld tot 10^{-6} niveau bereikt. We hebben een dubbele cosinus Θ spoel ontwikkeld voor binnenin het magnetisch schild. Het levert een magnetisch veld van $\mathcal{O}(10\,\mathrm{nT})$ op, met 2% relatieve precisie in ruimte en $\mathcal{O}(\mathrm{pT})$ stabiliteit over tijd.

Het magnetische veld in het interactiegebied, dat centraal ligt in het experiment, is eerst in kaart gebracht met flux gates, en daarna is het samen met het elektrisch veld in kaart gebracht met spectroscopie-experimenten. Dat laatste maakte gebruik van de superpositie van $X^2\Sigma^+$, $|F=1, m_F=1\rangle$ en $|F=1, m_F=-1\rangle$ hyperfijn toestanden van BaF.

Experimentele zoektochten naar een eEDM hebben zowel een kwantitatieve discussie van de apparatuur alswel een meetprincipe nodig. Met name de symmetrie van de opstelling is van cruciaal belang. In het eerste deel van het proefschrift is gezorgd voor het genereren van homogene elektrische en magnetische velden. Tegelijkertijd is er aan andere aspecten van EDM zoektochten gewerkt in vergezellende proefschriften. Deze bevatten details over de meetprocedure [91], de implementatie en het gebruik van laser systemen [96] en het dataverwerkingssysteem [112].

Het tweede deel van het proefschrift bespreekt de prestaties van het experiment na het combineren van alle onderdelen tot één geheel. Metingen tonen hoe elektrische en magnetische velden in kaart te brengen met één-puls laserspectroscopie, tot een frequentie resolutie van $\mathcal{O}(100\ \mathrm{Hz})$. Twee-puls laserspectroscopie levert interferentiepatronen met hoog contrast en precieze frequentieresolutie. Eén manier waar hiervan gebruik gemaakt is, is voor het bepalen van de mate van afscherming door het magnetisch schild. Hiermee is ook bepaald dat de bruikbare lengte van het homogene magnetisch veldgebied meer dan twee maal zo groot is als de origineel ontworpen lengte.

Het experiment voor zoektochten naar een permanent eEDM door middel van BaF is heel gevoelig voor potentiële systematische effecten. Deze zijn onderzocht en benaderd door een nieuwe meetstrategie te ontwikkelen [91, 92], en door effecten die niet worden weggenomen door deze meetstrategie uit te zoeken. Eén hiervan is het bewegings magnetisch veld, dat een deeltje ervaart als het door een elektrisch veld beweegt. In tegenstelling tot eerdere beschouwingen hebben wij ontdekt dat dit van belang is, zodra het experiment een niveau equivalent aan een eEDM van $10^{-28}\ \mathrm{e\,cm}$ bereikt.

De eerste metingen tonen aan dat het experiment werkt, en dat we een gevoeligheid in één dag van $\sigma_d \approx 10^{-26}\ \mathrm{e\,cm\,dag^{-1}}$ kunnen verwachten. In de toekomst zal het experiment verbeterd worden door een langzamere BaF bundel [99, 121], intensere molecuulbronnen [122] en verbeterde detectie van licht. Hiermee is een zoektocht met een competitief eEDM resultaat te verwachten.

Acknowledgments

I would like to thank both Klaus Jungmann and Lorenz Willmann for giving me the opportunity to do a PhD and your valuable supervision. And I would like to thank the reading committee, Paulo Crivelli, Julia Even and Gerco Onderwater, for the willingness to review the thesis, as well as the helpful feedback. Furthermore, I would like to thank Alexander, Anno and Ginny (the fast-beam-lab-crew) for a pleasurable and productive collaboration. I also would like to thank the other members of the NL-eEDM collaboration for the range and richness of perspectives: Anastasia, Artem, Joost, Kevin, Maarten, Pi, Parul, Rick, Rob, Roman, Steven, Ties, Wim, Yanning, Yongliang. I would like to thank Oliver, Hilde and Leo for their valuable support. And I would like to thank my paranymphs Anno and Ginny for their support in preparing my defense.

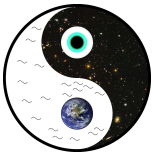

A Conventions

Table A.1: The notation and corresponding meaning are as denoted here, unless specified otherwise.

Notation	Meaning
$\vec{A}$	Vector A
$\lvert A\rvert$	Magnitude of vector A
$\hat{A} = \frac{\vec{A}}{\lvert A\rvert}$	Direction of vector A
Small cap	Axes inside magnetic shield
$\hat{x}$	Horizontal left direction, looking from the source, direction of x axis
$\hat{y}$	Vertical up direction, direction of y axis
$\hat{z}$	Direction (expected) of BaF beam axis in setup, direction of z axis
Capital	Axes outside magnetic shield
$\hat{X}$	Horizontal left direction, looking from the source, direction of X axis
$\hat{Y}$	Vertical up direction, direction of Y axis
$\hat{Z}$	Direction (expected) of BaF beam axis in setup, direction of Z axis
A_x	Magnitude of component of vector with direction $\hat{x}$
A_y	Magnitude of component of vector with direction $\hat{y}$
A_z	Magnitude of component of vector with direction $\hat{z}$
A_X	Magnitude of component of vector with direction $\hat{X}$
A_Y	Magnitude of component of vector with direction $\hat{Y}$
A_Z	Magnitude of component of vector with direction $\hat{Z}$
$A_\parallel$	The component of A parallel to B, B defined in text
$A_\perp$	The (combined) component(s) of A perpendicular to B, B defined in text

B Vacuum system for an eEDM experiment

B.1 Purpose of and requirements on the vacuum system

At the center of the interaction zone electric field plates (75 cm x 10 cm x 1 cm) generate a 4 kV/cm field, between which a BaF beam passes. We also have lasers interacting with the BaF beam between the plates. This needs to happen in a vacuum, i.e. residual gas pressure $p < 10^{-7}$ mbar. This corresponds to a mean free path of 600 meter for N_2 at room temperature. All components in the interaction zone have to be non-magnetic. All the components close to the interaction zone need to be close to non-magnetic (i.e. magnetic susceptibilities close to zero). Stainless steel outside the magnetic shield is just tolerable (see Section 3.6). We need three things:

1. A central vacuum system to contain the electric field electrodes and optical components for laser light.
2. Vessel pipes to this central system to maintain vacuum and provide for the BaF beam passing through.
3. Optical fiber feedthroughs for laser light and HV feedthroughs for connecting the electric field plates.

In this appendix we discuss materials employed in the vacuum system that in particular have to be (close to or completely) non-magnetic (see Section B.2). And we discuss how to reach the desired vacuum properties, in particular $p < 10^{-7}$ mbar (see Section B.3).

B.2 Vacuum materials

We need a sufficiently non-magnetic vacuum system at pressures below $p = 10^{-7}$ mbar. The whole system is depicted in Fig. B.1. Titanium tubes (yellow) provide access for BaF/laser beams at one end, and BaF beam access at the other end. The purple-gray object represents the double cosine coil, fitted around the glass vacuum tube. The red part is a mechanical support for the assembly, made from Ertalyte material.

The gray flanges are titanium. How the flanges are fitted to the glass tube (transparent yellow) is in Fig. B.2, a zoom-in of Fig. B.1. A reshaped teflon O-ring (white) prevents that the titanium flanges and the glass tube touch. There are two Viton O-rings (both black, one flat, one round). They also keep the titanium flanges and the glass tube separate. The round Viton O-ring provides a vacuum-tight seal. This Viton O-ring is squeezed between the titanium flange (gray, here to the left of the O-ring)

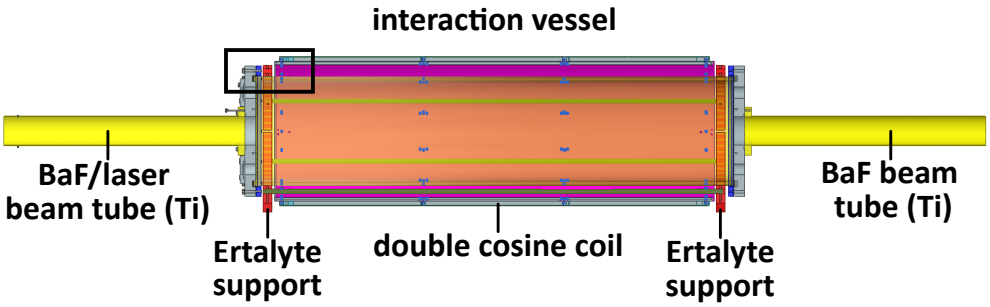

Figure B.1: Overview of vacuum system inside magnetic shield. The box top left indicates the zoom-in shown in Fig. B.2.

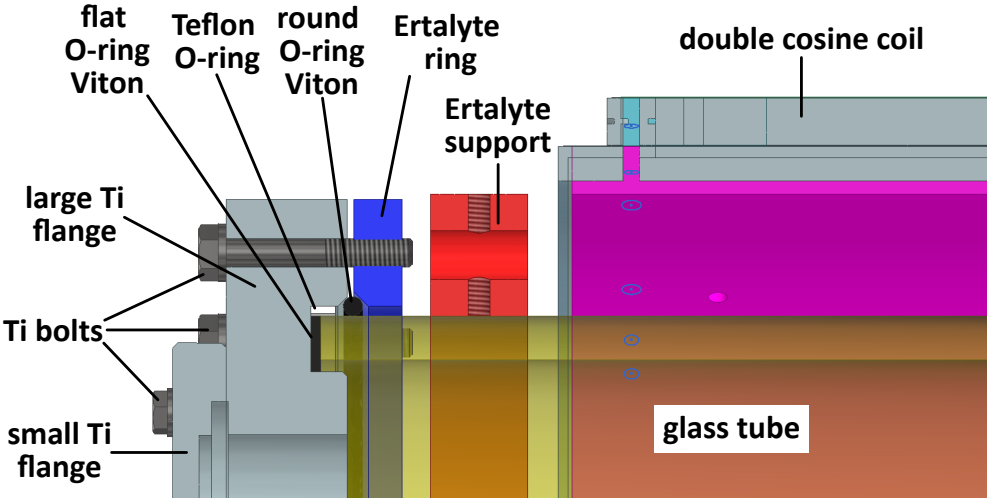

Figure B.2: Drawing of titanium flange to glass tube fitting. The large titanium (Ti) flange is 3 cm thick.

and an Ertalyte ring (blue, here to the right of the O-ring) with bolts. All used bolts are made from titanium. The double cosine coil (gray-purple) surrounds and is mounted to the glass tube. Ertalyte supports (red) maintain the position of the whole assembly inside the magnetic shield (see Fig. 3.10). All materials are non-magnetic.

B.3 Vacuum properties

The diameter of the titanium beam pipes is the rate limiting factor for achieving a sufficiently low residual gas pressure inside the glass tube. For $p < 10^{-7}$ mbar we need to consider the outgassing of the glass tube and the conductance of the titanium beam pipes. We are in this pressure range in the realm of molecular flow.

The residual gas pressure in our vacuum system is limited by its outgassing rate, which is determined by its surface area. The surface area A of the glass tube and the

large titanium endcaps is

$$A = \pi d \left(\frac{d}{2} + h \right) \approx 10^4 \text{ cm}^2 = 1 \text{ m}^2 \tag{B.1}$$

for diameter d = 25 cm and height h = 110 cm, which is large compared to the surface of the rest of the vacuum system. Heating the system for faster outgassing is not a viable option due to the sensitivity of the μ-metal to temperature. Further risks include deforming and stressing the glass tube, and the melting of plastics (e.g. the protective VDS layer outside the glass), seals and other materials.

We are guided in our vacuum design by information available in a vacuum handbook by Pfeiffer Vacuum [111]. The conductance C_{pipe} (in liters/second (L/s)) of a round pipe with diameter d and length l (in cm) is

$$C_{pipe} = k \, \frac{d^3}{l}, \tag{B.2}$$

The prefactor $k = 12.1 \text{ L s}^{-1} \text{ cm}^{-2}$ (at 293 K). One can adjust for the temperature by multiplying the conductance with $\sqrt{\frac{T}{293 \text{ K}}}$. For length $l = 60$ cm and diameter $d = 6.5$ cm, we have a conductance $C_{pipe} = 55$ L/s. If we extend our pipe a little, e.g. to the length $l = 65$ cm, we have $C_{pipe} = 51$ L/s conductance.

Since conductances in series add reciprocally,

$$C_{tot,series} = \frac{1}{C_1} + \frac{1}{C_2} + ... + \frac{1}{C_n}, \tag{B.3}$$

the titanium pipes are limiting for any (turbo) pump at their end with a pump speed higher than the titanium pipe conductance. We currently operate a 350 L/s turbopump (TURBOVAC 350 iX) at region D as well as another 350 L/s turbopump at region B (see Section 3.1). Conductances in parallel simply add,

$$C_{tot,parallel} = C_1 + C_2 + ... + C_n, \tag{B.4}$$

and since we have 2 titanium pipes attached to the glass tube, the total conductance the glass tube experiences is

$$C_{tot,glasstube} = 2 \times 53 \text{ L/s} = 106 \text{ L/s}. \tag{B.5}$$

With this pump configuration, the setup has reached a pressure $p = 1.5 \times 10^{-7}$ mbar in region B and $p = 5 \times 10^{-8}$ mbar in region D. With these pressures, no pressure dependence was observed in the signal S_B as well as S_D for BaF molecules, indicating the pressure is sufficient for consistent BaF transmission through the setup. This is in comparison to the observed pressure dependence of the BaF signal around $p = 10^{-6}$ mbar, indicating that the pressure is too high for reliable BaF transmission through the setup. This is analogous to the situation while we were probing for Ba atoms with 10 times higher pressure. Although there was no pressure dependence found of the Ba signal at $p = 10^{-6}$ mbar, we observed a pressure dependence at $p = 10^{-5}$ mbar. Measuring Ba atom and BaF molecule signals can thus be exploited to verify that the vacuum conditions in the interaction region satisfy the needs of the eEDM experiment.

C Magnetic shield specification from Sekels

This appendix contains all drawings of the magnetic shield, as well as the evaluation of the 5 μ-metal magnetic shield layers, as provided by Sekels [105]. The inner aluminium layer could be replaced with another material if aluminium were found at a later stage to interfere with the experiment.

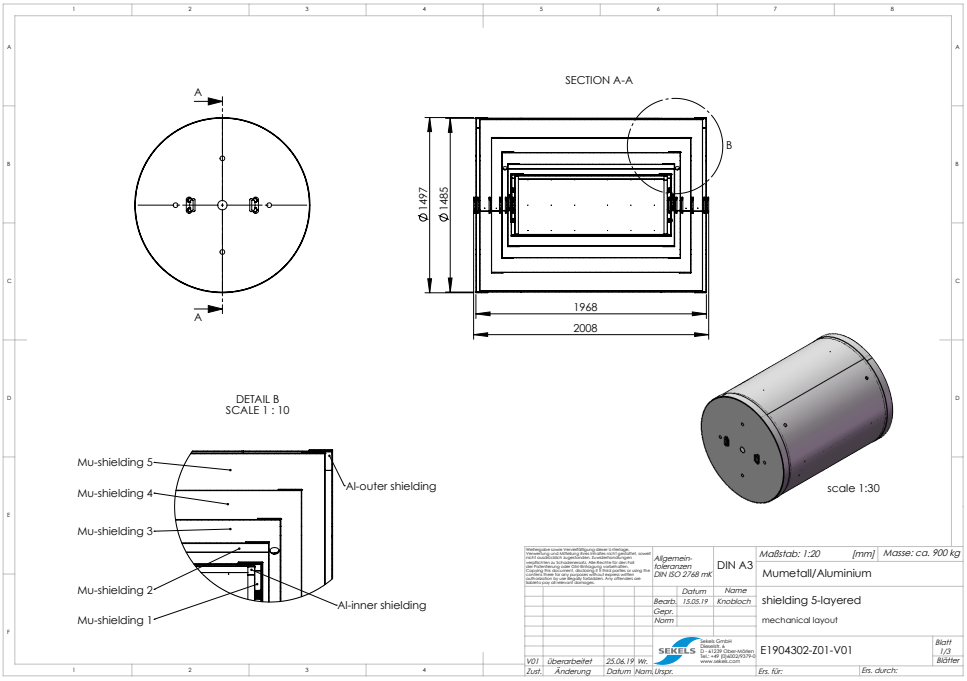
SECTION A-A
A
A
B
Ø 1497
Ø 1485
1968
2008
DETAIL B
SCALE 1 : 10
Mu-shielding 5
Mu-shielding 4
Mu-shielding 3
Mu-shielding 2
Mu-shielding 1
Al-outer shielding
Al-inner shielding
scale 1:30
Maßstab: 1:20 [mm] Masse: ca. 900 kg
DIN A3
Mumetall/Aluminium
shielding 5-layered
mechanical layout
E1904302-Z01-V01
Blatt 1/3 Blätter
V01 überarbeitet 25.06.19 Wr.
Änderung

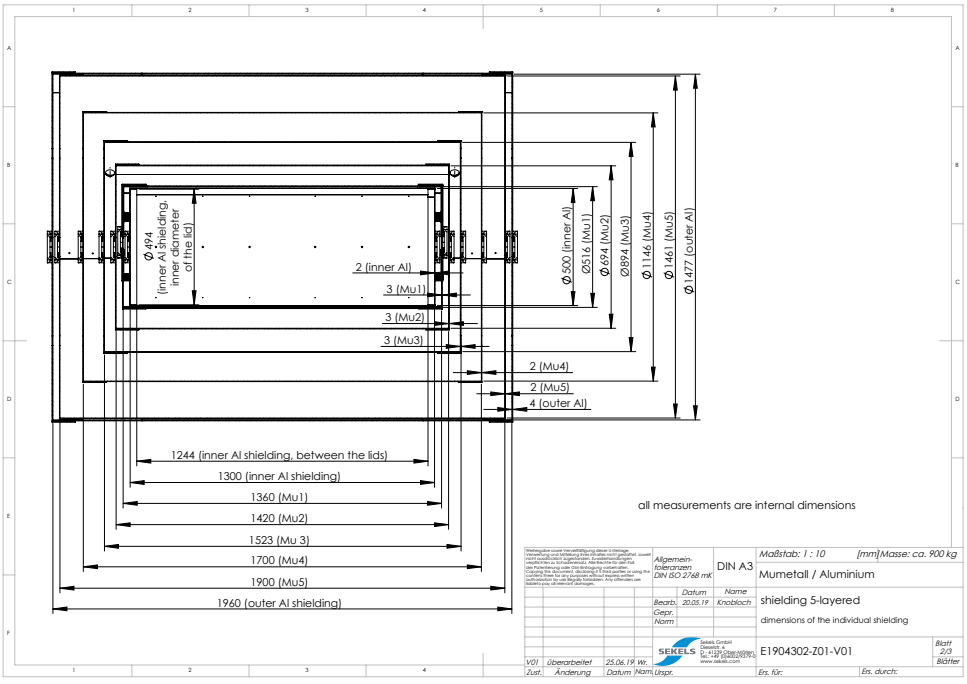
Ø 494
(inner Al shielding, inner diameter of the lid)
2 (inner Al)
3 (Mu1)
3 (Mu2)
3 (Mu3)
2 (Mu4)
2 (Mu5)
4 (outer Al)
Ø 500 (inner Al)
Ø516 (Mu1)
Ø 694 (Mu2)
Ø894 (Mu3)
Ø 1146 (Mu4)
Ø 1461 (Mu5)
Ø 1477 (outer Al)
1244 (inner Al shielding, between the lids)
1300 (inner Al shielding)
1360 (Mu1)
1420 (Mu2)
1523 (Mu 3)
1700 (Mu4)
1900 (Mu5)
1960 (outer Al shielding)
all measurements are internal dimensions
Maßstab: 1 : 10 [mm]Masse: ca. 900 kg
DIN A3
Mumetall / Aluminium
shielding 5-layered
dimensions of the individual shielding
E1904302-Z01-V01
Blatt 2/3 Blätter
V01 überarbeitet 25.06.19 Wr.
Änderung

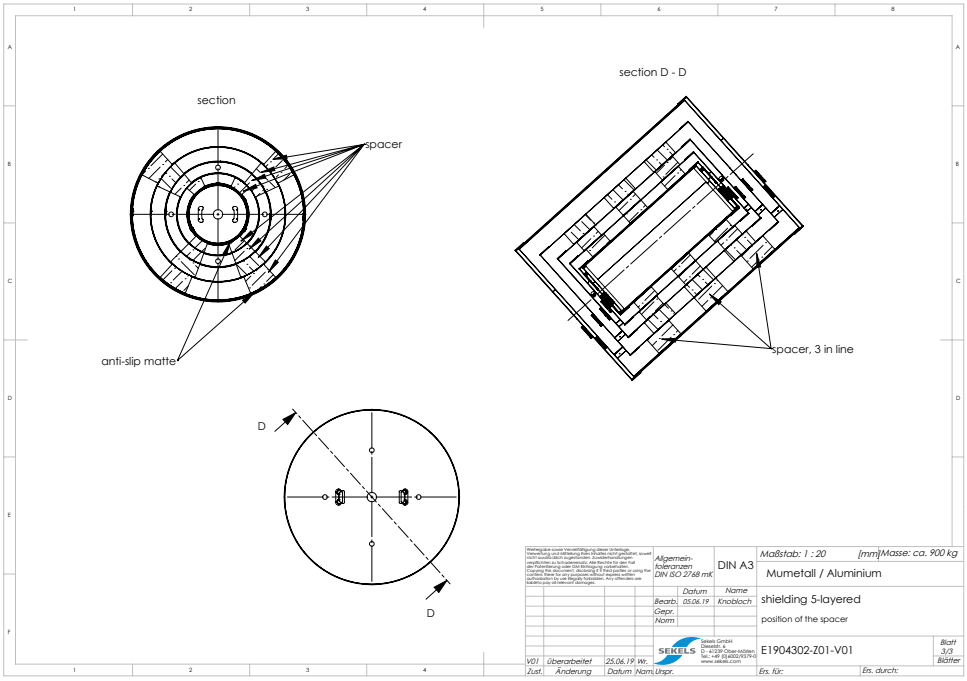
section
spacer
anti-slip matte
section D - D
spacer, 3 in line
D
D
DIN A3
Maßstab: 1 : 20
[mm] Masse: ca. 900 kg
Mumetall / Aluminium
shielding 5-layered
position of the spacer
E1904302-Z01-V01
Blatt 3/3
Blätter
SEKELS
Sekels GmbH
Datum
Name
05.06.19
Knobloch
25.06.19, Wr.

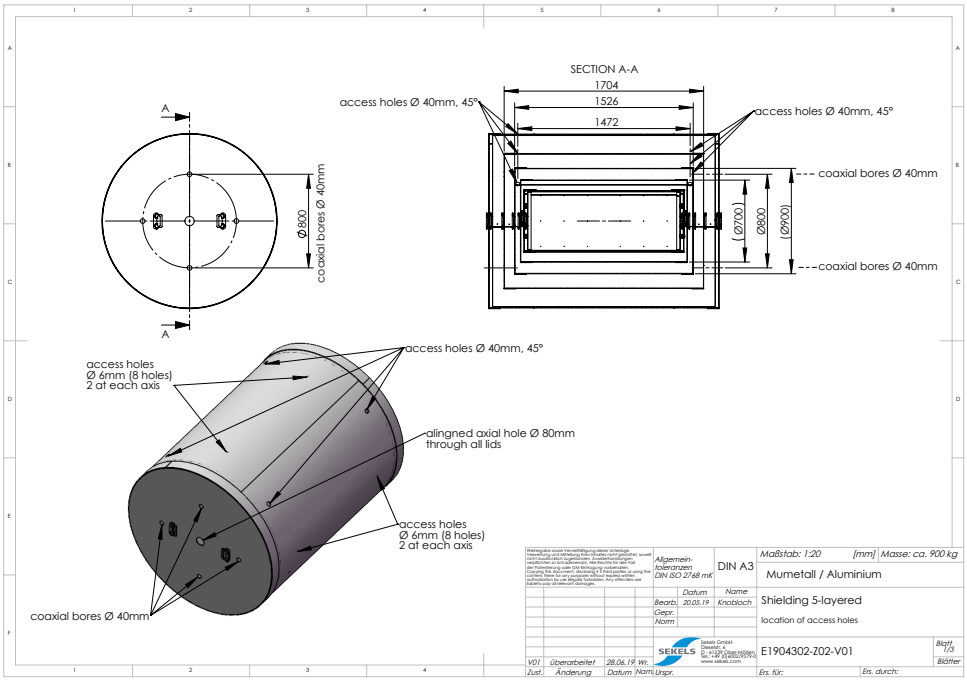
SECTION A-A
1704
1526
1472
access holes Ø 40mm, 45°
access holes Ø 40mm, 45°
coaxial bores Ø 40mm
coaxial bores Ø 40mm
(Ø700)
Ø800
(Ø900)
A
A
Ø 800
coaxial bores Ø 40mm
access holes Ø 40mm, 45°
access holes
Ø 6mm (8 holes)
2 at each axis
alingned axial hole Ø 80mm
through all lids
access holes
Ø 6mm (8 holes)
2 at each axis
coaxial bores Ø 40mm
DIN A3
Maßstab: 1:20
[mm] Masse: ca. 900 kg
Mumetall / Aluminium
Shielding 5-layered
location of access holes
E1904302-Z02-V01
Blatt 1/3
Blätter
SEKELS
Sekels GmbH
Datum
Name
20.05.19
Knobloch
28.06.19, Wr.

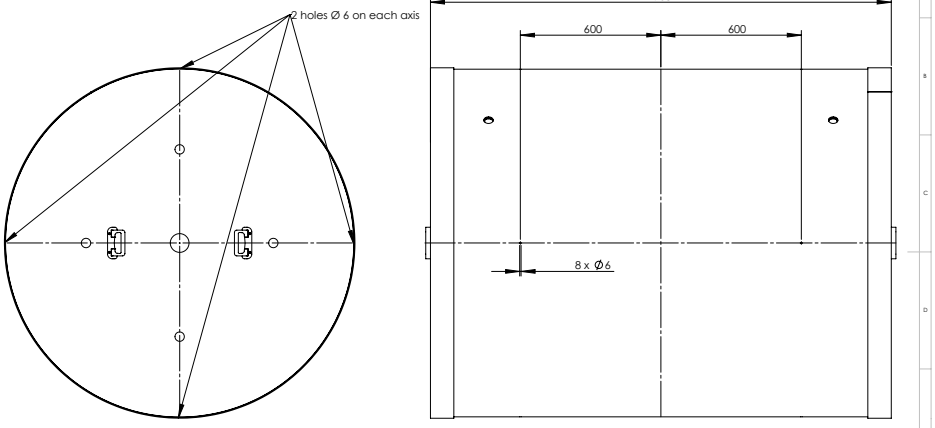

Allgemeintoleranzen DIN ISO 2768 mK				DIN A3	Maßstab: 1 : 1 [mm]	Masse: ca. x g	
					Mumetall / Aluminium		
			Datum	Name			
		Bearb.	04.07.19	Knobloch	Shielding 5-layered		
		Gepr.			location of holes Ø6 in the outer aluminium cylinder		
		Norm					
					E1904302-Z02-V01		Blatt 2/3 Blätter
Zust.	Änderung	Datum	Nam.	Urspr.	Ers. für:		Ers. durch:

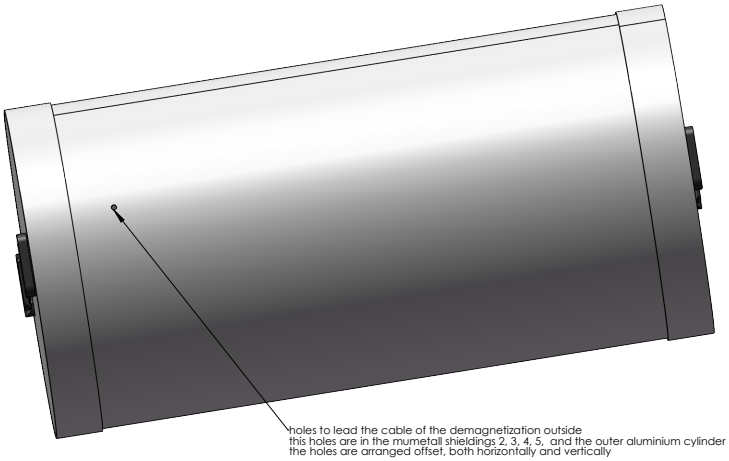

Allgemeintoleranzen DIN ISO 2768 mK				DIN A3	Maßstab: 1 : 5 [mm]	Masse: ca. 900 kg	
					Mumetall / Aluminium		
			Datum	Name			
		Bearb.	04.06.19	Knobloch	Shielding 5-layered		
		Gepr.			location of holes for the demagnetization		
		Norm					
					E1904302-Z02-V01		Blatt 3/3 Blätter
V01	überarbeitet	28.06.19	Wr.				
Zust.	Änderung	Datum	Nam.	Urspr.	Ers. für:		Ers. durch:

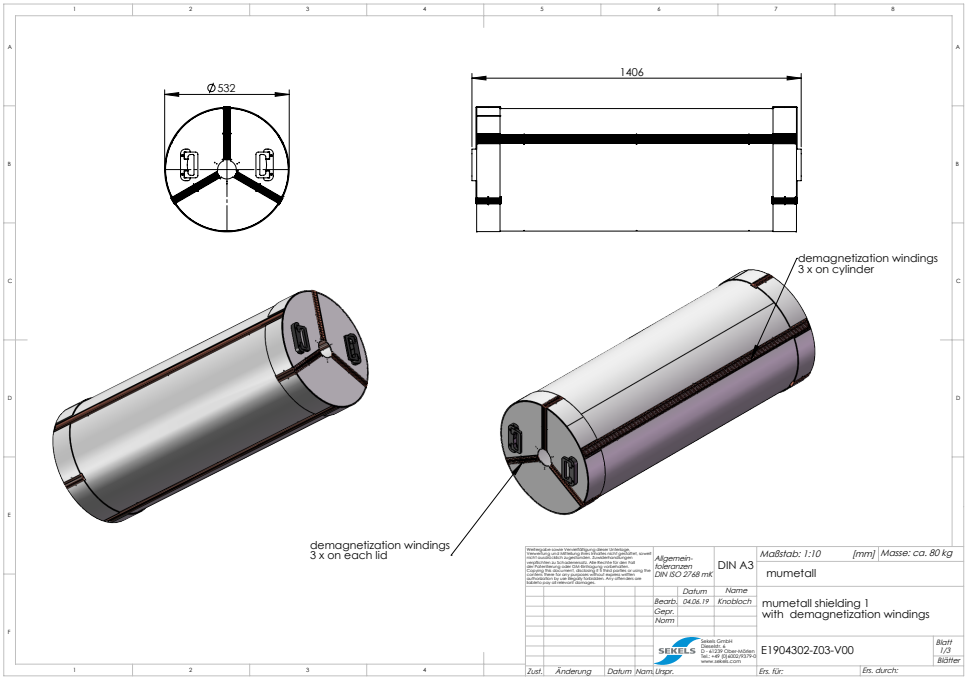
Ø 532
1406
demagnetization windings
3 x on cylinder
demagnetization windings
3 x on each lid
Allgemein-
toleranzen
DIN ISO 2768 mK
DIN A3
Maßstab: 1:10
[mm]
Masse: ca. 80 kg
mumetall
Datum
Name
Bearb.
04.06.19
Knobloch
Gepr.
Norm
mumetall shielding 1
with demagnetization windings
SEKELS
E1904302-Z03-V00
Blatt
1/3
Blätter
Änderung
Ers. für:
Ers. durch:

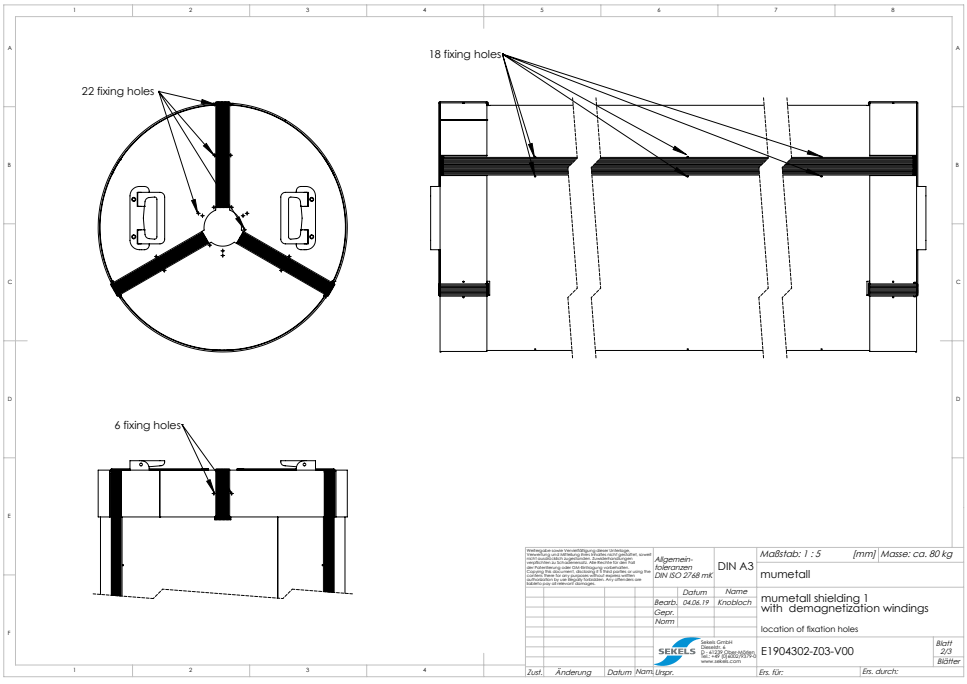
22 fixing holes
18 fixing holes
6 fixing holes
Allgemein-
toleranzen
DIN ISO 2768 mK
DIN A3
Maßstab: 1 :5
[mm]
Masse: ca. 80 kg
mumetall
Datum
Name
Bearb.
04.06.19
Knobloch
Gepr.
Norm
mumetall shielding 1
with demagnetization windings
location of fixation holes
SEKELS
E1904302-Z03-V00
Blatt
2/3
Blätter
Änderung
Ers. für:
Ers. durch:

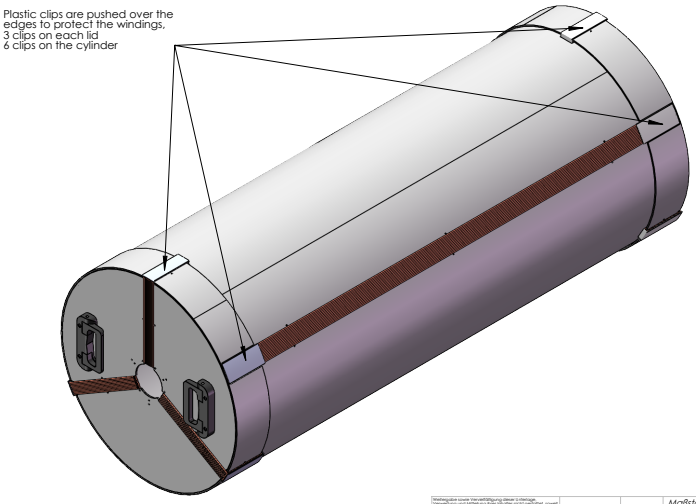

Allgemeintoleranzen DIN ISO 2768 mK	DIN A3	Maßstab: 1 : 5	[mm]	Masse: ca. 80 kg	
		mumetall			
	Datum	Name	mumetall shielding 1 with demagnetization windings		
Bearb.	05.06.19	Knobloch			
Gepr.			location of plastic clips		
Norm					
SEKELS	Sekels GmbH D-66386 St. Ingbert		E190403-Z03-V00		Blatt 3/9
	Tel. +49 (0)6894/9579-0 www.sekels.com				Blätter

Zust. | Änderung | Datum | Norm. | Urspr. | Ers. für: | Ers. durch:

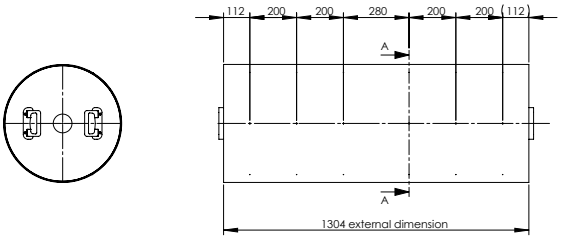

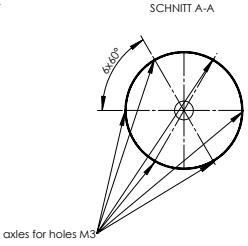

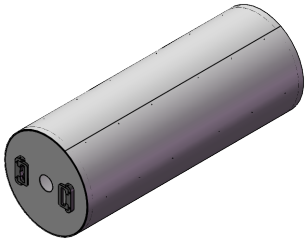

Allgemeintoleranzen DIN ISO 2768 mK	DIN A3	Maßstab: 1:10	[mm]	Masse: ca. 14 kg	
		Aluminium			
	Datum	Name	Shielding 5-layered		
Bearb.	04.07.19	Knobloch			
Gepr.			inner aluminium cylinder, complete components		
Norm					
SEKELS	Sekels GmbH D-66386 St. Ingbert		E1904302-Z04-V01		Blatt 1/1
	Tel. +49 (0)6894/9579-0 www.sekels.com				Blätter

Zust. | Änderung | Datum | Norm. | Urspr. | Ers. für: | Ers. durch:

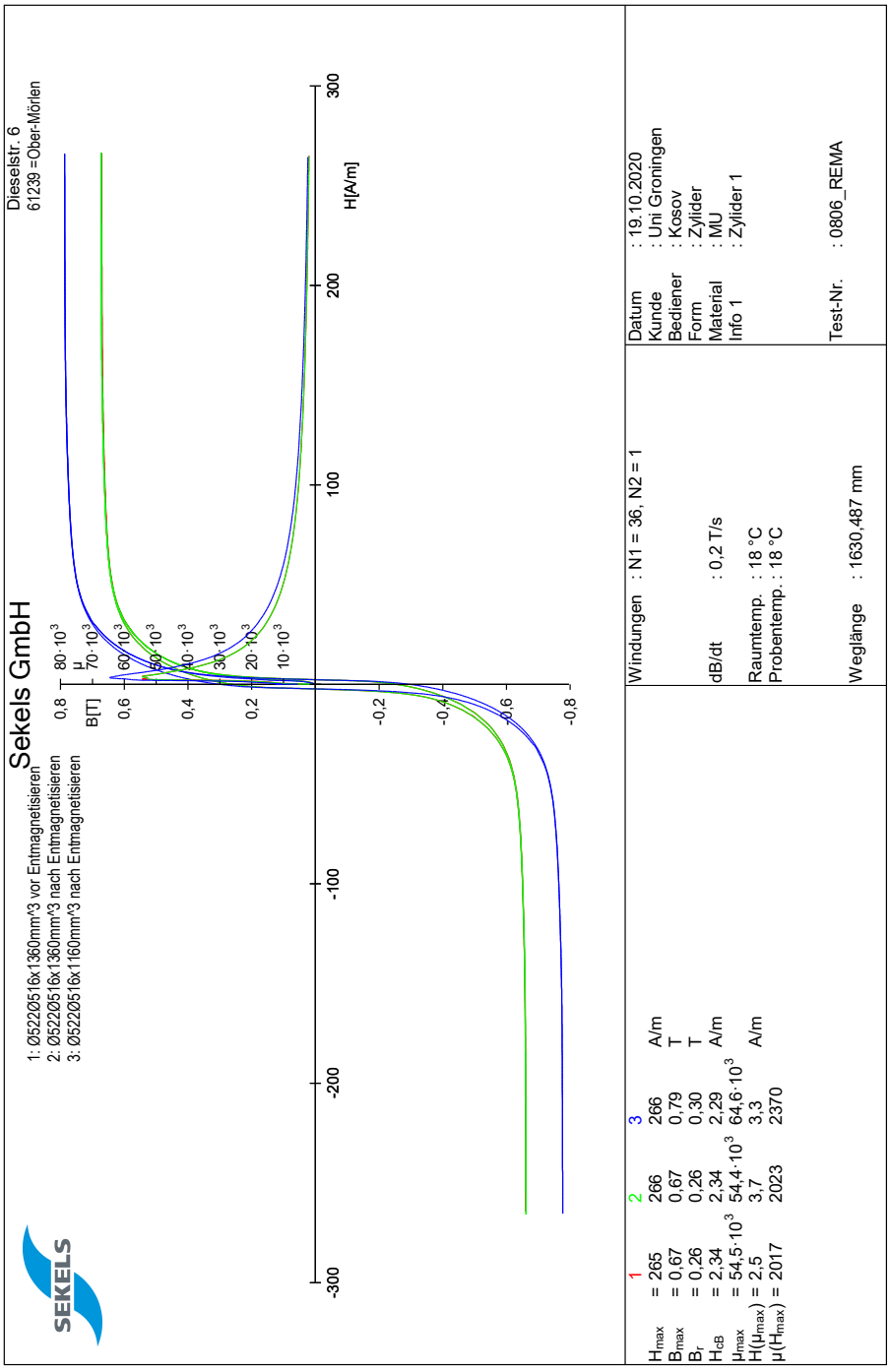

	1	2	3	
H_{max}	= 265	266	266	A/m
B_{max}	= 0,67	0,67	0,79	T
B_r	= 0,26	0,26	0,30	T
H_{cB}	= 2,34	2,34	2,29	A/m
μ_{max}	= $54,5 \cdot 10^3$	$54,4 \cdot 10^3$	$64,6 \cdot 10^3$	
$H(\mu_{max})$	= 2,5	3,7	3,3	A/m
$\mu(H_{max})$	= 2017	2023	2370	

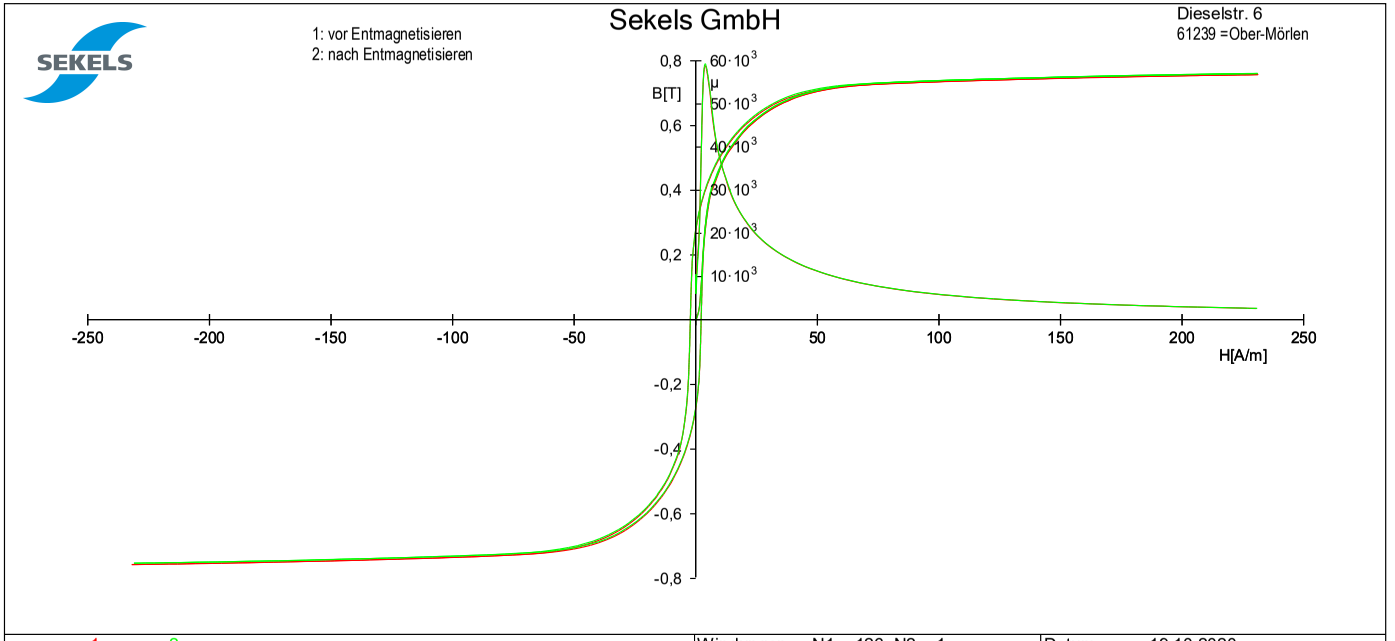

	1	2	
H_{max}	= 231	231	A/m
B_{max}	= 0,76	0,76	T
B_r	= 2,23	2,22	A/m
H_{cB}	= 58,9·10^3	59,3·10^3	
μ_{max}	= 4,0	3,8	A/m
$H(\mu_{max})$	= 2616	2623	
$\mu(H_{max})$			

Windungen	: N1 = 126, N2 = 1
dB/dt	: 0,2 T/s
Raumtemp.	: 20 °C
Probentemp.	: 20 °C
Weglänge	: 2189,69 mm
Fläche	: 4260 mm²

Datum	: 19.10.2020
Kunde	: Uni Groningen
Bediener	: Kosov
Form	: Zylider
Material	: MU
Info 1	: Ø700Ø694x1420mm^3
Info 2	: Zylider 2
Test-Nr.	: 0806_REMA

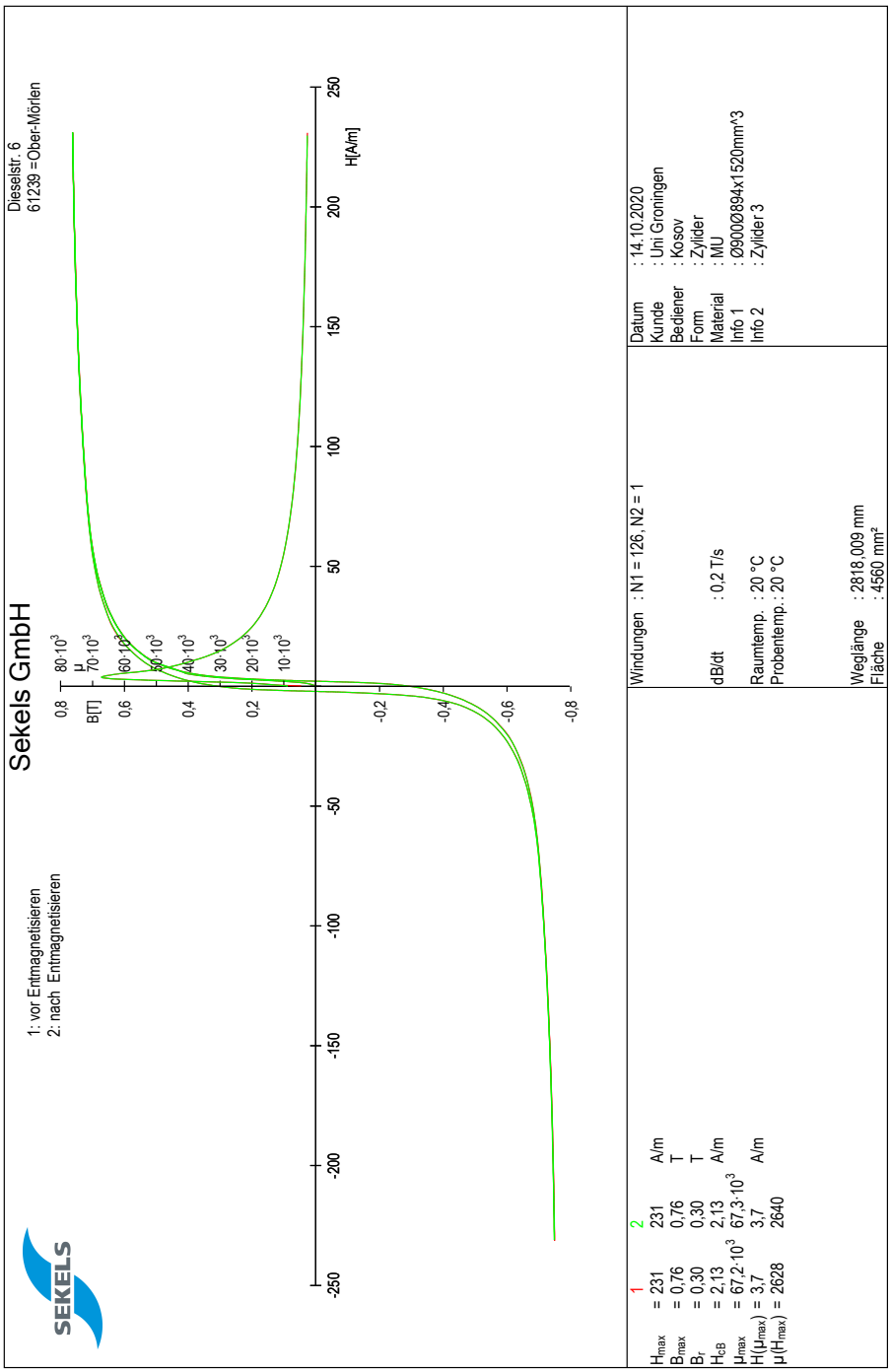
Sekels GmbH
Dieselstr. 6
61239 =Ober-Mörlen
1: vor Entmagnetisieren
2: nach Entmagnetisieren
B[T]
H[A/m]
μ
80·10³
70·10³
60·10³
50·10³
40·10³
30·10³
20·10³
10·10³
0,8
0,6
0,4
0,2
-0,2
-0,4
-0,6
-0,8
-250
-200
-150
-100
-50
50
100
150
200
250
Windungen : N1 = 126, N2 = 1
dB/dt : 0,2 T/s
Raumtemp. : 20 °C
Probentemp. : 20 °C
Weglänge : 2818,009 mm
Fläche : 4560 mm²
Datum : 14.10.2020
Kunde : Uni Groningen
Bediener : Kosov
Form : Zylider
Material : MU
Info 1 : Ø900Ø894x1520mm^3
Info 2 : Zylider 3
1 2
Hmax = 231 231 A/m
Bmax = 0,76 0,76 T
Br = 0,30 0,30 T
HcB = 2,13 2,13 A/m
μmax = 67,2·10³ 67,3·10³
H(μmax) = 3,7 3,7 A/m
μ(Hmax) = 2628 2640

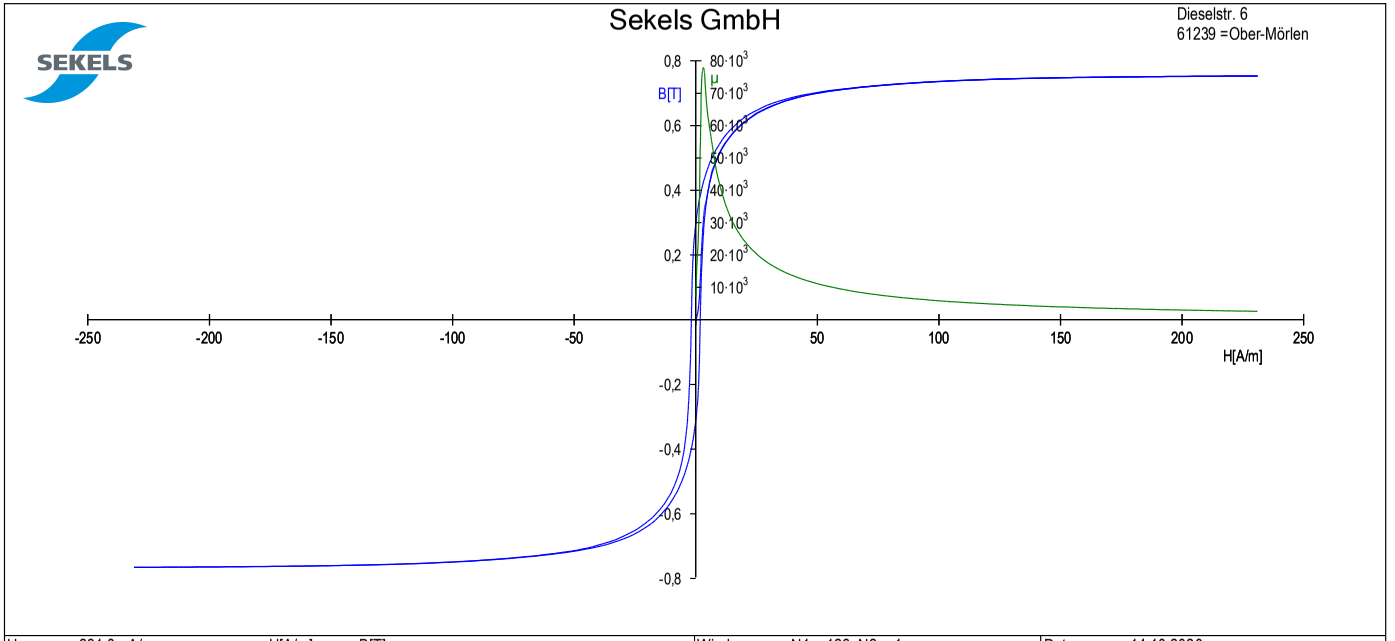

H_{max}	= 231,0	A/m	H[A/m]	B[T]	μ	Windungen	: N1 = 126, N2 = 1	Datum : 14.10.2020
J_{max}	= 0,753	T	2	0,151	$60{,}2 \cdot 10^3$			Kunde : Uni Groningen
B_{max}	= 0,753	T	50	0,700	$11{,}1 \cdot 10^3$			Bediener : Kosov
B_r	= 0,304	T	200	0,752	2992			Form : Zylinder
H_{cB}	= 1,82	A/m				dB/dt	: 0,2 T/s	Material : MU
μ_{max}	= $77{,}89 \cdot 10^3$							Info 1 : Ø1150Ø1146x1700mm^3
$H(\mu_{max})$	= 3,13	A/m				Raumtemp.	: 20 °C	Info 2 : Zylinder 4
$\mu(H_{max})$	= 2595					Probentemp.	: 20 °C	Info 3 : nach Entmagnetisieren
W	= 4,5	J/m³						
						Weglänge	: 3606,548 mm	
						Fläche	: 3400 mm²	

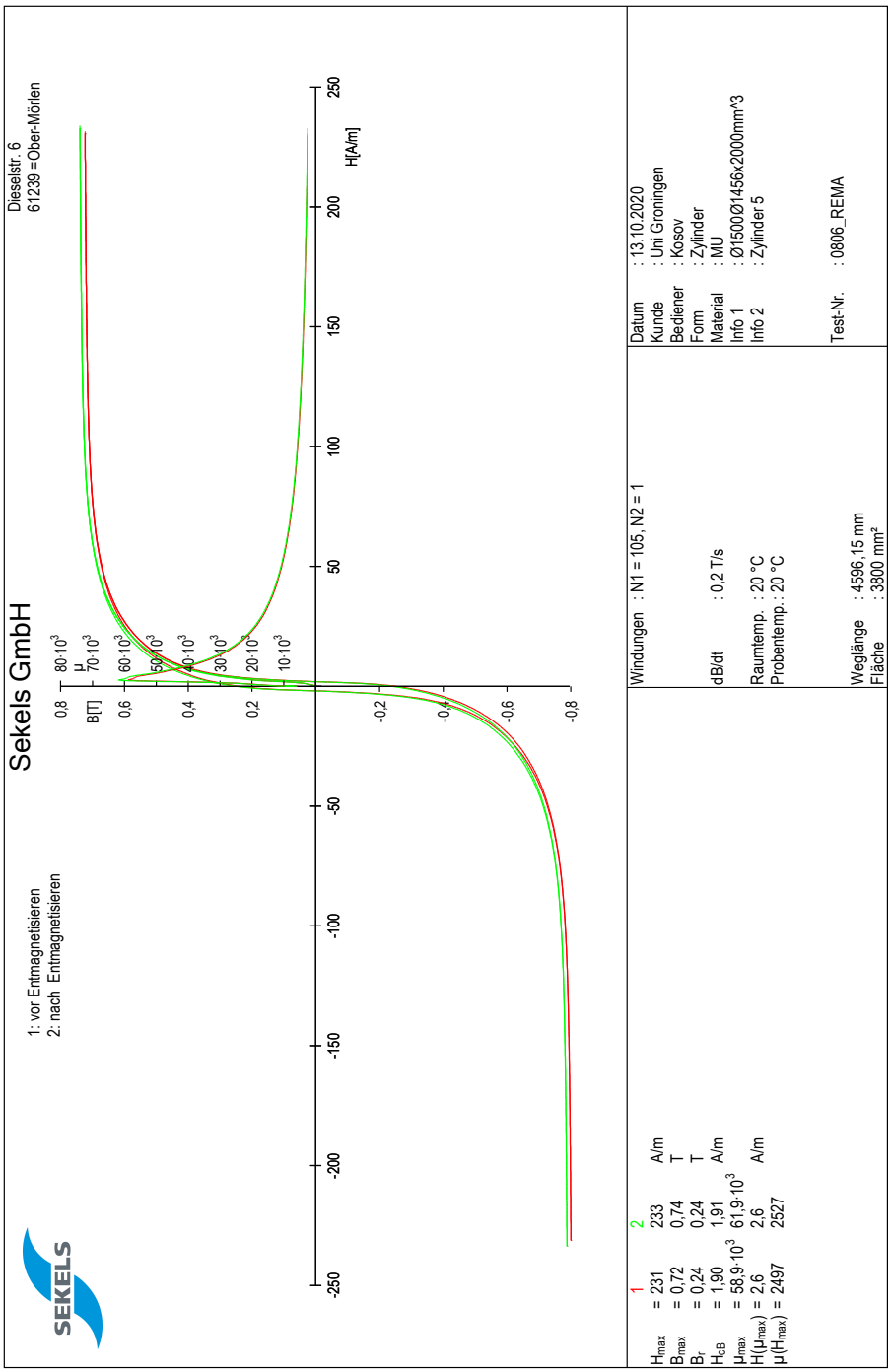

	1	2	
H_{max}	= 231	233	A/m
B_{max}	= 0,72	0,74	T
B_r	= 0,24	0,24	T
H_{cB}	= 1,90	1,91	A/m
μ_{max}	= $58,9 \cdot 10^3$	$61,9 \cdot 10^3$	
$H(\mu_{max})$	= 2,6	2,6	A/m
$\mu(H_{max})$	= 2497	2527	

D ITO-coated glass plates for electric field generation

For electric field generation inside the interaction zone, we use Indium Tin Oxide (ITO) coated soda lime float glass with an Anti Reflection (AR) coating (see Fig. D.1). The ITO coating, which is applied to one side, has a surface resistance of $300\ \Omega/\mathrm{Sq}$. The AR coating, which is applied to the other side, results in 1% reflection at 860 nm.

The glass plates are spaced at 40 mm with 0.05 mm tolerance, using macor pieces (see Fig. D.2) arranged on a flat surface (see Fig. D.3). The macor pieces (see Fig. D.2) contain arrangements for an additional field plate centered between the already existing plates. All this is connected with a frame consisting of Fig. D.4, Fig. D.5, and rods. The rods used for assembly were selected from a larger number of rods, for curvature below what was necessary. The parts are assembled by applying vacuum compatible glue to the outside of the glass plates and the macor pieces, so as to preserve the distances. The glue is STYCAST 2850FT mixed with catalyst 9 for appropriate viscosity for syringe injection into holes.

Teflon-coated HV compatible cables are connected to the ITO coated glass plates using vacuum compatible electrically conductive silver-filled epoxy paste EPO-TEK® EJ2189. The resistance of one of the plates is $17.7\ \mathrm{k}\Omega$. The other plate has a similar resistance. The result is in Fig. 3.16.

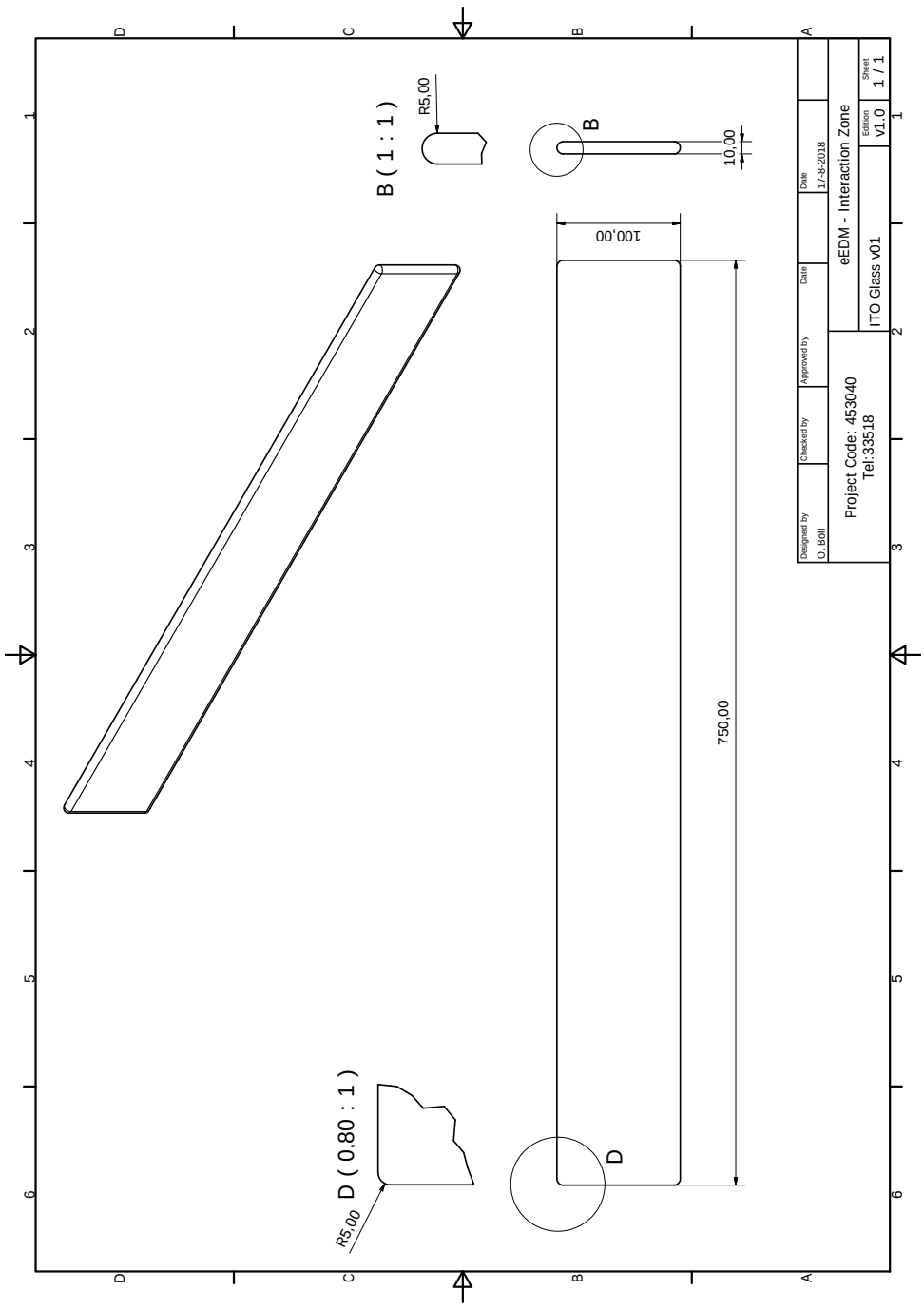

Figure D.1: Drawings of ITO coated glass plates.

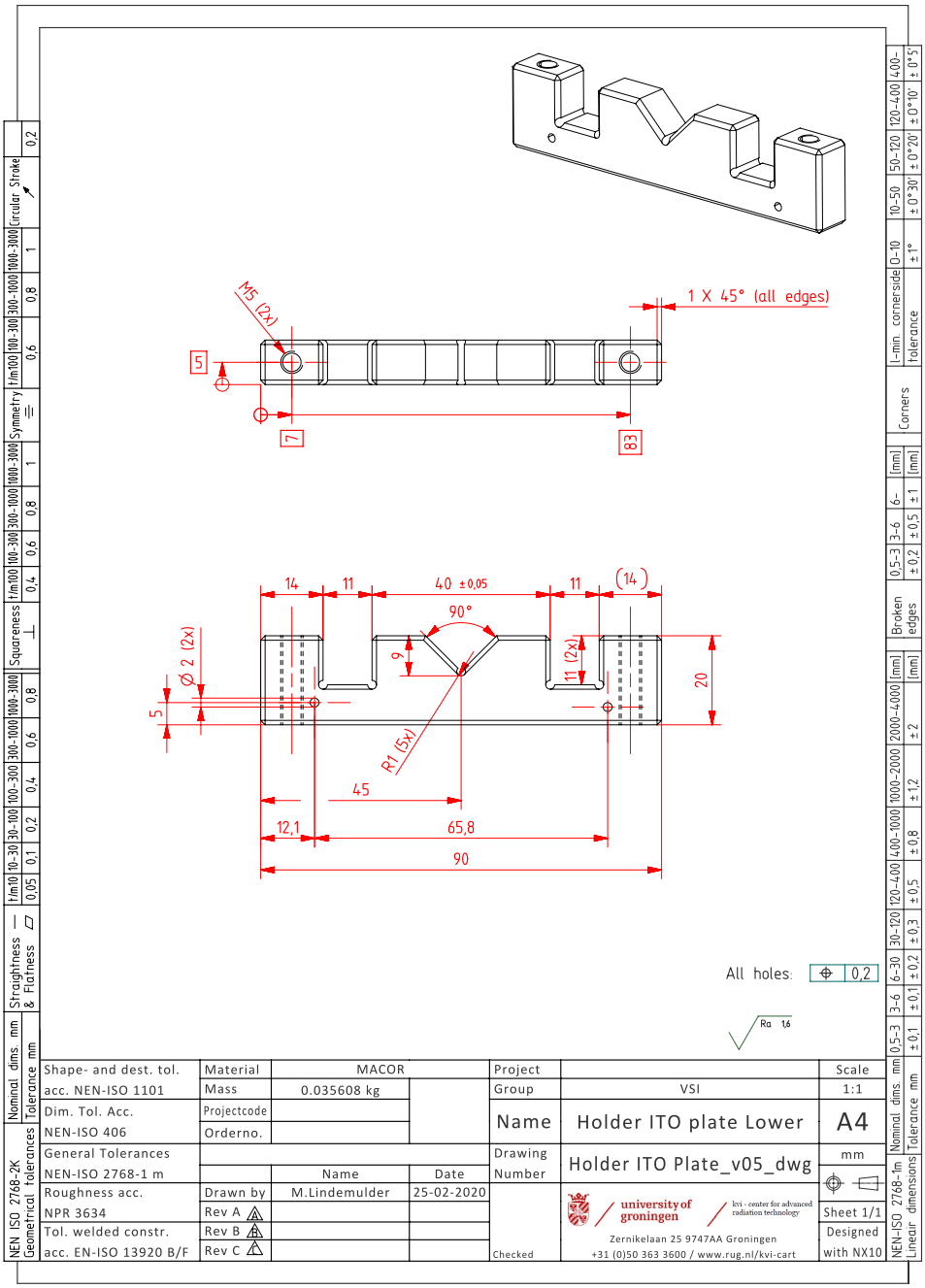

Figure D.2: Drawings of Macor ITO plate holder.

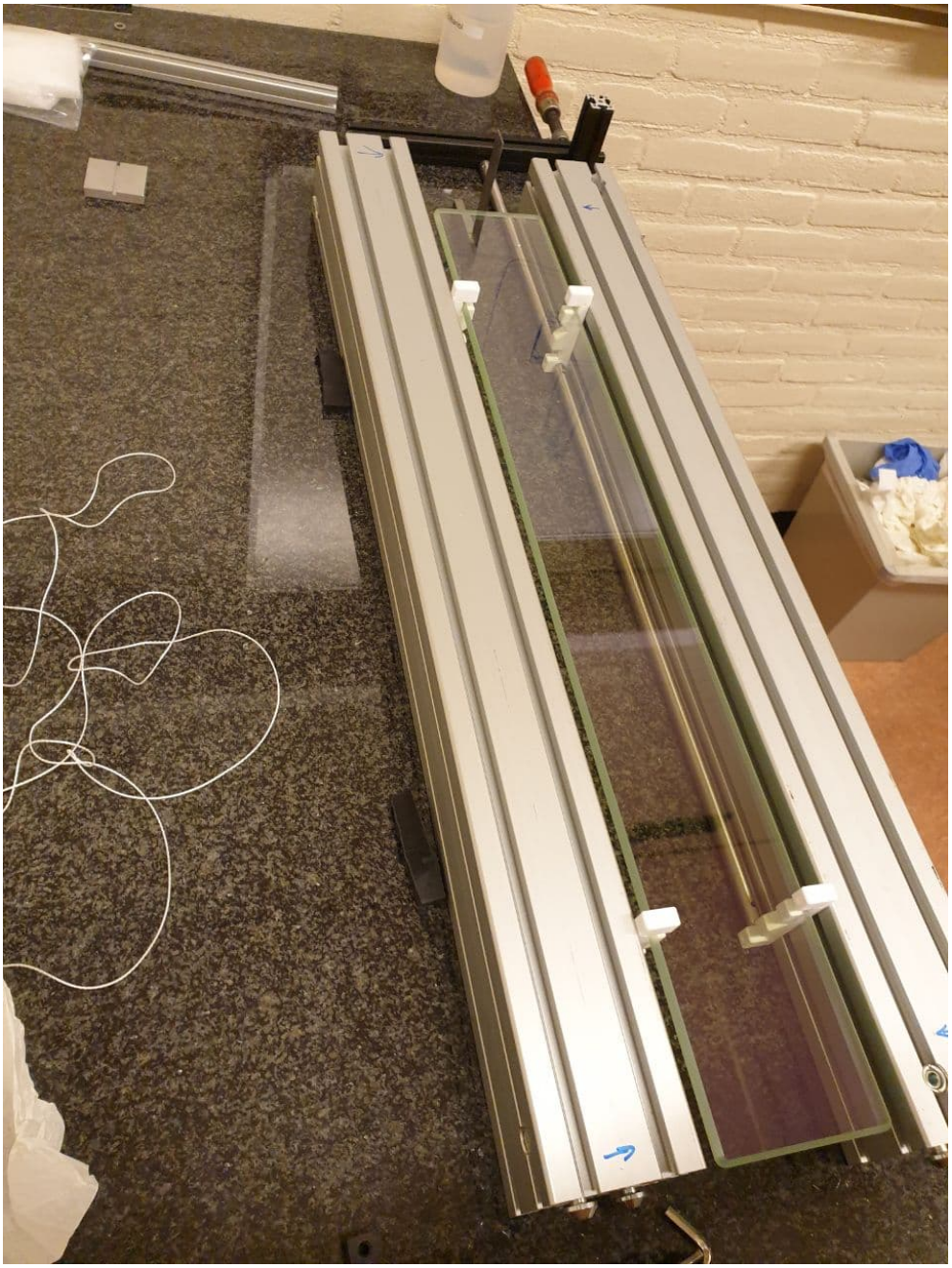

Figure D.3: Picture showing methods used for alignment: postholders in a Boikon frame, fixed on top of a polished granite table.

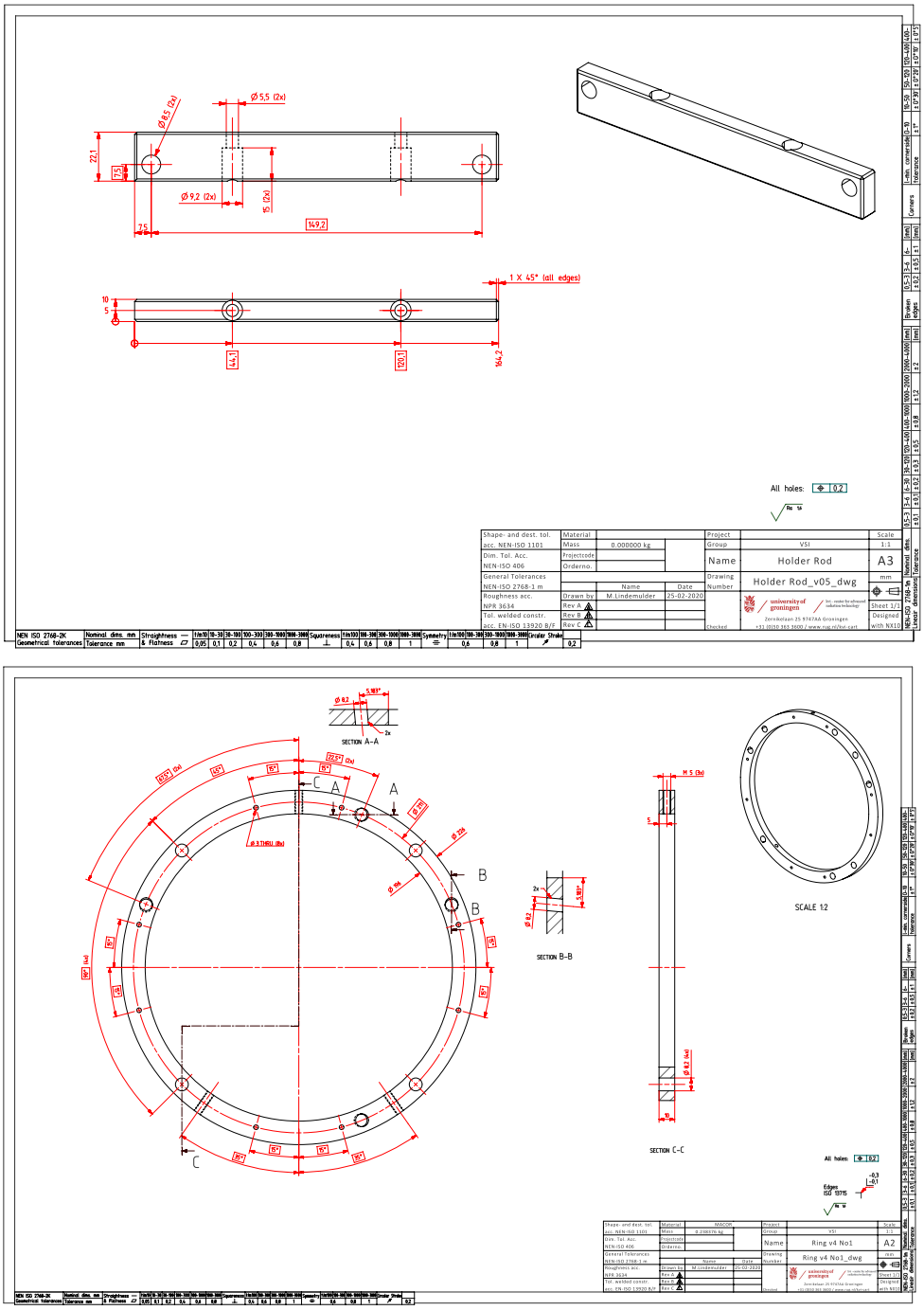

Figure D.4: Drawings of Macor ITO plate holder rod and ring No1.

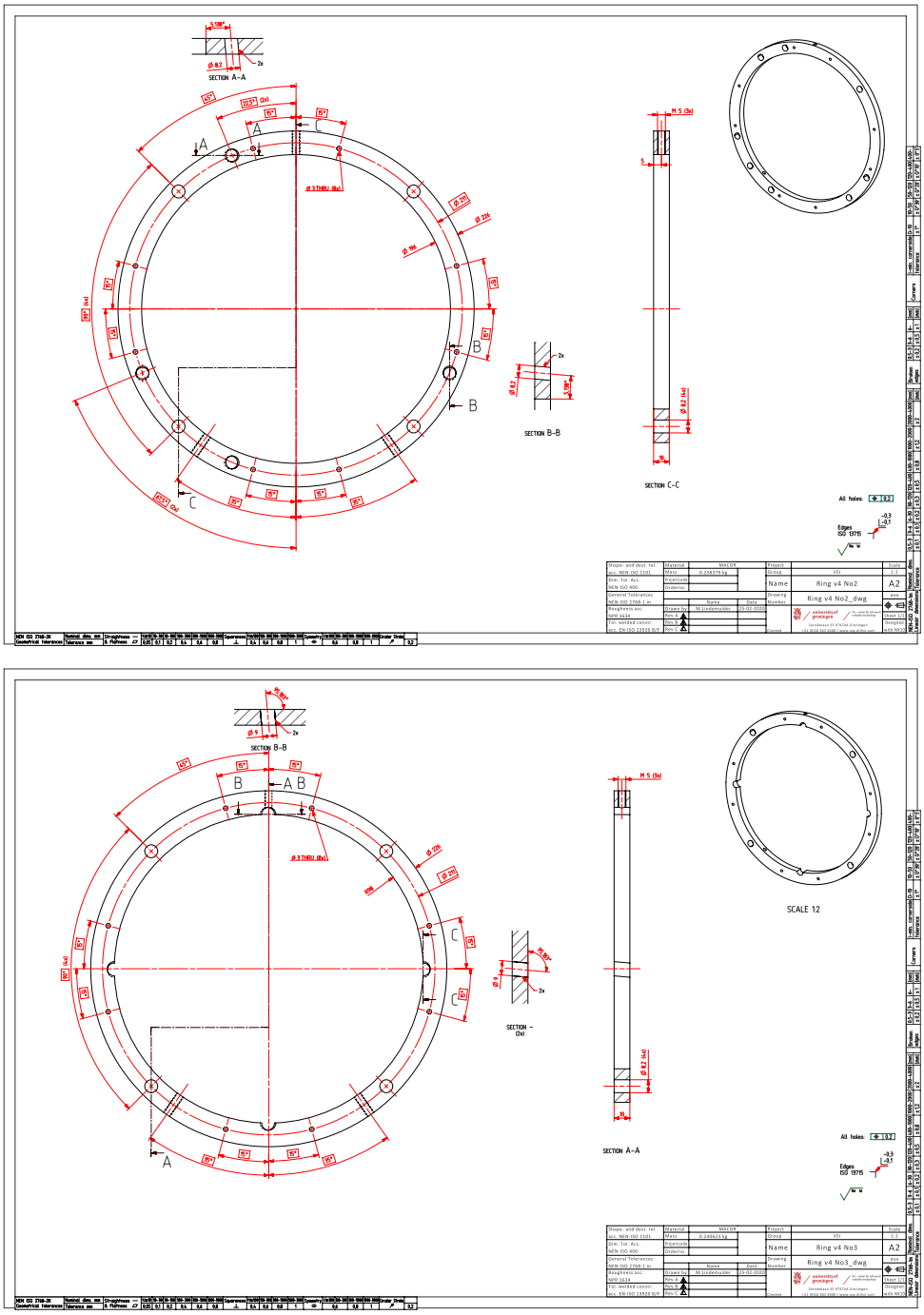

Figure D.5: Drawings of Macor ring No2 and ring No3.

E Electric field reversal box

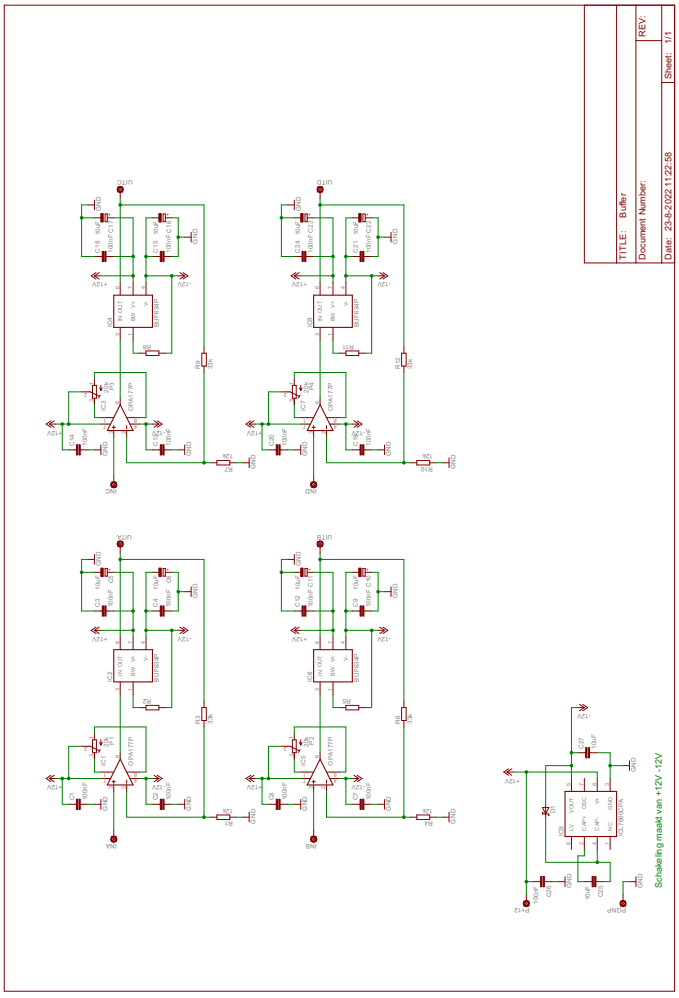

Figure E.1: Buffers for monitoring schema.

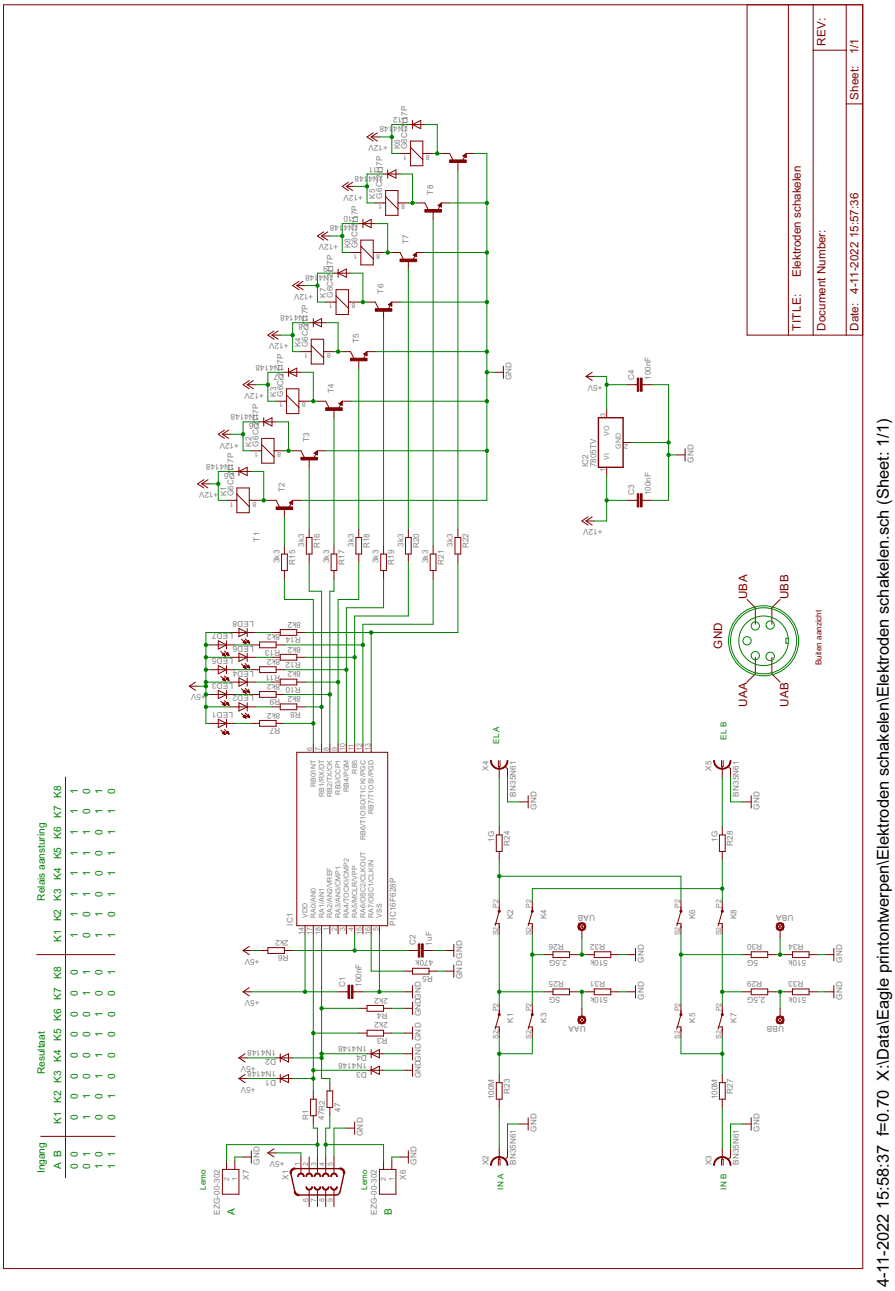

Figure E.2: Electric field reversal box schema.

F A note on airpads

The safe and shock-free movement of sensitive heavy equipment was performed with airpads. The implementation, while not critical to the measurement itself, is important to this end. Here is a description of the specifications and considerations for using airpads in this particular experiment. We used it to move the interaction zone magnetic shield with frame (region C in Fig. 3.1), as well as the detection zone with frame (region D in Fig. 3.1), with all but the most sensitive the equipment installed.

We decided to go for 4 airpads that can carry 500 kg each (Aerofilm, Polyurethaan Air caster 300 mm Standaard Capaciteit/Polyurethane Air caster 300 mm standard Capacity). A balanced configuration requires at least 3 airpads.

For moving the magnetic shield with its frame, which weighs a total of about 1000 kg, all 4 airpads are needed to insure stability. The detection zone weighs at most 200 kg in the end, so the minimum of 3 airpads would suffice.

There are some obstacles in the lab, such as the external compensation coils (see Section 3.3). These coils span from the laboratory floor to 5 cm above the floor. They are adjustable down to 2.5 cm above the floor. This barrier has to be traversed if you want to install the frames of the magnetic shield and detection zone within or across these Helmholtz coils.

G Flux Gates

We use FLC3-70 Stefan Meyer flux gate sensors, which provide for measuring 3 orthogonal axes [115]. Of the 9 flux gate sensors available for measurements, 8 can be used simultaneously. The flux gate sensors are connected through a non-magnetic RJ45 connection to a custom NIM crate box, which does both power supply and readout[i]. Power supply is through NIM crate +12 V and -12 V rails that feed into L7805 and L7905 voltage regulators, that form +5 V and -5 V rails respectively (200 mV tolerance). With some Zener diodes it is unlikely that the total supply voltage exceeds 12 V[ii]. Readout of the flux gate sensor voltages is output by the custom NIM crate box via SMA ports. These voltages are converted to frequency, digitized, with Voltage to Frequency Converters (VFC). The resulting frequency is counted with a VME crate mounted scaler counter (SIS3820). These are converted to magnetic fields in the DAQ by calibration of the previously mentioned electronics.

For reaching nT or better sensitivity, we found three factors most important. The first factor is power supply, which in our case is through voltage regulators, and these only work stable to a few mV if they get a sufficiently high input voltage. The second factor is the calibration of electronics, and in particular of the VFC offset frequency at 0 V, in combination with a calibration of the flux gate voltage at no magnetic field. With regular calibration, nT drifts in offsets due to temperature can be taken into account. The third factor is a stable room temperature. With sufficient air-conditioning such that temperature changes are $1\ ^{\circ}\mathrm{C}$ or less, better than $1\ \mathrm{nT}$ resolution measurements with flux gate sensors are viable.

The resulting field is measured over time (see Fig. G.1). From this the stability can be shown in the form of an Allan variance [117] diagram (see Fig. G.2).

[i] RJ45 connector on flux gate side, RJ45 port on NIM crate box side.

[ii] It can handle a total supply voltage of 12 V, above 12 V the flux gate electronics will be fried.

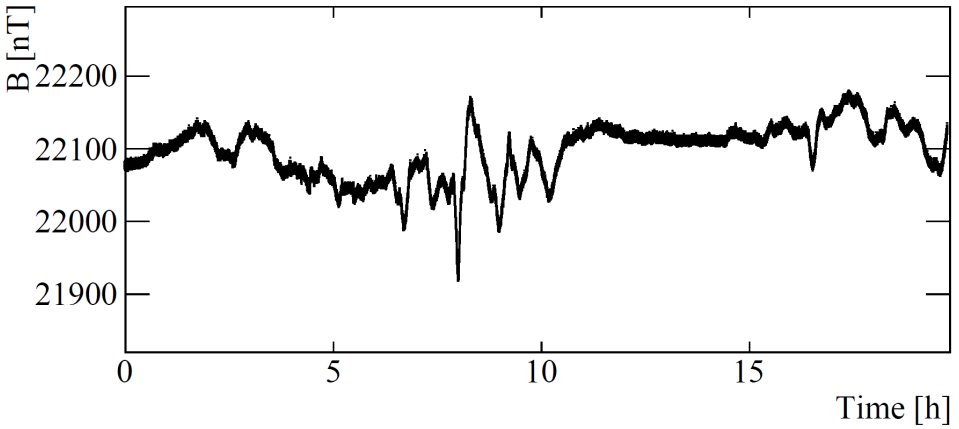

Figure G.1: Magnetic field measurement over 20 hours performed employing one of the 4 flux gates (FG02 in the laboratory) positioned around the magnetic shield at around BaF beam height for constant monitoring. The laboratory magnetic field magnitude is $B \approx 22\ \mu\mathrm{T}$.

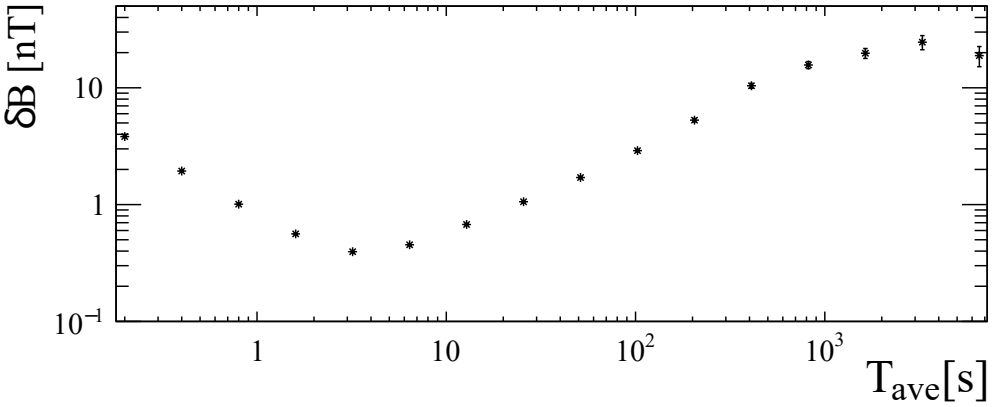

Figure G.2: Allan variance δB plotted as a function of averaging time T_{ave}. Derived from the measurement in Fig. G.2. The Allan variance decreases down to below nT level for $T_{ave} = 3$ s. Drifts over the 20 hour measurement lead to a maximum Allan variance $\delta B \approx 25$ nT.

H Magnetic field maps of the interaction zone employing flux gates

Four sets of two maps of the magnetic field where made, one set before degaussing, one set after high current degaussing, one set after low current degaussing. The fourth set was more detailed, recorded 2 days later than the other 3 sets, so as to let the magnetic field settle. Degaussing is performed by a Keysight 33500B Waveform Generator, providing a factory configured arbitrary waveform DEMAG_HC.arb (DEMAG_HF.arb is also available, but not used). The waveform is input into a Toellner TOE 7621 4-quadrant power supply. High current degaussing concerns setting the 4-quadrant power supply to ± 5 V current source input sensitivity. Low current degaussing concerns setting the 4-quadrant power supply to ± 10 V current source input sensitivity.

Each set contains a measurement in the FG In state and a measurement in the FG Out state (Fig. 4.4 and Fig. 4.5). The first set, Fig. H.1 and Fig. H.2, where measured before a degaussing of the inner magnetic shield layer. The second set, Fig. H.3 and Fig. H.4, where measured after a high current degaussing of the inner magnetic shield layer. The third set, Fig. H.5 and Fig. H.6, where measured after a low current degaussing of the inner magnetic shield layer.

The fourth more detailed measurement set is shown in Fig. H.7 and Fig. H.8, summarized in Table 4.2 and Table 4.3.

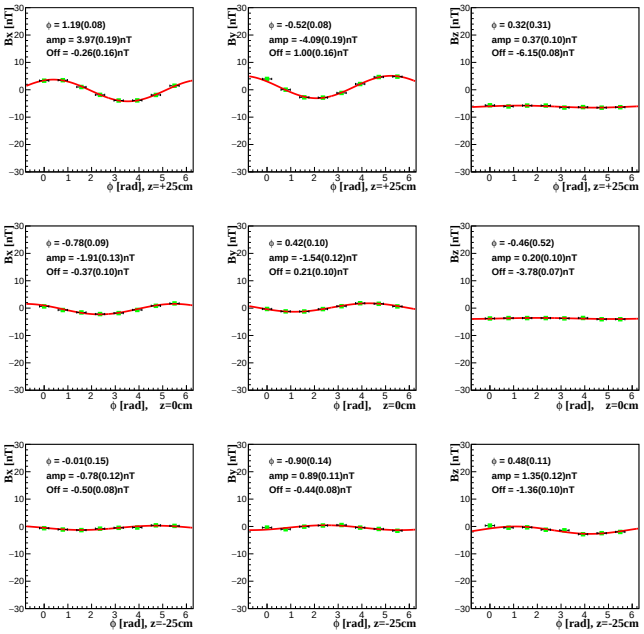

Figure H.1: Before degaussing. Map of magnetic field (2021-06-02) inside magnetic shield, with the flux gate in the FG In state.

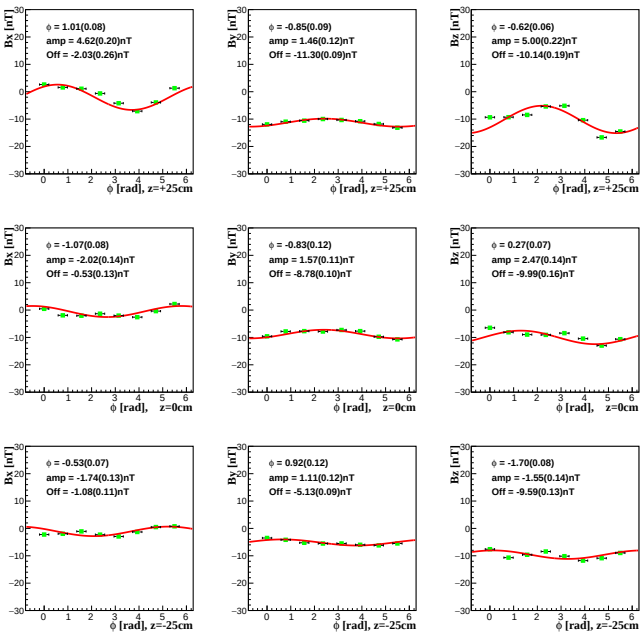

Figure H.2: Before degaussing. Map of magnetic field (2021-06-02) inside magnetic shield, with the flux gate in the FG Out state.

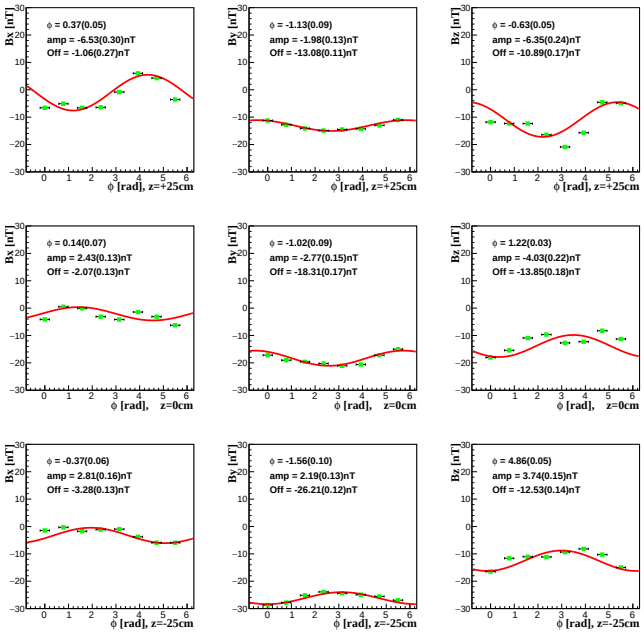

Figure H.3: After high current degaussing. Map of magnetic field (2021-06-02) inside magnetic shield, with the flux gate in the FG In state.

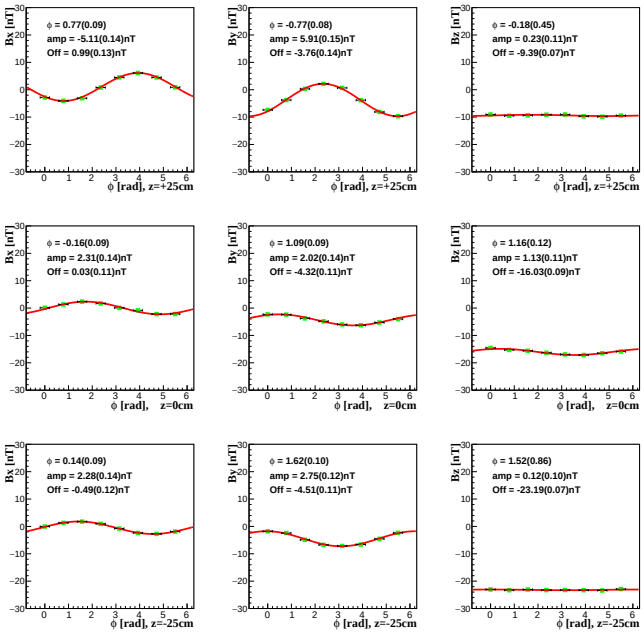

Figure H.4: After high current degaussing. Map of magnetic field (2021-06-02) inside magnetic shield, with the flux gate in the FG Out state.

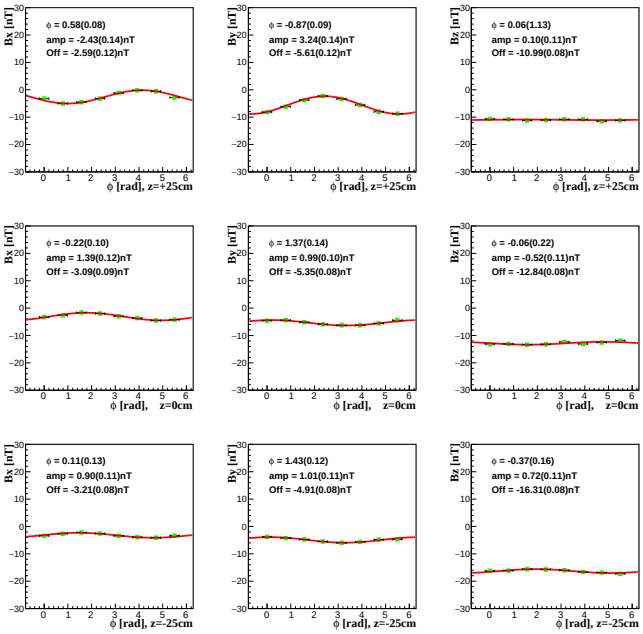

Figure H.5: After low current degaussing. Map of magnetic field (2021-06-02) inside magnetic shield, with the flux gate in the FG In state.

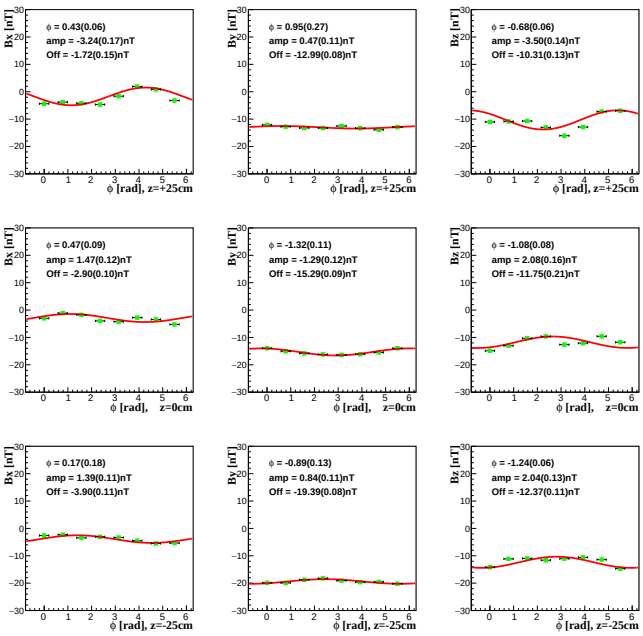

Figure H.6: After low current degaussing. Map of magnetic field (2021-06-02) inside magnetic shield, with the flux gate in the FG Out state.

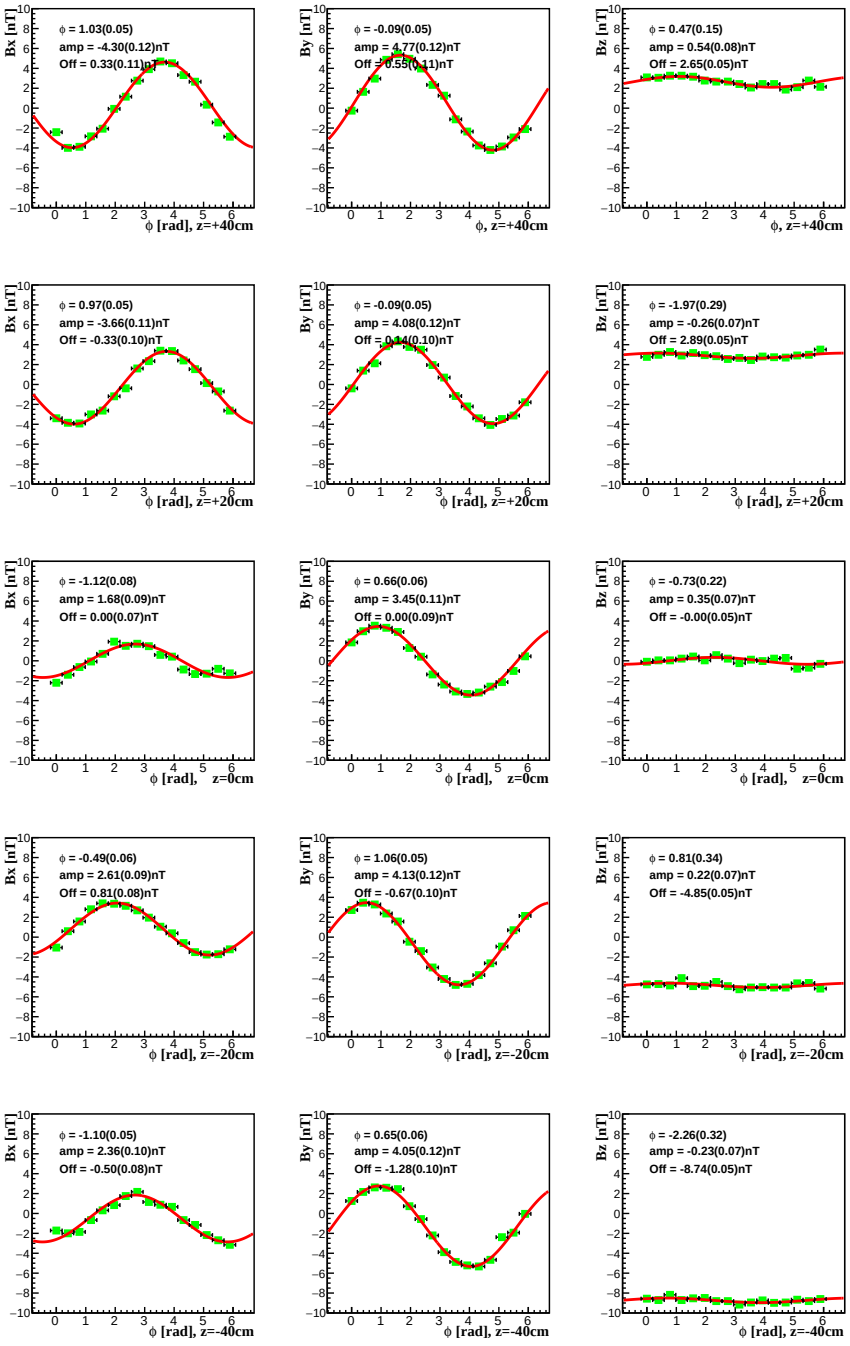

Figure H.7: Map of magnetic field (2021-06-04) inside magnetic shield, with the flux gate in the FG In state, rotating at one point at a time. Each point is at a location z with respect to the center of the magnetic shield.

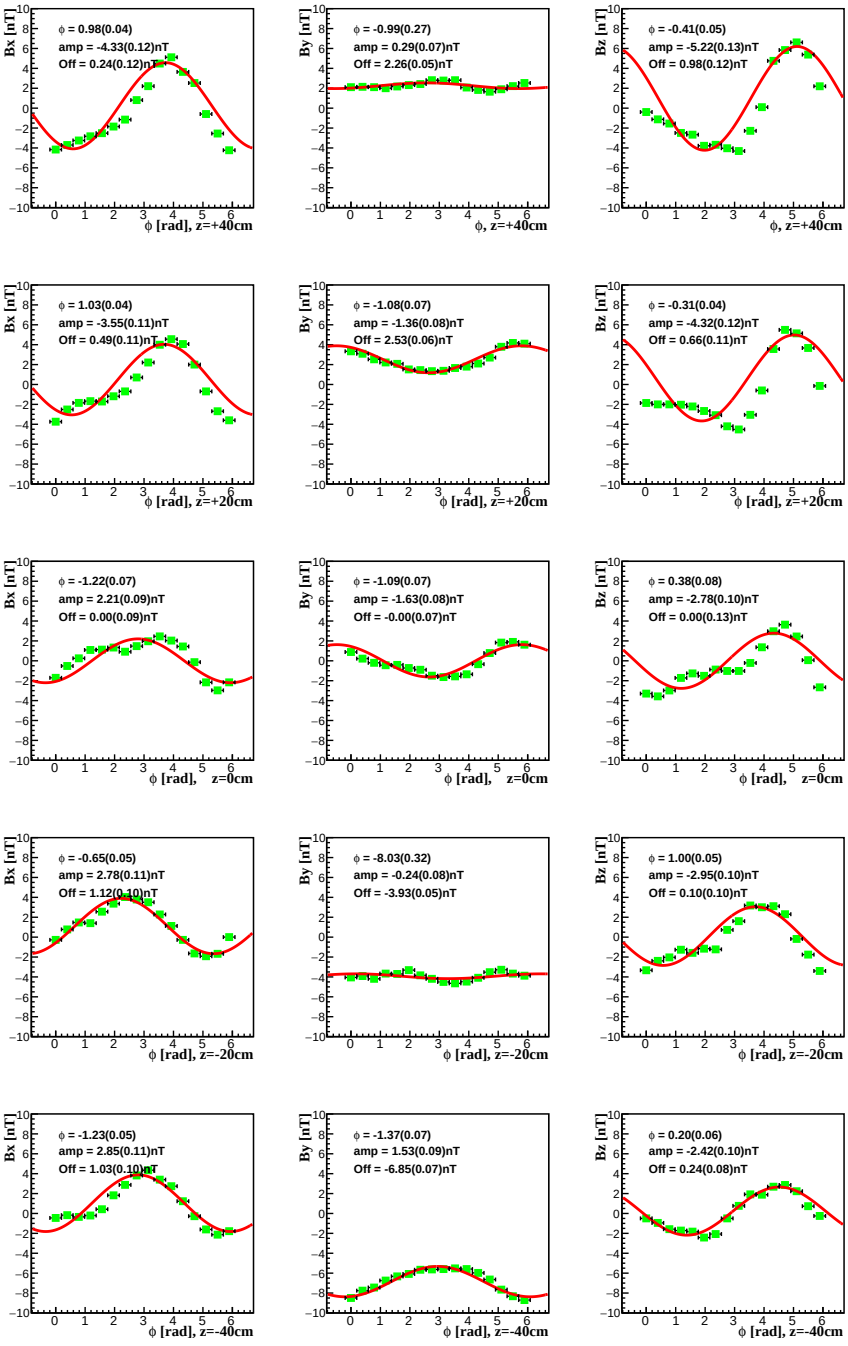

Figure H.8: Map of magnetic field (2021-06-04) inside magnetic shield, with the flux gate in the FG Out state, making a circle around one point at a time. Each point is at a location z with respect to the center of the magnetic shield.

Bibliography

[1] S. Glashow. Partial-symmetries of weak interactions. *Nuclear Physics*, 22:579, 1961.

[2] A. Salam. Weak and electromagnetic interactions. In *Selected Papers Of Abdus Salam: (With Commentary)*, pages 244–254. World Scientific, 1994.

[3] S. Weinberg. A model of leptons. *Phys. rev. letters*, 19:1264, 1967.

[4] G. 't Hooft. Renormalization of massless Yang-Mills fields. *Nuclear physics: B*, 33(1): 173–199, 1971.

[5] G. 't Hooft. Renormalizable lagrangians for massive Yang-Mills fields. *Nuclear physics: B*, 35(1):167–188, 1971.

[6] M. Veltman et al. Regularization and renormalization of gauge fields. *Nuclear Physics B*, 44(1):189–213, 1972.

[7] P.W. Higgs. Broken symmetries and the masses of gauge bosons. *Phys. Rev. Lett.*, 13: 508–509, Oct 1964. doi: 10.1103/PhysRevLett.13.508. URL `https://link.aps.org/doi/10.1103/PhysRevLett.13.508`.

[8] F. Englert and R. Brout. Broken symmetry and the mass of gauge vector mesons. *Phys. Rev. Lett.*, 13:321–323, Aug 1964. doi: 10.1103/PhysRevLett.13.321. URL `https://link.aps.org/doi/10.1103/PhysRevLett.13.321`.

[9] ALEPH Collaboration, DELPHI Collaboration, L3 Collaboration, OPAL Collaboration, and the LEP Electroweak Working Group. Combination procedure for the precise determination of Z boson parameters from results of the LEP experiments. *arxiv*, 2001.

[10] ATLAS Collaboration. Observation of a new particle in the search for the Standard Model Higgs boson with the ATLAS detector at the LHC. *Physics Letters B*, 716(1): 1 – 29, 2012. ISSN 0370-2693. doi: https://doi.org/10.1016/j.physletb.2012.08.020.

[11] CMS Collaboration. Observation of a new boson at a mass of 125 GeV with the CMS experiment at the LHC. *Physics Letters B*, 716(1):30 – 61, 2012. ISSN 0370-2693. doi: https://doi.org/10.1016/j.physletb.2012.08.021.

[12] E.M. Purcell and N.F. Ramsey. On the possibility of electric dipole moments for elementary particles and nuclei. *Phys. Rev.*, 78:807–807, Jun 1950. doi: 10.1103/PhysRev.78.807.

[13] J.H. Smith, E.M. Purcell, and N.F. Ramsey. Experimental limit to the electric dipole moment of the neutron. *Phys. Rev.*, 108:120–122, Oct 1957. doi: 10.1103/PhysRev.108.120.

[14] T.D. Lee and C.N. Yang. Question of parity conservation in weak interactions. *Phys. Rev.*, 104:254–258, Oct 1957. doi: 10.1103/PhysRev.104.254.

[15] C.S. Wu, E. Ambler, R.W. Hayward, D.D. Hoppes, and R.P. Hudson. Experimental test of parity conservation in beta decay. *Phys. Rev.*, 105:1413–1415, Feb 1957. doi: 10.1103/PhysRev.105.1413.

[16] J.H. Christenson, J.W. Cronin, V.L. Fitch, and R. Turlay. Evidence for the 2π Decay of the K_2^0 Meson. *Phys. Rev. Lett.*, 13:138–140, Jul 1964. doi: 10.1103/PhysRevLett.13.138. URL https://link.aps.org/doi/10.1103/PhysRevLett.13.138.

[17] G. Lüders. On the equivalence of invariance under time reversal and under particle-antiparticle conjugation for relativistic field theories. *Det Kgl. Danske Videnskabernes Selskab Mathematisk-fysiske Meddelelser*, 28(5):1–17, 1954.

[18] W. Pauli. *Exclusion principle, Lorentz group and reflection of space-time and charge*. Niels Bohr and the Development of Physics, pp. 30-51. Pergamon Press, 1955.

[19] J.S. Bell. Time reversal in field theory. *Proceedings of the Royal Society of London. Series A, Mathematical and Physical Sciences*, 231(1187):479–495, 1955.

[20] V.A. Kostelecký and N. Russell. Data tables for Lorentz and CPT violation. *Rev. Mod. Phys.*, 83:11–31, Mar 2011. doi: 10.1103/RevModPhys.83.11. URL https://link.aps.org/doi/10.1103/RevModPhys.83.11.

[21] A. Sytema. *Testing Lorentz invariance in β decay*. University of Groningen, 2016.

[22] A.D. Sakharov. Violation of CP invariance, C asymmetry, and baryon asymmetry of the universe. *Soviet Physics Uspekhi*, 34(5):392–393, may 1991. doi: 10.1070/pu1991v034n05abeh002497. URL https://doi.org/10.1070/pu1991v034n05abeh002497.

[23] W. Bernreuther and M. Suzuki. The electric dipole moment of the electron. *Rev. Mod. Phys.*, 63:313–340, Apr 1991. doi: 10.1103/RevModPhys.63.313. URL https://link.aps.org/doi/10.1103/RevModPhys.63.313.

[24] I.B. Khriplovich and S.K. Lamoreaux. *CP Violation Without Strangeness*. Springer Berlin Heidelberg, 1997. ISBN 9783642645778. doi: https://dx.doi.org/10.1007/978-3-642-60838-4.

[25] P.G.H. Sandars. Electric dipole moments of charged particles. *Contemporary Physics*, 42(2):97–111, 2001. doi: 10.1080/00107510010027781. URL http://dx.doi.org/10.1080/00107510010027781.

[26] M. Pospelov and A. Ritz. Electric dipole moments as probes of new physics. *Annals of Physics*, 318(1):119 – 169, 2005. ISSN 0003-4916. doi: https://doi.org/10.1016/j.aop.2005.04.002. URL http://www.sciencedirect.com/science/article/pii/S0003491605000539. Special Issue.

[27] B.L. Roberts and W.J. Marciano. *Lepton dipole moments*, volume 20. World Scientific Publishing Co Pte Ltd, 2009. ISBN 9789814271837.

[28] K. Jungmann. Searching for electric dipole moments. *Annalen der Physik*, 525(8-9):550–564, 2013. ISSN 1521-3889. doi: 10.1002/andp.201300071. URL http://dx.doi.org/10.1002/andp.201300071.

[29] D. DeMille, J.M. Doyle, and A.O. Sushkov. Probing the frontiers of particle physics with tabletop-scale experiments. *Science*, 357(6355):990–994, 2017.

[30] P.G.H. Sandars. The electric dipole moment of an atom. *Physics Letters*, 14(3):194–196, 1965.

[31] P.G.H. Sandars. Measurability of the proton electric dipole moment. *Phys. Rev. Lett.*, 19:1396–1398, 1967. doi: 10.1103/PhysRevLett.19.1396.

[32] P.G.H. Sandars. The electric-dipole moments of an atom I. Some general considerations. *Journal of Physics B: Atomic and Molecular Physics*, 1(3):499–510, 1968. doi: 10.1088/0022-3700/1/3/325.

[33] R.C. Fernow, J.C. Gallardo, W.M. Morse, and Y.K. Semertzidis. MUON EDM EXPERIMENT USING STAGE II OF THE NEUTRINO FACTORY. Technical report, Brookhaven National Lab., Upton, NY (US), 2002.

[34] G.W. Bennett et al. Improved limit on the muon electric dipole moment. *Phys. Rev. D*, 80:052008, Sep 2009. doi: 10.1103/PhysRevD.80.052008. URL https://link.aps.org/doi/10.1103/PhysRevD.80.052008.

[35] V.D. Barger, C. Kao, and A.K. Das. The muon electric dipole moment. In *B physics and CP violation. Proceedings, 2nd International Conference, Honolulu, USA, March 24-27, 1997*, pages 451–456, 1997. doi: 10.1142/9789814503952_0047.

[36] H. Albrecht et al. A search for the electric dipole moment of the τ-lepton. *Physics Letters B*, 485(1–3):37 – 44, 2000. ISSN 0370-2693. doi: https://doi.org/10.1016/S0370-2693(00)00630-4.

[37] K.S. Babu, B. Dutta, and R.N. Mohapatra. Enhanced electric dipole moment of the muon in the presence of large neutrino mixing. *Phys. Rev. Lett.*, 85:5064–5067, Dec 2000. doi: 10.1103/PhysRevLett.85.5064. URL https://link.aps.org/doi/10.1103/PhysRevLett.85.5064.

[38] W.B. Cairncross, D.N. Gresh, M. Grau, K.C. Cossel, T.S. Roussy, Y. Ni, Y. Zhou, J. Ye, and E.A. Cornell. Precision measurement of the electron's electric dipole moment using trapped molecular ions. *Phys. Rev. Lett.*, 119:153001, 2017. doi: 10.1103/PhysRevLett.119.153001.

[39] C.A. Baker, D.D. Doyle, P. Geltenbort, K. Green, M.G.D. van der Grinten, P.G. Harris, P. Iaydjiev, S.N. Ivanov, D.J.R. May, J.M. Pendlebury, J.D. Richardson, D. Shiers, and K.F. Smith. Baker et al. Reply:. *Phys. Rev. Lett.*, 98:149102, Apr 2007. doi: 10.1103/PhysRevLett.98.149102. URL https://link.aps.org/doi/10.1103/PhysRevLett.98.149102.

[40] G.E. Harrison, P.G.H. Sandars, and S.J. Wright. Experimental Limit on the Proton Electric Dipole Moment. *Phys. Rev. Lett.*, 22:1263–1265, Jun 1969. doi: 10.1103/PhysRevLett.22.1263. URL https://link.aps.org/doi/10.1103/PhysRevLett.22.1263.

[41] G.E. Harrison, P.G.H. Sandars, and S.J. Wright. Experimental Limit on the Proton Electric Dipole Moment, ERRATA. *Phys. Rev. Lett.*, 23:274–274, Aug 1969. doi: 10.1103/PhysRevLett.23.274.3. URL https://link.aps.org/doi/10.1103/PhysRevLett.23.274.3.

[42] E.A. Hinds and P.G.H. Sandars. Experiment to search for P- and T-violating interactions in the hyperfine structure of thallium fluoride. *Phys. Rev. A*, 21:480–487, Feb 1980. doi: 10.1103/PhysRevA.21.480. URL https://link.aps.org/doi/10.1103/PhysRevA.21.480.

[43] D.A. Wilkening, N.F. Ramsey, and D.J. Larson. Search for P and T violations in the hyperfine structure of thallium fluoride. *Phys. Rev. A*, 29:425–438, Feb 1984. doi: 10.1103/PhysRevA.29.425. URL https://link.aps.org/doi/10.1103/PhysRevA.29.425.

[44] D. Anastassopoulos, EDM Collaboration, et al. Ags proposal: Search for a permanent electric dipole moment of the deuteron nucleus at the 10-29 e·cm level. *BNL Report*, 2008.

[45] M. Ledbetter. *Progress Toward a Search for a Permanent Electric Dipole Moment in Liquid 129Xe*. Princeton University, 2005.

[46] F. Kuchler, P. Fierlinger, and D. Wurm. A novel approach to measure the electric dipole moment of the isotope 129-Xe. *EPJ Web of Conferences*, 66:05011, 2014. doi: 10.1051/epjconf/20146605011. URL https://doi.org/10.1051/epjconf/20146605011.

[47] W.C. Griffith, M.D. Swallows, T.H. Loftus, M.V. Romalis, B.R. Heckel, and E.N. Fortson. Improved limit on the permanent electric dipole moment of ^{199}Hg. *Phys. Rev. Lett.*, 102:101601, Mar 2009. doi: 10.1103/PhysRevLett.102.101601. URL https://link.aps.org/doi/10.1103/PhysRevLett.102.101601.

[48] M.A. Rosenberry and T.E. Chupp. Atomic electric dipole moment measurement using spin exchange pumped masers of ^{129}Xe and ^{3}He. *Phys. Rev. Lett.*, 86:22–25, Jan 2001. doi: 10.1103/PhysRevLett.86.22. URL https://link.aps.org/doi/10.1103/PhysRevLett.86.22.

[49] M.A. Rosenberry. *A precision measurement of the ^{129}Xe electric dipole moment using dual noble gas masers*. University of Michigan, 2000.

[50] W. Heil. Polarized ^{3}He and ^{129}Xe and EDMs. *International Symposium on LEPTON MOMENTS. Cape Cod*, 2014.

[51] F. Allmendinger, P. Blümler, M. Doll, O. Grasdijk, W. Heil, K. Jungmann, S. Karpuk, H.-J. Krause, A. Offenhäusser, M. Repetto, U. Schmidt, Y. Sobolev, K. Tullney, L. Willmann, and S. Zimmer. Precise measurement of magnetic field gradients from free spin precession signals of ^{3}He and ^{129}Xe magnetometers. *The European Physical Journal D*, 71(4):98, Apr 2017. ISSN 1434-6079. doi: 10.1140/epjd/e2017-70505-4. URL https://doi.org/10.1140/epjd/e2017-70505-4.

[52] B.J. Heidenreich, O.T. Elliott, N.D. Charney, K.A. Virgien, A.W. Bridges, M.A. McKeon, S.K. Peck, D. Krause, J.E. Gordon, L.R. Hunter, and S.K. Lamoreaux. Limit on the electron electric dipole moment in gadolinium-iron garnet. *Phys. Rev. Lett.*, 95:253004, Dec 2005. doi: 10.1103/PhysRevLett.95.253004. URL https://link.aps.org/doi/10.1103/PhysRevLett.95.253004.

[53] Y.J. Kim, C.-Y. Liu, S.K. Lamoreaux, and G. Reddy. Experimental search for the electron Electric Dipole Moment using solid state techniques. *Journal of Physics: Conference Series*, 312(10):102009, 2011. URL http://stacks.iop.org/1742-6596/312/i=10/a=102009.

[54] B.C. Regan, E.D. Commins, C.J. Schmidt, and D. DeMille. New Limit on the Electron Electric Dipole Moment. *Phys. Rev. Lett.*, 88:071805, Feb 2002. doi: 10.1103/PhysRevLett.88.071805. URL https://link.aps.org/doi/10.1103/PhysRevLett.88.071805.

[55] J.J. Hudson, D.M. Kara, I.J. Smallman, B.E. Sauer, M.R. Tarbutt, and E.A. Hinds. Improved measurement of the shape of the electron. *Nature*, 473(7348):493–496, 2011.

[56] The ACME Collaboration, J. Baron, W.C. Campbell, D. DeMille, J.M. Doyle, G. Gabrielse, Y.V. Gurevich, P.W. Hess, N.R. Hutzler, E. Kirilov, I. Kozyryev, B.R. O'Leary, C.D. Panda, M.F. Parsons, E.S. Petrik, B. Spaun, A.C. Vutha, and A. D. West. Order of Magnitude Smaller Limit on the Electric Dipole Moment of the Electron. *Science*, 343(6168):269–272, 2014. ISSN 0036-8075. doi: 10.1126/science.1248213. URL http://science.sciencemag.org/content/343/6168/269.

[57] P.A.B. Haase, D.J. Doeglas, A. Boeschoten, E. Eliav, M. Iliaš, P. Aggarwal, H.L. Bethlem, A. Borschevsky, K. Esajas, Y. Hao, et al. Systematic study and uncertainty evaluation of P, T-odd molecular enhancement factors in BaF. *The Journal of chemical physics*, 155 (3):034309, 2021.

[58] K. Gaul, S. Marquardt, T. Isaev, and R. Berger. Systematic study of relativistic and chemical enhancements of $\mathcal{P},\mathcal{T}$-odd effects in polar diatomic radicals. *Phys. Rev. A*, 99:032509, Mar 2019. doi: 10.1103/PhysRevA.99.032509. URL https://link.aps.org/doi/10.1103/PhysRevA.99.032509.

[59] T. Fleig. $\mathcal{P},\mathcal{T}$-odd and magnetic hyperfine-interaction constants and excited-state lifetime for HfF^+. *Phys. Rev. A*, 96:040502, Oct 2017. doi: 10.1103/PhysRevA.96.040502. URL https://link.aps.org/doi/10.1103/PhysRevA.96.040502.

[60] L.V. Skripnikov and A.V. Titov. Theoretical study of thorium monoxide for the electron electric dipole moment search: Electronic properties of H3Δ1 in ThO. *The Journal of Chemical Physics*, 142(2), 01 2015. ISSN 0021-9606. doi: 10.1063/1.4904877. URL https://doi.org/10.1063/1.4904877. 024301.

[61] S. Sasmal, H. Pathak, M. K. Nayak, N. Vaval, and S. Pal. Calculation of P,T-odd interaction constant of PbF using Z-vector method in the relativistic coupled-cluster framework. *The Journal of Chemical Physics*, 143(8), 08 2015. ISSN 0021-9606. doi: 10.1063/1.4929591. URL https://doi.org/10.1063/1.4929591. 084119.

[62] A. Sunaga, M. Abe, M. Hada, and B.P. Das. Relativistic coupled-cluster calculation of the electron-nucleus scalar-pseudoscalar interaction constant W_s in YbF. *Phys. Rev. A*, 93:042507, Apr 2016. doi: 10.1103/PhysRevA.93.042507. URL https://link.aps.org/doi/10.1103/PhysRevA.93.042507.

[63] M. Pospelov and A. Ritz. Electric dipole moments as probes of new physics. *Annals of physics*, 318(1):119–169, 2005.

[64] Y. Ema, T. Gao, and M. Pospelov. Standard Model Prediction for Paramagnetic Electric Dipole Moments. *Physicial Review Letters*, 2022. doi: 10.1103/PhysRevLett.129.231801.

[65] J. Beacham et al. Physics beyond colliders at CERN: beyond the standard model working group report. *J. of Phys. G: Nucl. and Part. Phys.*, 47(1):010501, 2019. doi: 10.1088/1361-6471/ab4cd2.

[66] COMSOL MultiPhysics, 2022. URL https://www.comsol.com/.

[67] I.B. Khriplovich. The quark electric dipole moment and the induced θ-term in the Kobayashi-Maskawa model. *Physics Letters B*, 173(2):193–196, 1986. ISSN 0370-2693. doi: https://doi.org/10.1016/0370-2693(86)90245-5. URL https://www.sciencedirect.com/science/article/pii/0370269386902455.

[68] A. Czarnecki and B. Krause. Neutron Electric Dipole Moment in the Standard Model: Complete Three-Loop Calculation of the Valence Quark Contributions. *Phys. Rev. Lett.*, 78:4339–4342, Jun 1997. doi: 10.1103/PhysRevLett.78.4339. URL https://link.aps.org/doi/10.1103/PhysRevLett.78.4339.

[69] E.P. Shabalin. Electric Dipole Moment of Quark in a Gauge Theory with Left-Handed Currents. *Sov. J. Nucl. Phys.*, 28:75, 1978.

[70] C. Jarlskog. Commutator of the Quark Mass Matrices in the Standard Electroweak Model and a Measure of Maximal CP Nonconservation. *Phys. Rev. Lett.*, 55:1039–1042, Sep 1985. doi: 10.1103/PhysRevLett.55.1039. URL https://link.aps.org/doi/10.1103/PhysRevLett.55.1039.

[71] M.E. Pospelov and I.B. Khriplovich. Electric dipole moment of the W boson and the electron in the Kobayashi-Maskawa model. *Sov. J. Nucl. Phys.*, 53:638–640, 1991.

[72] M.J. Booth. The Electric Dipole Moment of the W and Electron in the Standard Model, 1993.

[73] M. Pospelov and A. Ritz. CKM benchmarks for electron electric dipole moment experiments. *Phys. Rev. D*, 89:056006, Mar 2014. doi: 10.1103/PhysRevD.89.056006. URL https://link.aps.org/doi/10.1103/PhysRevD.89.056006.

[74] J. Bsaisou, J. de Vries, C. Hanhart, S. Liebig, Ulf-G. Meißner, D. Minossi, A. Nogga, and A. Wirzba. Nuclear electric dipole moments in chiral effective field theory. *J. High Energ. Phys*, 03, 2015. doi: 10.1007/JHEP03(2015)104. URL https://doi.org/10.1007/JHEP03(2015)104.

[75] J. de Vries, E. Mereghetti, and A. Walker-Loud. Baryon mass splittings and strong CP violation in SU(3) chiral perturbation theory. *Phys. Rev. C*, 92:045201, Oct 2015. doi: 10.1103/PhysRevC.92.045201. URL https://link.aps.org/doi/10.1103/PhysRevC.92.045201.

[76] B. Graner, Y. Chen, E.G. Lindahl, and B.R. Heckel. Reduced Limit on the Permanent Electric Dipole Moment of ^{199}Hg. *Phys. Rev. Lett.*, 116:161601, Apr 2016. doi: 10.1103/PhysRevLett.116.161601. URL https://link.aps.org/doi/10.1103/PhysRevLett.116.161601.

[77] T.E. Chupp, P. Fierlinger, M.J. Ramsey-Musolf, and J.T. Singh. Electric dipole moments of atoms, molecules, nuclei, and particles. *Rev. Mod. Phys.*, 91:015001, Jan 2019. doi: 10.1103/RevModPhys.91.015001. URL https://link.aps.org/doi/10.1103/RevModPhys.91.015001.

[78] C.-Y. Seng. Reexamination of the standard model nucleon electric dipole moment. *Phys. Rev. C*, 91:025502, Feb 2015. doi: 10.1103/PhysRevC.91.025502. URL https://link.aps.org/doi/10.1103/PhysRevC.91.025502.

[79] V. Andreev, D.G. Ang, and ACME Collaboration 2018. Improved limit on the electric dipole moment of the electron. *Nature*, 562:355, 2018. doi: 10.1038/s41586-018-0599-8.

[80] T.S. Roussy, L. Caldwell, T. Wright, W.B. Cairncross, Y. Shagam, K.B. Ng, N. Schlossberger, S.Y. Park, A. Wang, J. Ye, and E.A. Cornell. An improved bound on the electron's electric dipole moment. *Science*, 381(6653):46–50, 2023. doi: 10.1126/science.adg4084. URL https://www.science.org/doi/abs/10.1126/science.adg4084.

[81] L. Caldwell, T.S. Roussy, T. Wright, W.B. Cairncross, Y. Shagam, K.B. Ng, N. Schlossberger, S.Y. Park, A. Wang, J. Ye, and E.A. Cornell. Systematic and statistical uncertainty evaluation of the HfF^+ electron electric dipole moment experiment. *Phys. Rev. A*, 108:012804, Jul 2023. doi: 10.1103/PhysRevA.108.012804. URL https://link.aps.org/doi/10.1103/PhysRevA.108.012804.

[82] NL eEDM collaboration, P. Aggarwal, H.L. Bethlem, A. Borschevsky, M. Denis, K. Esajas, P.A.B. Haase, Y. Hao, S. Hoekstra, K. Jungmann, T.B. Meijknecht, M.C. Mooij, R.G.E. Timmermans, W. Ubachs, L. Willmann, and A. Zapara. Measuring the electric dipole moment of the electron in BaF. *Eur. Phys. J. D*, 72(11):197, 2018. doi: 10.1140/epjd/e2018-90192-9.

[83] Planck Collaboration. Planck 2018 results. I. Overview and the cosmological legacy of Planck. *A&A*, 641:A1, 2020.

[84] LHCb collaboration. Test of lepton universality in beauty-quark decays. *arXiv:2103.11769 [hep-ex]*, 2021.

[85] D. Colladay and V.A. Kostelecký. CPT violation and the standard model. *Phys. Rev. D*, 55:6760–6774, Jun 1997. doi: 10.1103/PhysRevD.55.6760. URL https://link.aps.org/doi/10.1103/PhysRevD.55.6760.

[86] S. Coleman and S.L. Glashow. High-energy tests of lorentz invariance. *Phys. Rev. D*, 59:116008, Apr 1999. doi: 10.1103/PhysRevD.59.116008. URL https://link.aps.org/doi/10.1103/PhysRevD.59.116008.

[87] P.G.H. Sandars and E. Lipworth. Electric Dipole Moment of the Cesium Atom. A New Upper Limit to the Electric Dipole Moment of the Free Electron. *Phys. Rev. Lett.*, 13:718–720, Dec 1964. doi: 10.1103/PhysRevLett.13.718.

[88] T.S. Stein, J.P. Carrico, E. Lipworth, and M.C. Weisskopf. Electric Dipole Moment of the Cesium Atom. A New Upper Limit to the Electric Dipole Moment of the Free Electron. *Phys. Rev. Lett.*, 19:741–743, Sep 1967. doi: 10.1103/PhysRevLett.19.741.

[89] M.C. Weisskopf, J.P. Carrico, H. Gould, E. Lipworth, and T.S. Stein. Electric Dipole Moment of the Cesium Atom. A New Upper Limit to the Electric Dipole Moment of the Electron. *Phys. Rev. Lett.*, 21:1645–1648, Dec 1968. doi: 10.1103/PhysRevLett.21.1645.

[90] J. Brown and A. Carrington. *Rotational Spectroscopy of Diatomic Molecules*. Cambridge University Press, 2007. ISBN 9780521810098.

[91] A. Boeschoten. *Precision measurements in diatomic molecules: a route to a permanent electric dipole moment*. University of Groningen, 2023.

[92] A. Boeschoten, V.R. Marshall, T.B. Meijknecht, A. Touwen, H.L. Bethlem, A. Borschevsky, S. Hoekstra, J.W.F. van Hofslot, K. Jungmann, M.C. Mooij, R.G.E. Timmermans, W. Ubachs, and L. Willmann. Novel spin-precession method for sensitive EDM searches, 2023. URL https://arxiv.org/abs/2303.06402.

[93] P. Aggarwal, V.R. Marshall, H.L. Bethlem, A. Boeschoten, A. Borschevsky, M. Denis, K. Esajas, Y. Hao, S. Hoekstra, K. Jungmann, et al. Lifetime measurements of the A 2 Π 1/2 and A 2 Π 3/2 states in BaF. *Physical Review A*, 100(5):052503, 2019.

[94] P. Aggarwal, H.L. Bethlem, A. Boeschoten, A. Borschevsky, K. Esajas, Y. Hao, S. Hoekstra, K. Jungmann, V.R. Marshall, T.B. Meijknecht, et al. A supersonic laser ablation beam source with narrow velocity spreads. *Review of Scientific Instruments*, 92(3): 033202, 2021.

[95] Y. Hao, L.F. Pašteka, L. Visscher, P. Aggarwal, H.L. Bethlem, A. Boeschoten, A. Borschevsky, M. Denis, K. Esajas, S. Hoekstra, et al. High accuracy theoretical investigations of CaF, SrF, and BaF and implications for laser-cooling. *The Journal of chemical physics*, 151(3):034302, 2019.

[96] V.R. Marshall. *PhD Thesis*. University of Groningen, 2024.

[97] R. Loudon. *The quantum theory of light*. Oxford University Press, third edition, 2000.

[98] N.J. Ayres, G. Ban, L. Bienstman, G. Bison, K. Bodek, V. Bondar, T. Bouillaud, E. Chanel, J. Chen, P.-J. Chiu, B. Clément, C.B. Crawford, M. Daum, B. Dechenaux, C.B. Doorenbos, S. Emmenegger, L. Ferraris-Bouchez, M. Fertl, A. Fratangelo, P. Flaux, D. Goupillière, W.C. Griffith, Z.D. Grujic, P.G. Harris, K. Kirch, P.A. Koss, J. Krempel, B. Lauss, T. Lefort, Y. Lemière, A. Leredde, M. Meier, J. Menu, D.A. Mullins, O. Naviliat-Cuncic, D. Pais, F.M. Piegsa, G. Pignol, G. Quéméner, M. Rawlik, D. Rebreyend, I. Rienäcker, D. Ries, S. Roccia, K.U. Ross, D. Rozpedzik, W. Saenz, P. Schmidt-Wellenburg, A. Schnabel, N. Severijns, B. Shen, T. Stapf, K. Svirina, R. Tavakoli Dinani, S. Touati, J. Thorne, R. Virot, J. Voigt, E. Wursten, N. Yazdandoost, J. Zejma, and G. Zsigmond. The design of the n2EDM experiment. *The European Physical Journal C*, 81(6), 2021. doi: 10.1140/epjc/s10052-021-09298-z. URL https://doi.org/10.1140/epjc/s10052-021-09298-z.

[99] P. Aggarwal. *Production, deceleration and trapping of SrF molecules*. University of Groningen, 2021. doi: 10.33612/diss.177484581.

[100] S. Denis, L. Dusoulier, M. Dirickx, Ph. Vanderbemden, R. Cloots, M. Ausloos, and B. Vanderheyden. Magnetic shielding properties of high-temperature superconducting tubes subjected to axial fields. *Superconductor Science and Technology*, 20(3):192, jan 2007. doi: 10.1088/0953-2048/20/3/014. URL https://dx.doi.org/10.1088/0953-2048/20/3/014.

[101] J.-F. Fagnard, S. Denis, G. Lousberg, M. Dirickx, M. Ausloos, B. Vanderheyden, and P. Vanderbemden. DC and AC Shielding Properties of Bulk High-Tc Superconducting Tubes. *IEEE Transactions on Applied Superconductivity*, 19(3):2905–2908, 2009. doi: 10.1109/TASC.2009.2017880.

[102] J.K. Joosten. Magnetic field compensation inside the interaction zone of the BaF eEDM experiment, July 2019.

[103] J.O. Grasdijk. *Search for the permanent electric dipole moment of ^{129}Xe*. University of Groningen, 2018.

[104] C.P. Bidinosti and J.W. Martin. Passive magnetic shielding in static gradient fields. *AIP Advances*, 4(4):047135, 2014. doi: 10.1063/1.4873714.

[105] Sekels GmbH, 2022. URL `https://www.sekels.de/en/home/`.

[106] Meca Magnetic, 2022. URL `https://www.mecamagnetic.com/magnetic-shielding/`.

[107] S. Chikazumi. *Physics of ferromagnetism*. Oxford University Press, second edition, 1997.

[108] F. Thiel, A. Schnabel, S. Knappe-Grüneberg, D. Stollfuß, and M. Burghoff. Demagnetization of magnetically shielded rooms. *Review of Scientific Instruments*, 78(3):035106, 2007. doi: 10.1063/1.2713433.

[109] D.J. Griffiths. *Introduction to Electrodynamics*. Pearson, 2013. ISBN 9780321856562.

[110] C. Juchem, D. Green, and R.A. de Graaf. Multi-coil magnetic field modeling. *Journal of Magnetic Resonance*, 236:95–104, 2013. doi: https://doi.org/10.1016/j.jmr.2013.08.015.

[111] *The Vacuum Technology Book Volume II*, 2013. URL `https://www.pfeiffer-vacuum.com/en/know-how/`.

[112] A.P. Touwen. *PhD Thesis*. University of Groningen, 2024.

[113] F. Schwarz. Caddie software, 2000s.

[114] E.A. Dijck. *Spectroscopy of Trapped $^{138}Ba^{+}$ Ions for Atomic Parity Violation and Optical Clocks*. University of Groningen, 2020. ISBN 978-94-034-2298-5. doi: 10.33612/diss.108023683.

[115] *Magnetic Field Sensor FLC3-70*. Stefan Mayer Instruments, 2022. URL `https://stefan-mayer.com/en/downloads.html`.

[116] April 2020 was zonnigste ooit, 2020. URL `https://www.weeronline.nl/nieuws/weeroverzichten-2020-april`.

[117] W.J. Riley. *NIST Special Publication 1065 Handbook of Frequency Stability Analysis*. NIST, 2008.

[118] NIST 2018 CODATA recommended values, 2018. URL `https://physics.nist.gov/cuu/Constants/bibliography.html`.

[119] C. Cohen-Tannoudji and D. Guery-Odelin. *Advances in Atomic Physics: An overview*. World Scientific Publishing Company, 2011.

[120] G. Petit and B. Luzum. *The 2010 Reference Edition of the IERS Conventions*. Springer, 2013.

[121] P. Aggarwal, Y. Yin, K. Esajas, H.L. Bethlem, A. Boeschoten, A. Borschevsky, S. Hoekstra, K. Jungmann, V.R. Marshall, T.B. Meijknecht, M.C. Mooij, R.G.E. Timmermans, A. Touwen, W. Ubachs, and L. Willmann. Deceleration and trapping of srf molecules. *Phys. Rev. Lett.*, 127:173201, Oct 2021. doi: 10.1103/PhysRevLett.127.173201. URL `https://link.aps.org/doi/10.1103/PhysRevLett.127.173201`.

[122] K. Esajas. *Intense slow beams of heavy molecules to test fundamental symmetries*. University of Groningen, 2021. doi: 10.33612/diss.170215126.